Development of transverse flow at small and large opacities in conformal kinetic theory

Victor E. Ambruş,[1,2] S. Schlichting,[3] and C. Werthmann[3,*]

[1]*Institut für Theoretische Physik, Johann Wolfgang Goethe-Universität, Max-von-Laue-Strasse 1, D-60438 Frankfurt am Main, Germany*
[2]*Department of Physics, West University of Timişoara, Bd. Vasile Pârvan 4, Timişoara 300223, Romania*
[3]*Fakultät für Physik, Universität Bielefeld, D-33615 Bielefeld, Germany*

(Received 29 September 2021; accepted 8 December 2021; published 28 January 2022)

We employ an effective kinetic description, based on the Boltzmann equation in the relaxation time approximation, to study the space-time dynamics and development of transverse flow of small and large collision systems. By combining analytical insights in the small opacity limit with numerical simulations at larger opacities, we are able to describe the development of transverse flow from very small to very large opacities. Surprisingly, we find that deviations between kinetic theory and hydrodynamics persist even in the limit of very large opacities, which can be attributed to the presence of the early preequilibrium phase.

DOI: 10.1103/PhysRevD.105.014031

I. INTRODUCTION

Over the past decades, the collective flow of soft hadrons produced in high-energy heavy-ion collisions at the Relativistic Heavy-Ion Collider (RHIC) and the Large Hadron Collider (LHC) has become one of the cornerstones to establish the existence of deconfined quark gluon plasma (QGP) and to characterize the properties of strong-interaction matter under extreme conditions. The space-time dynamics of relativistic heavy-ion collisions is commonly described in terms of relativistic viscous hydrodynamics [1–5], which provides an accurate description of experimental measurements of soft hadron production and collective flow at RHIC and LHC.

Based on the tremendous success in quantifying properties of the QGP produced in heavy-ion collisions [6–9], different groups have performed hydrodynamic calculations for small systems [10–24], which also provide a reasonable description of the experimentally observed collective flow in proton-nucleus and proton-proton collisions [25–27]. However, in contrast to nucleus-nucleus collisions, such calculations are subject to much larger uncertainties, where, in addition to the poorly constrained initial state geometry [19,28,29], one may question the theoretical justification for employing a hydrodynamic description for a system, which features a very short lifetime and consists of very few degrees of freedom.

Despite significant progress in understanding the onset of hydrodynamic behavior in QCD plasmas (see, e.g., [30,31] for recent reviews), calculations performed in this regard are typically subject to simplifying assumptions, e.g., modeling the early stages of heavy-ion collisions in terms of a transversely homogenous Bjorken flow, and are therefore not (yet) able to capture the competing effects of longitudinal and transverse expansion in small collision systems.

Beyond studies based on effective macroscopic descriptions of QCD, there have also been attempts to explain the onset of collective behavior in small systems by invoking a microscopic origin of the correlations. Examples include calculations within the color glass condensate (CGC) effective field theory of high-energy QCD [32–42], as well as more conventional approaches extending general purpose event generators such as PYTHIA or HERWIG to include space-time dependent final state interactions [43–46].

Clearly, the development of a unified description that encompasses both paradigms in the respective limit is an outstanding challenge [47]. Beyond microscopic calculations that are rooted in the underlying theory of QCD, it is therefore an important achievement that—at least within simpler microscopic descriptions—it is possible to include a nontrivial transverse expansion [48–55], and, in some cases, even detailed event-by-event geometries [37,56–58] to describe the onset of collective flow. In this spirit, the

*cwerthmann@physik.uni-bielefeld.de

central objective of this paper is to scrutinize the development of transverse flow and investigate possible changes in the space-time dynamics and flow response of small and large systems.

We follow previous works [52,53,57] and employ a simple kinetic description of the system described in Sec. II, where the system size and energy dependence is characterized by a single opacity parameter. Within this framework, we perform (semi)analytic calculations to leading order in opacity in Sec. III and subsequently in Sec. IV develop two different numerical schemes that allow us to study the evolution of the system all the way from very low to very high opacity. Numerical results are presented in Sec. V, where we analyze the longitudinal cooling and flow response in kinetic theory as a function of opacity and compare it to analogous calculations in ideal and viscous hydrodynamics. We conclude with Sec. VI. Several appendices contain additional details and explicit expressions for the (semi)analytic calculations.

II. EFFECTIVE KINETIC DESCRIPTION OF ANISOTROPIC FLOW

A. Setup

We will describe the system via an averaged phase-space distribution $f(x,p)$ of (massless) quasiparticles, for which we assume boost invariance along the longitudinal (beam) direction. Effectively, this reduces the dimensionality of the problem to $(2+1)+3$ dimensions, which can be efficiently described using Milne coordinates $x^\mu=(\tau,\mathbf{x}_\perp,\eta)$ and $p^\mu=(p^\tau,\mathbf{p}_\perp,p^\eta)$, where

$$\tau=\sqrt{(x^0)^2-(x^3)^2},\qquad \eta=\operatorname{artanh}(x^3/x^0), \tag{1}$$

such that τ is invariant, and η behaves additively under boosts in the longitudinal direction. Defining similarly

$$y=\operatorname{artanh}(p^z/p^t), \tag{2}$$

it follows from boost invariance that the phase-space distribution f can only depend on η and y via their difference. We denote transverse positions in terms of regular cartesian coordinates $\mathbf{x}_\perp=(x^1,x^2)$, such that the metric of the coordinate system $(\tau,\mathbf{x}_\perp,\eta)$ is given by $g_{\mu\nu}=\operatorname{diag}(1,-1,-1,-\tau^2)$. The corresponding momenta $(p^\tau,\mathbf{p}_\perp,p^\eta)$ are the cartesian transverse momentum $\mathbf{p}_\perp$, and

$$p^\tau=p_\perp\cosh(y-\eta),\qquad p^\eta=\frac{p_\perp}{\tau}\sinh(y-\eta), \tag{3}$$

where $p_\perp=|\mathbf{p}_\perp|$. Based on a kinetic description of the nonequilibrium dynamics, the evolution of the phase-space distribution is governed by the Boltzmann equation,[1]

$$p^\mu\partial_\mu f=C[f]. \tag{4}$$

For the collision kernel, we employ the relaxation time approximation (RTA),

$$C_{\mathrm{RTA}}[f]=-\frac{p_\mu u^\mu}{\tau_R}\left[f-f_{\mathrm{eq}}\left(\frac{p_\mu u^\mu}{T}\right)\right], \tag{5}$$

where we choose a temperature-dependent relaxation time,

$$\tau_R=\frac{5\eta/s}{T}, \tag{6}$$

to describe a conformal system with constant shear viscosity to entropy density ratio η/s. Energy-momentum conservation requires that the local equilibrium temperature T and rest-frame velocity u^μ are determined via the Landau matching condition [60–64],

$$u_\nu T^{\mu\nu}=\epsilon u^\mu, \tag{7}$$

with timelike four-velocity eigenvector $u_\mu u^\mu=+1$ and eigenvalue ϵ, representing the energy in the local rest frame. The temperature T can be computed from the energy density ϵ via the equation of state,

$$\epsilon=\frac{\pi^2}{30}\nu_{\mathrm{eff}}T^4, \tag{8}$$

which introduces a proportionality factor $\frac{\pi^2}{30}\nu_{\mathrm{eff}}$, which can be absorbed into redefinitions of the related quantities (cf. Sec. II B). The stress-energy tensor $T^{\mu\nu}$ is obtained from the distribution function f via

$$T^{\mu\nu}(x)=\nu_{\mathrm{eff}}\sqrt{-g}\int\frac{\mathrm{d}^3p}{(2\pi)^3p^\tau}p^\mu p^\nu f(x,p), \tag{9}$$

where $\sqrt{-g}=\tau$ denotes the metric determinant, $\mathrm{d}^3p=\mathrm{d}^2\mathbf{p}_\perp\mathrm{d}p^\eta$ is the integration measure in Milne coordinates, and ν_{eff} represents the degeneracy factor.

Since the computation of observables will involve weighted integration of f over momentum space, we define a shorthand notation $\langle\cdot\rangle$ as

[1]We note that in Eq. (4), coordinate derivatives on the lhs are to be evaluated at constant p^μ in Minkowksi space. Throughout this manuscript, we will employ different parametrizations of the spatial and momentum coordinates, which give rise to additional terms on the lhs. Specifically for a boost-invariant system in Milne coordinates, one finds [59]

$$p^\tau\partial_\tau f+\boldsymbol{p}_\perp\cdot\partial_{\boldsymbol{x}_\perp}f-\frac{p^\tau p^\eta}{\tau}\frac{\partial f}{\partial p^\eta}=C[f].$$

$$\langle \mathcal{O} \rangle = \nu_{\text{eff}} \sqrt{-g} \int \frac{\mathrm{d}^3 p}{(2\pi)^3 p^\tau} \mathcal{O}(\mathbf{p}_\perp, p^\eta) f, \tag{10}$$

which allows, for example, one to write the energy-momentum tensor as $T^{\mu\nu} = \langle p^\mu p^\nu \rangle$.

We consider initial conditions motivated by the CGC effective field theory of high-energy QCD [65], where the initial state very shortly after the collision ($\tau \sim 1/Q_s$) can be viewed as a highly anisotropic collection of gluons with typical transverse momenta $\sim Q_s$ and vanishing longitudinal momenta in the local rest frame [37,41]. Specifically, we will consider initial conditions of the form,

$$f(\tau_0, \mathbf{x}_\perp, \mathbf{p}_\perp, y - \eta) = \frac{(2\pi)^3}{\nu_{\text{eff}}} \frac{\delta(y-\eta)}{\tau_0 p_\perp} \frac{\mathrm{d}N_0}{\mathrm{d}^2\mathbf{x}_\perp \mathrm{d}^2\mathbf{p}_\perp \mathrm{d}y}, \tag{11}$$

which has vanishing longitudinal pressure ($T^\eta{}_\eta = 0$). Strikingly, it can be shown (cf. Sec. II B) that—due to the particularly simple nature of RTA—certain energy-weighted observables do not depend on a particular form of the (isotropic) momentum distribution $\frac{\mathrm{d}N_0}{\mathrm{d}^2\mathbf{x}_\perp \mathrm{d}^2\mathbf{p}_\perp \mathrm{d}y}$ [52], and we will therefore not specify it further. Instead, the dynamics is entirely described by the initial energy density distribution, which, for the initial conditions in Eq. (11), is determined by[2]

$$\epsilon(\tau_0, \mathbf{x}_\perp) = \frac{1}{\tau_0} \int d^2\mathbf{p}_\perp p_\perp \frac{\mathrm{d}N_0}{\mathrm{d}^2\mathbf{x}_\perp \mathrm{d}^2\mathbf{p}_\perp \mathrm{d}y}. \tag{12}$$

We take the initial energy density $\epsilon(\tau_0, \mathbf{x}_\perp)$ as a superposition of an isotropic background $\bar{\epsilon}(\tau_0, x_\perp)$ depending only on $x_\perp = |\mathbf{x}_\perp|$ and an anisotropic component $\delta\epsilon(\tau_0, \mathbf{x}_\perp)$; i.e.,

$$\epsilon(\tau_0, \mathbf{x}_\perp) = \bar{\epsilon}(\tau_0, x_\perp) + \delta\epsilon(\tau_0, \mathbf{x}_\perp). \tag{13}$$

We follow previous works [51,57] and consider the background to be of a rotationally symmetric Gaussian shape,

$$\bar{\epsilon}(\tau_0, x_\perp) = \frac{1}{\pi R^2 \tau_0} \frac{\mathrm{d}E_\perp^{(0)}}{\mathrm{d}\eta} \exp\left(-\frac{x_\perp^2}{R^2}\right), \tag{14}$$

where R denotes the transverse system size and $\frac{\mathrm{d}E_\perp^{(0)}}{\mathrm{d}\eta}$ denotes the initial energy per unit rapidity. Similarly, the anisotropic perturbations are taken as[3]

$$\delta\epsilon(\tau_0, \mathbf{x}_\perp) = \bar{\epsilon}(\tau_0, x_\perp)\delta_n \exp\left(-\alpha \frac{x_\perp^2}{R^2}\right)\left(\frac{x_\perp}{R}\right)^n \times \cos(n\phi^{(n)}_{\mathbf{x}_\perp \mathbf{n}_\perp}), \tag{15}$$

such that upon integrating over the transverse coordinates $\mathbf{x}_\perp$, the perturbations do not contribute to the total energy. By $\phi^{(n)}_{\mathbf{x}_\perp \mathbf{n}_\perp}$, we denote the angle,

$$\phi^{(n)}_{\mathbf{x}_\perp \mathbf{n}_\perp} = \phi_x - \Psi_n, \tag{16}$$

where ϕ_x is the position space azimuthal angle, i.e., $\phi_x = \arctan(x^2/x^1)$, and Ψ_n is the symmetry plane angle of the nth order angular harmonic mode. To compactify the notation, in the following, we will drop the superscript (n) and write $\phi_{\mathbf{x}_\perp \mathbf{n}_\perp}$. We note that in accordance with Eq. (15), we will restrict ourselves to including only one anisotropic mode at a time, which means that we need not specify Ψ_n (or rather the relative angles between different symmetry planes). We leave the parameter α unspecified for analytical calculations and, if not stated otherwise, employ $\alpha = 1/2$ when presenting numerical results.

By varying the amplitude δ_n of the anistropic perturbations, we can adjust the eccentricities ϵ_n of the initial state energy distribution. Following standard procedure [66,67], the initial state eccentricities ϵ_n are determined as

$$\epsilon_n = -\frac{\int_{\mathbf{x}_\perp} x_\perp^n \epsilon(\mathbf{x}_\perp) \cos\left[n(\phi_x - \Psi_n)\right]}{\int_{\mathbf{x}_\perp} x_\perp^n \epsilon(\mathbf{x}_\perp)}, \tag{17}$$

which can be computed analytically for our form of the initial condition. Defining $\bar{\alpha} = 1 + \alpha$, the results are

$$\epsilon_n = -\delta_n \frac{n!}{2\Gamma(\frac{n}{2}+1)} \bar{\alpha}^{-n-1}. \tag{18}$$

Values of the ratio ϵ_n/δ_n for $n = 2, \ldots, 6$ in the case $\alpha = \frac{1}{2}$ are summarized in Table I, along with the maximally allowed values $\epsilon_n^{\max}$ for which a positive energy density is retained throughout the entire transverse plane.

B. Scaling properties

Based on the above setup, the development of anisotropic flow in small systems constitutes a complicated multiscale problem, which, in general, is sensitive to the

TABLE I. Eccentricities ϵ_n/δ_n and maximum allowed eccentricity $\epsilon_n^{\max}$ for which positivity of the initial energy density is satisfied.

n	2	3	4	5	6
ϵ_n/δ_n	$-\frac{8}{27}$	$-\frac{64}{81\sqrt{\pi}}$	$-\frac{64}{81}$	$-\frac{2048}{729\sqrt{\pi}}$	$-\frac{2560}{729}$
$\epsilon_n^{\max}$	0.4027	0.3845	0.3649	0.3454	0.3265

[2]Strictly speaking, the integration in Eq. (12) yields a density in $\mathrm{d}^2\mathbf{x}_\perp \mathrm{d}y$. However, in the boost-invariant case, the phase-space distribution f only depends on $y - \eta$, meaning that integration over y and η is interchangeable, and densities w.r.t. $\mathrm{d}y$ and $\mathrm{d}\eta$ are identical.

[3]Note that the anisotropic perturbations contain a variance modification factor α; a similar factor in the isotropic Gaussian could always be absorbed into the definition of R.

typical energy of quasiparticles Q_s, the total energy per unit rapidity $dE_\perp^{(0)}/d\eta$, the system size R, as well as the dimensionless coupling strength η/s. However, due to the particular simplicity of the conformal RTA in Eq. (5), the entire dependence on these quantities can be expressed in terms of a single dimensionless opacity parameter $\hat{\gamma}$ [52], as we will now demonstrate.

The starting point is the Boltzmann equation (4), in which we assume that the phase-space distribution $f(x,p)$ can be expressed as an explicit function of the curvilinear coordinates τ and $\boldsymbol{x}_\perp$, as well as of the momentum space coordinates p^τ, v_z, and ϕ_p, defined via

$$\begin{pmatrix} p^\tau \\ p^\eta \end{pmatrix} = p^\tau \begin{pmatrix} 1 \\ \tau^{-1} v_z \end{pmatrix}, \qquad \mathbf{p}_\perp = p^\tau \sqrt{1-v_z^2} \begin{pmatrix} \cos\phi_p \\ \sin\phi_p \end{pmatrix}. \tag{19}$$

In this case, the Boltzmann equation (4) reduces to [52]

$$\left(\partial_\tau + \mathbf{v}_\perp \cdot \boldsymbol{\nabla}_\perp - \frac{v_z(1-v_z^2)}{\tau}\partial_{v_z} - \frac{v_z^2 p^\tau}{\tau}\partial_{p^\tau}\right) f = -\left(5\frac{\eta}{s}\right)^{-1} T[f] v^\mu u_\mu[f](f - f_{\mathrm{eq}}[f]), \tag{20}$$

where we denote $v^\mu = p^\mu/p^\tau$, while T and u^μ are determined from the phase-space distribution f via Landau matching, as described in the previous section.

Now the general strategy to establish the scaling properties of the system is to first integrate out the momentum dependence and subsequently express all quantities in terms of dimensionless variables. Since the Landau matching condition in Eq. (7) only requires the knowledge of energy-weighted moments of the phase-space distribution, we reformulate the problem in terms of the reduced distribution,[4]

$$\mathcal{F}(\tau, \mathbf{x}_\perp; \phi_p, v_z) = \frac{\nu_{\mathrm{eff}} \pi R^2 \tau}{(2\pi)^3} \left(\frac{\mathrm{d}E_\perp^{(0)}}{\mathrm{d}\eta}\right)^{-1} \times \int_0^\infty \mathrm{d}p^\tau (p^\tau)^3 f(\tau, \mathbf{x}_\perp; p^\tau, \phi_p, v_z), \tag{21}$$

where the constant prefactor is simply chosen to cancel explicit dependencies on ν_{eff} and $\frac{\mathrm{d}E_\perp^{(0)}}{\mathrm{d}\eta}$ in the resulting equations. Since Eq. (21) takes into account the correct energy (p^τ) weighting, the energy-momentum tensor $T^{\mu\nu}$ can simply be expressed in terms of the reduced distribution as

$$T^{\mu\nu}(\tau, \mathbf{x}_\perp) = \frac{1}{\tau R^2}\frac{\mathrm{d}E_\perp^{(0)}}{\mathrm{d}\eta} \int \mathrm{d}\Omega_p v^\mu v^\nu \mathcal{F}(\tau, \mathbf{x}_\perp; \phi_p, v_z), \tag{22}$$

where $\mathrm{d}\Omega_p = \mathrm{d}v_z \mathrm{d}\phi_p$ denotes the solid angle element in momentum space. By multiplying Eq. (20) with the appropriate prefactors and performing the integration in Eq. (21), we then arrive at

$$\left(\tilde{\partial}_\tau + \vec{v}_\perp \cdot \tilde{\partial}_{\tilde{x}_\perp} - \frac{v_z(1-v_z^2)}{\tilde{\tau}}\partial_{v_z} + \frac{4v_z^2 - 1}{\tilde{\tau}}\right)\mathcal{F} = -\hat{\gamma} v^\mu u_\mu[\mathcal{F}] \tilde{\tau}^{-1/4} \tilde{T}[\mathcal{F}](\mathcal{F} - \mathcal{F}_{\mathrm{eq}}[\mathcal{F}]), \tag{23}$$

where all quantities denoted with a tilde ˜ are explicitly dimensionless and defined as follows. Dimensionless coordinates are expressed with respect to the system size R as

$$\tilde{\tau} = \tau/R, \qquad \tilde{\mathbf{x}}_\perp = \mathbf{x}_\perp/R, \tag{24}$$

while the dimensionless energy density $\tilde{\epsilon}$ and temperature $\tilde{T}$ of the system are defined according to

$$\tilde{\epsilon} = \frac{\tau\pi R^2}{dE_\perp^{(0)}/d\eta}\epsilon, \qquad \tilde{T} = \left(\frac{\tau\pi R^2 \frac{\pi^2}{30}\nu_{\mathrm{eff}}}{dE_\perp^{(0)}/d\eta}\right)^{1/4} T. \tag{25}$$

Defining the stress-energy tensor with respect to the same nondimensionalization employed for the energy density, we have

$$\tilde{T}^{\mu\nu} = \frac{\tau\pi R^2}{dE_\perp^{(0)}/d\eta} T^{\mu\nu} = \int \mathrm{d}\Omega_p v^\mu v^\nu \mathcal{F}, \tag{26}$$

such that the Landau matching condition in Eq. (7) reduces to

$$u_\nu \tilde{T}^{\mu\nu} = \tilde{\epsilon} u^\mu, \tag{27}$$

and the equation of state takes the particularly simple form $\tilde{\epsilon} = \tilde{T}^4$ in terms of the dimensionless variables. By considering the fact that the local equilibrium distribution is determined as $f_{\mathrm{eq}}(x,p) = f_{\mathrm{eq}}[p^\tau (v\cdot u)/T]$, the corresponding distribution $\mathcal{F}_{\mathrm{eq}}$ can be expressed as

$$\mathcal{F}_{\mathrm{eq}} = \frac{\nu_{\mathrm{eff}}\pi R^2 \tau}{(2\pi)^3}\left(\frac{\mathrm{d}E_\perp^{(0)}}{\mathrm{d}\eta}\right)^{-1} \frac{T^4}{(u\cdot v)^4}\int_0^\infty dx x^3 f_{\mathrm{eq}}(x), \tag{28}$$

where the last integral can be computed in terms of the energy density ϵ as $\int_0^\infty dx x^3 f_{\mathrm{eq}}(x) = \frac{(2\pi)^3 \epsilon}{4\pi\nu_{\mathrm{eff}} T^4}$, such that $\mathcal{F}_{\mathrm{eq}}$ takes the simple form,

$$\mathcal{F}_{\mathrm{eq}} = \frac{\tilde{\epsilon}}{4\pi(u\cdot v)^4}. \tag{29}$$

[4]Note that our definition for $\mathcal{F}$ differs from the one in Ref. [52] by a factor of τ, which is introduced in order to absorb trivial effects of the longitudinal expansion.

Similarly, the initial condition for $\mathcal{F}$ can also be obtained by integrating Eq. (11), where assuming an azimuthally isotropic momentum distribution, one can express $\mathcal{F}$ in terms of the initial energy density as

$$\mathcal{F}(\tilde{\tau}_0, \tilde{\mathbf{x}}_\perp, \phi_p, v_z) = \frac{\delta(v_z)}{2\pi}\tilde{\epsilon}(\tilde{\tau}_0, \tilde{\mathbf{x}}_\perp), \tag{30}$$

such that the prefactors in the definition of $\tilde{\epsilon}(\tilde{\tau}_0, \tilde{\mathbf{x}}_\perp)$ in Eq. (25) cancel with the ones in Eq. (21).

By performing the above transformations, all dependencies on the system size R, initial energy $\frac{dE_\perp^{(0)}}{d\eta}$, and number of degrees of freedom ν_{eff} have thus been subsumed into a single dimensionless opacity parameter,

$$\hat{\gamma} = \left(5\frac{\eta}{s}\right)^{-1} R^{3/4}\left(\frac{1}{\pi R^2 \frac{\pi^2}{30}\nu_{\text{eff}}}\frac{dE_\perp^{(0)}}{d\eta}\right)^{1/4}, \tag{31}$$

which appears on the right-hand side of Eq. (23) and controls the relaxation toward equilibrium. In order to get an idea of the typical magnitude of $\hat{\gamma}$, we can estimate its value as

$$\hat{\gamma} \approx 0.88\left(\frac{\eta/s}{0.16}\right)^{-1}\left(\frac{R}{0.4\text{ fm}}\right)^{1/4}\left(\frac{dE_\perp^{(0)}/d\eta}{5\text{ GeV}}\right)^{1/4}\left(\frac{\nu_{\text{eff}}}{40}\right)^{-1/4}, \tag{32}$$

which indicates that in small systems realized in $p+p$ and $p+Pb$, one should typically expect $\hat{\gamma}$ of the order unity. Conversely, in large systems, the opacity can be significantly larger, such that, e.g., in central $Pb+Pb$ collisions at LHC energies, one obtains

$$\hat{\gamma} \approx 9.2\left(\frac{\eta/s}{0.16}\right)^{-1}\left(\frac{R}{6\text{ fm}}\right)^{1/4}\left(\frac{dE_\perp^{(0)}/d\eta}{4000\text{ GeV}}\right)^{1/4}\left(\frac{\nu_{\text{eff}}}{40}\right)^{-1/4}. \tag{33}$$

Based on a combination of (semi)analytic and numerical studies, we will therefore explore the full range of opacities $\hat{\gamma} \ll 1$, $\hat{\gamma} \sim 1$ and $\hat{\gamma} \gg 1$ in order to investigate possible changes in the reaction dynamics for small and large systems.

C. Observables

Before we discuss the details of the solution of the previously stated problem, it is instructive to introduce the observables, which we will use to quantify the time evolution of the system and the development of transverse flow. Below, we will define all observables in terms of the original phase space density f and additionally express them in terms of the shorthand notation $\langle\cdot\rangle$ that was previously introduced in (10). Based on the above discussion, we will restrict ourselves to energy-weighted observables, which can be formulated in terms of moments of the reduced distribution $\mathcal{F}$ as

$$\langle (p^\tau)^2 \mathcal{O}(v_z, \phi_p)\rangle = \frac{1}{\pi R^2}\frac{dE_\perp^{(0)}}{d\eta}\int d\Omega_p \mathcal{O}(v_z, \phi_p)\mathcal{F}. \tag{34}$$

One of the basic observables to look at is the transverse energy per unit rapidity $dE_\perp/d\eta$, computed via

$$\frac{dE_\perp}{d\eta} = \nu_{\text{eff}}\tau^2\int_{\mathbf{x}_\perp}\int\frac{d^3p}{(2\pi)^3}p_\perp f = \tau\int_{\mathbf{x}_\perp}\left\langle (p^\tau)^2\sqrt{1-v_z^2}\right\rangle, \tag{35}$$

whose decrease in time is a measure of the work performed against the longitudinal expansion of the system. Since we are interested in azimuthal momentum anisotropies, the most important observables are the flow harmonics v_n, given as the normalized Fourier modes of the particle distribution in the azimuthal momentum angle [68,69]. We note that, in accordance with the above discussion, we also weight the v_n's with the transverse momentum $p_\perp$ to acquire an energy-weighted version of these flow harmonics; i.e., we will study the moments,

$$v_n^E = \frac{\int_{\mathbf{x}_\perp}\int\frac{d^3p}{(2\pi)^3}p_\perp e^{in\phi_p}f}{\int_{\mathbf{x}_\perp}\int\frac{d^3p}{(2\pi)^3}p_\perp f} = \frac{\int_{\mathbf{x}_\perp}\langle (p^\tau)^2\sqrt{1-v_z^2}e^{in\phi_p}\rangle}{\int_{\mathbf{x}_\perp}\langle (p^\tau)^2\sqrt{1-v_z^2}\rangle}. \tag{36}$$

Beyond the v_n^Es, which describe azimuthal anisotropies of the momentum distribution, another energy-weighted elliptic momentum anisotropy can also be defined on the level of $T^{\mu\nu}$ without the need of full knowledge of f. Explicitly, this elliptic anisotropy of the energy flow ϵ_p is defined as [70–72]

$$\epsilon_p = \frac{\int_{\mathbf{x}_\perp}(T^{11}-T^{22}+2iT^{12})}{\int_{\mathbf{x}_\perp}(T^{11}+T^{22})} = \frac{\int_{\mathbf{x}_\perp}\langle (p^\tau)^2(1-v_z^2)e^{2i\phi_p}\rangle}{\int_{\mathbf{x}_\perp}\langle (p^\tau)^2(1-v_z^2)\rangle}, \tag{37}$$

and we will employ this measure in Sec. V C to compare the kinetic evolution to relativistic viscous hydrodynamics in order to avoid possible ambiguities of the freeze-out prescription.

III. SOLUTION TO LINEAR ORDER IN OPACITY $\hat{\gamma}$ AND ECCENTRICITY ϵ_n

While the Boltzmann equation (4) as an integro-differential equation is in general too complicated to solve analytically, important conclusions can be obtained in the weakly interacting regime close to free streaming, which corresponds to the limit $\hat{\gamma} \to 0$. We are primarily interested in the development of anisotropic flow, i.e., the final state momentum space anisotropy quantified by the harmonic

coefficients v_n, in response to the initial state coordinate space eccentricity quantified by the amplitudes ϵ_n (or equivalently δ_n) of the harmonic perturbations introduced in Eq. (15). Starting from the free-streaming regime, where there is no production of v_n, we seek to follow previous works [48–50,53–55] in deriving analytical expressions for $v_n(\tilde{\tau})$, which are accurate to linear order for small $\hat{\gamma}$ and small ϵ_n.

Since in the free-streaming system, the momenta of the particles remain unchanged, the free-streaming dynamics is effectively $2+1$-dimensional, and we will continue to work in spatial Milne coordinates, where, in contrast to other sections, we use y for longitudinal momentum parametrization instead of p^η or v_z. Another feature is that the analytical setup will quite straightforwardly also allow one to treat the problem more generally without restricting it to energy-weighted degrees of freedom. However, this requires one to specify the initial condition in (11) in more detail—in particular, with regards to the initial momentum distribution $\mathrm{d}N_0/\mathrm{d}^2\mathbf{x}_\perp\mathrm{d}^2\mathbf{p}_\perp\mathrm{d}y$, which will introduce additional scales that non-energy-weighted degrees of freedom will depend on. We will assume that this distribution is (initially) isotropic in transverse momentum and depends only on some nonspecific but fixed function F of the ratio of $p_\perp$ to the momentum scale $Q_s(\mathbf{x}_\perp)$; i.e.,

$$\frac{\mathrm{d}N_0}{\mathrm{d}^2\mathbf{x}_\perp\mathrm{d}^2\mathbf{p}_\perp\mathrm{d}y} = F\left(\frac{Q_s(\mathbf{x}_\perp)}{p_\perp}\right), \tag{38}$$

where the characteristic energy scale $Q_s(\mathbf{x}_\perp)$ is related to the local energy density $\epsilon(\tau_0,\mathbf{x}_\perp)$ via Eq. (12).

Below, we outline the calculation of observables to leading order in an expansion in opacity $\hat{\gamma}$ and eccentricity ϵ_n and quote the results for the flow harmonics v_n and the longitudinal cooling of $dE_\perp/d\eta$. Details of the analytic calculation are compiled in Appendices A–C.

A. Expansion scheme

To linearize the solution in opacity, we expand around the free-streaming limit corresponding to zero opacity, denoted as $f^{(0)}$, which satisfies

$$p^\mu\partial_\mu f^{(0)} = 0. \tag{39}$$

The first order correction $f^{(1)}$ is obtained by computing the effect of the first scattering of each particle, with the scattering rates determined by the zeroth order result,

$$p^\mu\partial_\mu f^{(1)} = C[f^{(0)}]. \tag{40}$$

This type of expansion was conceptualized in [48,49] and has recently also been used in other works examining weakly interacting systems [50,53–55]. As reasoned in the previous section, we can factor out from $C[f]$ the opacity parameter $\hat{\gamma}$ as a proportionality constant containing all parametric dependencies. Therefore, $\hat{\gamma}$ can be identified as the expansion parameter of this expansion scheme. In the following, we will denote observables X computed in the free-streaming limit as $X^{(0)}$ and their first order corrections in opacity by $X^{(1)}$.

Similarly, for the expansion in eccentricity, we recall from Sec. II A that the initial energy density is of the form,

$$\epsilon(\tau_0,\mathbf{x}_\perp) = \bar{\epsilon}(\tau_0,x_\perp) + \delta\epsilon(\tau_0,\mathbf{x}_\perp), \tag{41}$$

with isotropic $\bar{\epsilon}$ and purely anisotropic $\delta\epsilon$, which introduces a finite eccentricity ϵ_n. Evidently, in free streaming, the isotropic and anisotropic components of the phase-space distribution f evolve independently of each other, and the anisotropic perturbation can be computed exactly. However, when computing the induced changes of the phase-space distribution $f^{(1)}$, one is required to perform the Landau matching at the level of the full energy-momentum tensor emerging from $f^{(0)}$, which introduces a nontrivial coupling of the isotropic and anisotropic components. Hence, for simplicity, we will solve the corresponding eigenvalue equation only to linear order in the anisotropic perturbations, which formally corresponds to a leading order expansion in ϵ_n. In the following, we will denote the linearized corrections to observables X due to the anisotropic perturbation as δX.

B. Observables

Since we want to examine momentum anisotropies, all observables of interest will be derived from the momentum distribution $\frac{\mathrm{d}N}{\mathrm{d}^2p_\perp\mathrm{d}y}$, which can be obtained from the phase space density f by integrating over coordinate space variables. Specifically in Milne coordinates, the four-volume transformation entails an extra functional determinant for the 3D hypersurface integration at fixed proper time τ, such that

$$\frac{\mathrm{d}N}{\mathrm{d}^2\mathbf{p}_\perp\mathrm{d}y} = \frac{\nu_{\mathrm{eff}}}{(2\pi)^3}\int_{\mathbf{x}_\perp}\int \mathrm{d}\eta p_\perp\tau\cosh(y-\eta)f. \tag{42}$$

Based on the momentum distribution $\frac{\mathrm{d}N}{\mathrm{d}^2p_\perp\mathrm{d}y}$, we will extract the following moments[5]:

[5]Note that, in contrast to the different treatments described in the other sections, the analytical treatment allows one to describe more than just the energy-weighted version of the flow harmonics. Nevertheless, there are two important reasons for extracting moments of the distributions, rater than differential observables such as $\frac{\mathrm{d}N}{\mathrm{d}^2p_\perp\mathrm{d}y}$ or $v_n(p_\perp)$. The first is that the integral over $p_\perp$ will be crucial in facilitating further analytical integrations later on, but perhaps the more convincing reason is the aforementioned simplification of the problem when restricting it to the case of $m=1$ for the energy-weighted observables.

$$V_{mn} = \int_{\mathbf{p}_\perp} e^{in\phi_{\mathbf{p}_\perp}} p_\perp^m \frac{\mathrm{d}N}{\mathrm{d}^2\mathbf{p}_\perp \mathrm{d}y} = \int_{\mathbf{x}_\perp} \langle p^\tau p_\perp^m e^{in\phi_p} \rangle, \quad (43)$$

which can be directly related to the observables that are of interest to us. Specifically, one has $\frac{\mathrm{d}E_\perp}{\mathrm{d}\eta} = V_{10}$ and $v_n^E = \frac{V_{1n}}{V_{10}}$.

C. Free-streaming solution

The free-streaming solution of (39) can be computed, e.g., via the method of characteristics to be

$$f^{(0)}(\tau, \mathbf{x}_\perp, \mathbf{p}_\perp, y-\eta) = f^{(0)}\Bigg(\tau_0, \mathbf{x}_\perp - \mathbf{v}_\perp t(\tau, \tau_0, y-\eta), \mathbf{p}_\perp, \operatorname{arcsinh}\left(\frac{\tau}{\tau_0}\sinh(y-\eta)\right)\Bigg), \quad (44)$$

where $\mathbf{v}_\perp = \mathbf{p}_\perp/|\mathbf{p}_\perp|$, and

$$t(\tau, \tau_0, y-\eta) = \tau\cosh(y-\eta) - \sqrt{\tau_0^2 + \tau^2\sinh^2(y-\eta)}. \quad (45)$$

We note that the free-streaming result simplifies significantly for $f^{(0)}(\tau_0, \mathbf{x}_\perp, \mathbf{p}_\perp, y-\eta) \propto \delta(y-\eta)$, as in this case,

$$\delta\left(\operatorname{arcsinh}\left(\frac{\tau}{\tau_0}\sinh(y-\eta)\right)\right) = \frac{\tau_0}{\tau}\delta(y-\eta), \quad (46)$$

and

$$t(\tau, \tau_0, 0) = \tau - \tau_0 = \Delta\tau. \quad (47)$$

By applying this simplification to our initial condition in Eq. (11), we obtain

$$f^{(0)}(\tau, \mathbf{x}_\perp, \mathbf{p}_\perp, y-\eta) = \frac{(2\pi)^3}{\nu_{\mathrm{eff}}}\frac{\delta(y-\eta)}{\tau p_\perp} F\left(\frac{Q_s(\mathbf{x}_\perp - \mathbf{v}_\perp\Delta\tau)}{p_\perp}\right). \quad (48)$$

Evidently, the free-streaming evolution will not change the momentum distribution $\frac{\mathrm{d}N}{\mathrm{d}^2 p_\perp \mathrm{d}y}$ since there are no scatterings, and therefore, also the moments $V_{mn}^{(0)}$ will remain constant,

$$V_{m,n=0}^{(0)}(\tau) = V_{m,n=0}^{(0)}(\tau_0), \qquad V_{m,n>0}^{(0)}(\tau) = 0, \quad (49)$$

where the last equality follows by noting that the initial condition is isotropic in momentum space. Subsequently, all v_n^Es with $n \neq 0$ vanish identically at all times τ, while the energy per unit rapidity remains constant,

$$v_n^{E,(0)} = 0, \qquad \frac{dE_\perp^{(0)}}{d\eta}(\tau) = \frac{dE_\perp}{d\eta}(\tau_0). \quad (50)$$

D. Landau matching

Next, the free-streaming result can be used to compute the energy-momentum tensor of the isotropic background $T^{(0)\mu\nu}$ and its anisotropic perturbations $\delta T^{(0)\mu\nu}$, which will be needed to obtain the local thermodynamic variables that enter the collision integral $C[f]$. Defining

$$v_\perp^\mu = p^\mu/p_\perp|_{y-\eta=0} = (1, \mathbf{v}_\perp, 0), \quad (51)$$

the isotropic part $T^{(0)\mu\nu}$ of the energy-momentum tensor is given by

$$T^{(0)\mu\nu} = \frac{\tau_0}{\tau}\int\frac{\mathrm{d}\phi_p}{2\pi} v_\perp^\mu v_\perp^\nu \bar{\epsilon}(\tau_0, \mathbf{x}_\perp - \Delta\tau\mathbf{v}_\perp). \quad (52)$$

Due to isotropy, it has only four independent entries and can be written as

$$T^{(0)\mu\nu} = \begin{pmatrix} T^{(0)\tau\tau} & T^{(0)\tau\perp}\hat{\mathbf{x}}_\perp^t & 0 \\ T^{(0)\tau\perp}\hat{\mathbf{x}}_\perp & T^{(0)\mathbb{1}}\mathbb{1} + T^{(0)\perp\perp}\hat{\mathbf{x}}_\perp\hat{\mathbf{x}}_\perp^t & 0 \\ 0 & 0 & 0 \end{pmatrix}, \quad (53)$$

where we denote $\hat{\mathbf{x}}_\perp = \mathbf{x}_\perp/|\mathbf{x}_\perp|$. $T^{(0)\mu\nu}$ has eigenvectors u^μ, t^μ and s^μ satisfying the relations,

$$u_\mu T^{(0)\mu\nu} = \epsilon u^\nu, \quad (54)$$

$$t_\mu T^{(0)\mu\nu} = p_t t^\nu, \quad (55)$$

$$s_\mu T^{(0)\mu\nu} = p_s s^\nu. \quad (56)$$

Based on its symmetries, these eigenvectors can be parametrized as

$$u^\mu = \gamma(1, \beta\hat{\mathbf{x}}_\perp, 0), \quad (57)$$

$$t^\mu = \gamma(\beta, \hat{\mathbf{x}}_\perp, 0), \quad (58)$$

$$s^\mu = (0, i\sigma_2\hat{\mathbf{x}}_\perp, 0), \quad (59)$$

where

$$\beta = \frac{3T^{(0)\tau\tau} + T^{(0)\perp\perp}}{4T^{(0)\tau\perp}} - \sqrt{\left(\frac{3T^{(0)\tau\tau} + T^{(0)\perp\perp}}{4T^{(0)\tau\perp}}\right)^2 - 1} \quad (60)$$

is the local rest-frame velocity, $\gamma = (1-\beta^2)^{-1/2}$ and $i\sigma_2 = \left(\begin{smallmatrix} 0 & 1 \\ -1 & 0 \end{smallmatrix}\right)$; the corresponding eigenvalues are given by

$$\epsilon = T^{(0)\tau\tau} - \beta T^{(0)\tau\perp}, \quad (61)$$

$$p_t = \beta T^{(0)\tau\perp} - T^{(0)\perp\perp} - T^{(0)\mathbb{1}}, \quad (62)$$

$$p_s = -T^{(0)\mathbb{1}}. \quad (63)$$

Now, similarly to the isotropic background in Eq. (52), the anisotropic part of the energy-momentum tensor can be computed as

$$\delta T^{(0)\mu\nu} = \frac{\tau_0}{\tau}\int \frac{\mathrm{d}\phi_p}{2\pi} v_\perp^\mu v_\perp^\nu \delta\epsilon(\tau_0, \mathbf{x}_\perp - \Delta\tau \mathbf{v}_\perp), \quad (64)$$

which—due to the absence of isotropy—features six independent entries, and its eigenvalues and eigenvectors will be a complicated function of all of them. Obtaining their exact result would be cumbersome and ultimately pointless, as it would be too complex to perform further calculations with them, so instead, we will linearize the Landau matching condition in the perturbation, meaning that the corrections $\delta\epsilon$ and δu^μ are computed from

$$\delta u_\mu T^{(0)\mu\nu} + u_\mu \delta T^{(0)\mu\nu} = \delta\epsilon u^\mu + \epsilon\delta u^\mu, \quad (65)$$

$$u_\mu \delta u^\mu = 0. \quad (66)$$

The second condition ensures that the perturbation preserves the correct normalization of u^μ to linear order. In order to solve this system of equations, we can expand

$$\delta u^\mu = \delta u_t t^\mu + \delta u_s s^\mu \quad (67)$$

and use the orthogonality of the eigenbasis of $T^{(0)\mu\nu}$ to obtain via contraction with the eigenvectors from (65) the following results:

$$\delta\epsilon = u_\mu \delta T^{(0)\mu\nu} u_\nu, \quad (68)$$

$$\delta u_t = \frac{u_\mu \delta T^{(0)\mu\nu} t_\nu}{p_t - \epsilon}, \quad (69)$$

$$\delta u_s = \frac{u_\mu \delta T^{(0)\mu\nu} s_\nu}{p_s - \epsilon}. \quad (70)$$

While Eqs. (61)–(63) and (68)–(70) provide schematic expressions for the $\epsilon, \delta\epsilon, u^\mu$, and δu^μ, the exact forms of $T^{(0)\mu\nu}$ and $\delta T^{(0)\mu\nu}$ that determine these quantities consist of lengthy expressions, which are provided in Appendix B.

E. First order corrections in $\hat{\gamma}$

Now that we have obtained the local energy densities and flow velocities, computing the corrections $\delta f^{(1)}$ due to the first scatterings according to

$$\frac{p^\mu}{p^\tau}\partial_\mu f^{(1)} = \frac{C[f^{(0)}]}{p^\tau} \quad (71)$$

is comparatively straightforward after realizing that this is just the inhomogeneous case of the PDE we already solved for free streaming. The solution (44) allows one to read off the Green's function for propagation in time and compute $f^{(1)}$ via

$$f^{(1)}(\tau, \mathbf{x}_\perp, \mathbf{p}_\perp, y-\eta) = \int_{\tau_0}^{\tau} \mathrm{d}\tau' \frac{C[f^{(0)}]}{p^\tau}\left(\tau', \mathbf{x}_\perp - \mathbf{v}_\perp t(\tau,\tau', y-\eta), \mathbf{p}_\perp, \operatorname{arcsinh}\left(\frac{\tau}{\tau'}\sinh(y-\eta)\right)\right). \quad (72)$$

Since we will integrate over space to compute $\frac{\mathrm{d}N^{(1)}}{\mathrm{d}^2 p_\perp \mathrm{d}y}$ according to (42), we can simplify this expression by performing the following substitutions:

$$\mathbf{x}_\perp{}' = \mathbf{x}_\perp - \mathbf{v}_\perp t(\tau,\tau', y-\eta), \qquad \eta' = y - \operatorname{arcsinh}\left(\frac{\tau}{\tau'}\sinh(y-\eta)\right), \quad (73)$$

such that

$$\mathrm{d}^2\mathbf{x}_\perp{}' = \mathrm{d}^2\mathbf{x}_\perp, \qquad \mathrm{d}\eta' = \frac{\tau}{\tau'}\frac{\cosh(y-\eta)}{\cosh(y-\eta')}\mathrm{d}\eta, \quad (74)$$

yielding the following result for the changes in the momentum space distribution $\frac{\mathrm{d}N^{(1)}}{\mathrm{d}^2 p_\perp \mathrm{d}y}$:

$$\frac{\mathrm{d}N^{(1)}}{\mathrm{d}^2 p_\perp \mathrm{d}y}(\tau, \mathbf{p}_\perp) = \int_{\tau_0}^{\tau}\mathrm{d}\tau' \int_{\mathbf{x}_\perp{}'}\int \mathrm{d}\eta' \tau' \frac{\nu_{\mathrm{eff}}}{(2\pi)^3} \times C[f^{(0)}](\tau', \mathbf{x}_\perp{}', \mathbf{p}_\perp, y-\eta'), \quad (75)$$

where, in the following, we will drop the primes on all integration variables except for τ'. Since, as stated in Sec. III B, the final observables we want to compute correspond to $\mathrm{d}^2 p_\perp$-integrated moments of $\frac{\mathrm{d}N}{\mathrm{d}^2 p_\perp \mathrm{d}y}$, one is then left with the calculation of the following six-dimensional integral,

$$V^{(1)}_{mk}(\tau) = \int_{\mathbf{p}_\perp} e^{ik\phi_p} p_\perp^m \int_{\tau_0}^{\tau}\mathrm{d}\tau' \int_{\mathbf{x}_\perp}\int \mathrm{d}\eta \tau' \frac{\nu_{\mathrm{eff}}}{(2\pi)^3} \times C[f^{(0)}](\tau', \mathbf{x}_\perp, \mathbf{p}_\perp, y-\eta). \quad (76)$$

We find that four of these integrals can be carried out analytically, while the remaining two integrals over $\mathrm{d}\tau'$ and $\mathrm{d}x_\perp$ require numerical methods. Below, we provide a brief outline of the four analytical integrations and explain how different terms can be categorized. Explicit expressions and further details of the analytic calculation can be found in Appendix C.

The integration over $p_\perp$ is performed first to obtain moments of F and f_{eq}, which will facilitate the other integrations. Since the integrand depends mostly on $u\cdot v$, we substitute integration over the position space azimuthal angle ϕ_x for integration over $\phi_{\mathbf{x}_\perp\mathbf{p}_\perp} = \phi_x - \phi_p$. The integral over η is straightforward for the term containing a Dirac delta, but for other terms, it is of similar complexity to the integral over $\phi_{\mathbf{x}_\perp\mathbf{p}_\perp}$, and both are performed together.

After these integrations, the only remaining dependence on the azimuthal momentum angle takes the form, $e^{ik\phi_p}\cos(n\phi_{\mathbf{p}_\perp\mathbf{n}_\perp})$ ($\phi_{\mathbf{p}_\perp\mathbf{n}_\perp}=\phi_p-\Psi_n$), and the last integral becomes a trigonometric orthogonality relation, which signifies that eccentricities do not mix, as is to be expected due to the linearization.

Due to the fact that we consider an isotropic background with a purely anisotropic perturbation, the leading order expansion of the flow harmonics is given by

$$v_n^{(m)}=\frac{V_{mn}}{V_{m0}}=\frac{\delta V_{mn}^{(1)}}{V_{m0}^{(0)}}+\text{nonlinear terms}. \tag{77}$$

Due to this symmetry, one also finds that the leading order opacity contributions to the observables V_{mn} conveniently separate into the first order isotropic corrections $V_{m0}^{(1)}\propto\hat{\gamma}$ for $n=0$ on one hand and the first order anisotropic corrections $\delta V_{mn}^{(1)}\propto\hat{\gamma}\delta_n$ to only moments with $n\neq 0$ on the other hand. While the former ($V_{m0}^{(1)}$) represent opacity corrections to the evolution of the isotropic background, the latter ($\delta V_{mn}^{(1)}$) describe the systems' response to the anisotropic energy perturbations.

We also make the mathematically as well as physically relevant distinction between terms $V_{mn}^{(1,0)}$ coming from the decay of $f^{(0)}$ and terms $V_{mn}^{(1,\,\mathrm{eq})}$ coming from the buildup of f_{eq}. In our calculation, we treat these terms separately and then sum them to find the total observable. However, it is important to point out that in many cases, the two terms turn out to have different parametric dependencies. By construction of the expansion scheme, all of them are proportional to $\hat{\gamma}$. However, due to the different functional forms of $f^{(0)}$ and f_{eq}, we obtain that the isotropic ($n=0$) corrections are given by

$$V_{m0}^{(1,0)}=-\hat{\gamma}V_{m0}^{(0)}\mathcal{P}_m(\tilde{\tau}), \tag{78}$$

$$V_{m0}^{(1,\mathrm{eq})}=+\hat{\gamma}\nu_{\mathrm{eff}}R^{-m}\left(\nu_{\mathrm{eff}}^{-1}\frac{\mathrm{d}E_\perp^{(0)}}{\mathrm{d}\eta}R\right)^{\frac{m+3}{4}}\mathcal{Q}_m(\tilde{\tau}), \tag{79}$$

and similarly, for the anistropic corrections ($n\neq 0$),

$$V_{mn}^{(1,0)}=-\hat{\gamma}\delta_n V_{m0}^{(0)}\mathcal{P}_{mn}(\tilde{\tau}), \tag{80}$$

$$V_{mn}^{(1,\mathrm{eq})}=+\hat{\gamma}\delta_n\nu_{\mathrm{eff}}R^{-m}\left(\nu_{\mathrm{eff}}^{-1}\frac{\mathrm{d}E_\perp^{(0)}}{\mathrm{d}\eta}R\right)^{\frac{m+3}{4}}\mathcal{Q}_{mn}(\tilde{\tau}). \tag{81}$$

Detailed expressions of the functions $\mathcal{P}_m(\tilde{\tau})$, $\mathcal{Q}_m(\tilde{\tau})$, $\mathcal{P}_{mn}(\tilde{\tau})$, $\mathcal{Q}_{mn}(\tilde{\tau})$ are given in Eqs. (C17), (C22), (C42), and (C61). Of course, the appearance of a different parametric behavior is not too surprising, as f^0 depends on the entire momentum distribution, whereas f_{eq} only depends on the local energy density. Generally, to fix the relative size of decay and buildup for $V_{mn}^{(1)}$, we need an input for $\frac{\mathrm{d}E_\perp^{(0)}}{\mathrm{d}\eta}$ and $V_{m0}^{(0)}$, which means specifying the related moments of the initial momentum distribution F in Eq. (38). In general, $\mathcal{Q}_m$ and $\mathcal{Q}_{mn}$ depend on the details of the equilibrium distribution f_{eq}, which we choose for definiteness to be the Bose-Einstein distribution (for more details, we refer the reader to Appendix C). Clearly, the only exception to this rule is the case $m=1$ of energy-weighted observables, where $V_{10}^{(0)}=\frac{\mathrm{d}E_\perp^{(0)}}{\mathrm{d}\eta}$, and the calculation of $V_{1n}^{(1)}/V_{10}^{(0)}$ does not require any further specification of the initial momentum distribution F.

By restricting our attention to energy-weighted observables, we can then perform the residual integrals numerically to obtain the leading order changes in the initial energy per unit rapidity,

$$\frac{\mathrm{d}E_\perp^{(1)}}{d\eta}(\tau\to\infty)\Big/\left(\hat{\gamma}\frac{\mathrm{d}E_\perp^{(0)}}{\mathrm{d}\eta}\right)=-0.210, \tag{82}$$

and the flow response,

$$v_2^E(\tau\to\infty)/(\hat{\gamma}\epsilon_2)=0.212 \tag{83}$$

$$v_3^E(\tau\to\infty)/(\hat{\gamma}\epsilon_3)=0.0665 \tag{84}$$

$$v_4^E(\tau\to\infty)/(\hat{\gamma}\epsilon_4)=-0.00914, \tag{85}$$

which we will compare to full numerical solutions of the RTA Boltzmann equation in the following. Beyond the results in Eqs. (82)–(85), which provide the asymptotic ($\tau\to\infty$) values of the transverse energy and flow coefficients, it is clear that Eq. (76) also gives access to the time evolution of these quantities, which we will further investigate in Sec. V.

We note that the above results are obtained for the initial condition in Eqs. (13)–(15) with $\alpha=1/2$, which is different than the case $\alpha=0$ considered in [53]. If we choose $\alpha=0$ instead, we find

$$v_2^E(\tau\to\infty)/(\hat{\gamma}\epsilon_2)=0.213 \tag{86}$$

$$v_3^E(\tau\to\infty)/(\hat{\gamma}\epsilon_3)=0.0621 \tag{87}$$

$$v_4^E(\tau\to\infty)/(\hat{\gamma}\epsilon_4)=-0.00483, \tag{88}$$

in agreement with [53].[6] By comparing the results for different v_ns in Eqs. (83)–(85) and (86)–(88), one finds that v_2 appears to be rather insensitive to α, whereas the higher order v_ns are more sensitive to α, as we will further discuss in Sec. V B. Especially, v_4 changes by approximately a factor of 2 between the two cases, and can even turn out to have different signs for different values of α, indicating a strong dependence on the initial profile in the low opacity regime.

[6]Note that for comparison with [53], one also needs to account for the factor of ϵ_n/δ_n in Eq. (18).

IV. NUMERICAL PROCEDURE FOR NON-LINEAR SOLUTION

We will now discuss two different schemes to obtain numerical solutions of the RTA Boltzmann equation, which are based on a momentum moment expansion discussed in Sec. IV A and the relativistic Lattice Boltzmann (RLB) method discussed in Sec. IV B.

A. Expansion in spherical harmonic moments

Within our first approach, we follow previous works [73], where instead of describing the evolution of the phase space density f, the numerical algorithm solves time evolution equations only for some energy-weighted momentum moments on a two-dimensional lattice in transverse space. Specifically, we consider the following energy-weighted moments C_l^m of the phase-space distribution:

$$C_l^m \coloneqq \tau^2 \int \frac{\mathrm{d}^3 p}{(2\pi)^3} Y_l^m(\theta_p, \phi_p) p^\tau f = \int \frac{\mathrm{d}^2 p_\perp}{(2\pi)^2} \int \frac{\mathrm{d}p_\eta}{2\pi} Y_l^m(\theta_p, \phi_p) \sqrt{p_\perp^2 + \frac{p_\eta^2}{\tau^2}} f, \tag{89}$$

where Y_l^m denote the spherical harmonics, which are given in terms of the associated Legendre polynomials P_l^m as

$$Y_l^m(\theta, \phi) = y_l^m P_l^m(\cos\theta) e^{im\phi}, \tag{90}$$

with normalization

$$y_l^m = \sqrt{\frac{2l+1}{4\pi} \frac{(l-m)!}{(l+m)!}}, \tag{91}$$

and the momentum space angles in Eq. (89) are parametrized by the polar and azimuthal angles θ_p and ϕ_p defined as

$$\cos\theta_p = \frac{p_\eta/\tau}{p^\tau}, \qquad \tan\phi_p = \frac{p^2}{p^1}. \tag{92}$$

Since only a finite number of moments can be described numerically, the algorithm only keeps track of the moments with $l < l_{\max}$ for an adjustable large enough value of $l_{\max}$ to achieve apparent convergence.

1. Initial conditions and evolution equation for moments

By taking the corresponding moments of the initial conditions in Eq. (11), one obtains the initial conditions for the spherical harmonic moments as

$$C_l^m(\tau_0) = \tau_0 \epsilon(\tau_0, \mathbf{x}_\perp) y_l^0 P_l^0(0) \delta^{m0}. \tag{93}$$

This expression contains as a factor the Legendre polynomial evaluation $P_l^0(0)$, which vanishes for odd l and is otherwise given by

$$P_l^0(0) = (-1)^{l/2} \pi^{-1/2} \frac{\Gamma(\frac{l+1}{2})}{\Gamma(\frac{l}{2}+1)}. \tag{94}$$

Similarly, denoting the local rest-frame velocity as $u^\mu = \gamma(1, \beta_1, \beta_2, 0)$ and taking the corresponding moments of the Boltzmann equation (4), (5) then yields the following equation of motion for the spherical harmonic moments:

$$\begin{aligned}\partial_\tau C_l^m = {} & \frac{1}{\tau}(b_{l,+2}^m C_{l+2}^m + b_{l,0}^m C_l^m + b_{l,-2}^m C_{l-2}^m) + \frac{1}{2}\left(\frac{\gamma\beta_1}{\tau_R} - \partial_1\right)[u_{l,+}^m C_{l+1}^{m+1} + u_{l,-}^m C_{l-1}^{m+1} + d_{l,+}^m C_{l+1}^{m-1} + d_{l,-}^m C_{l-1}^{m-1}] \\ & + \frac{1}{2i}\left(\frac{\gamma\beta_2}{\tau_R} - \partial_2\right)[u_{l,+}^m C_{l+1}^{m+1} + u_{l,-}^m C_{l-1}^{m+1} - d_{l,+}^m C_{l+1}^{m-1} - d_{l,-}^m C_{l-1}^{m-1}] + \frac{1}{\tau_R} E_l^m(u^\mu, T) - \frac{\gamma}{\tau_R} C_l^m,\end{aligned} \tag{95}$$

where the terms with spatial derivatives proportional to the coefficients u, d describe free streaming, while the terms proportional to the coefficients b are related to the longitudinal expansion. The corresponding coefficients are given by [73][7]

$$u_{l,-}^m = \sqrt{\frac{(l-m)(l-m-1)}{4l^2-1}}, \qquad u_{l,+}^m = -\sqrt{\frac{(l+m+1)(l+m+2)}{4l(l+2)+3}}, \tag{96}$$

$$d_{l,-}^m = -\sqrt{\frac{(l+m)(l+m-1)}{4l^2-1}}, \qquad d_{l,+}^m = \sqrt{\frac{(l-m+1)(l-m+2)}{4l(l+2)+3}}, \tag{97}$$

[7]Note that here $b_{l,0}^m$ is smaller by $\frac{1}{3}$ compared to [73] because the C_l^m are weighted with τ instead of $\tau^{4/3}$.

$$b^m_{l,-2} = -\frac{l+2}{2l-1}\sqrt{\frac{(l-m)(l-m-1)(l+m)(l+m-1)}{(2l-3)(2l+1)}}, \qquad b^m_{l,0} = \frac{1-3(l^2-l)+5m^2}{4l(l+1)-3},$$
$$b^m_{l,+2} = \frac{l-1}{2l+3}\sqrt{\frac{(l-m+1)(l-m+2)(l+m+2)(l+m+1)}{(2l+5)(2l+1)}}. \tag{98}$$

Finally, all terms that are inversely proportional to the relaxation time τ_R result from the collision kernel and describe the relaxation of the system toward local equilibrium, with the equilibrium moments E^l_m given by

$$E^m_l = \int \frac{\mathrm{d}^2 p_\perp}{(2\pi)^2}\int \frac{\mathrm{d}p_\eta}{2\pi} Y^m_l(\theta_p,\phi_p) p^\mu u_\mu f_{\mathrm{eq}} = 2^{-l-2}\pi^{1/2}\tau\epsilon Y^m_l\left(\frac{\pi}{2},\phi_u\right)\gamma^{-3}\beta^l\frac{\Gamma(l+3)}{\Gamma(l+\frac{3}{2})}{}_2F_1\left(\frac{l+3}{2},\frac{l+4}{2};l+\frac{3}{2};\beta^2\right), \tag{99}$$

where we denote $\tan\phi_u = \beta_2/\beta_1$ and $\beta^2 = \beta_1^2+\beta_2^2$ and refer to Appendix D for further details of the calculation. We also note for later convenience that by separately keeping track of the free streaming longitudinal expansion and collisional contributions in Eq. (95), we can compute the respective contributions to the rate of change of any observables.

Evaluation of Eq. (95) also requires an input for the local energy density ϵ and flow velocity u^μ, which have to be computed via Landau matching. In practice, we first compute the various components of the energy-momentum tensor from the following linear combinations of spherical harmonic moments,

$$\tau T^{\tau\tau} = \sqrt{4\pi}C^0_0 \tag{100}$$

$$\tau T^{\tau 1} = \sqrt{\frac{2\pi}{3}}(C^{-1}_1 - C^1_1) \tag{101}$$

$$\tau T^{\tau 2} = \sqrt{\frac{2\pi}{3}}i(C^{-1}_1 + C^1_1) \tag{102}$$

$$\tau T^{11} = \sqrt{\frac{4\pi}{9}}\left(C^0_0 - \sqrt{\frac{1}{5}}C^0_2\right) + \sqrt{\frac{2\pi}{15}}(C^2_2 + C^{-2}_2) \tag{103}$$

$$\tau T^{22} = \sqrt{\frac{4\pi}{9}}\left(C^0_0 - \sqrt{\frac{1}{5}}C^0_2\right) - \sqrt{\frac{2\pi}{15}}(C^2_2 + C^{-2}_2) \tag{104}$$

$$\tau T^{12} = \sqrt{\frac{2\pi}{15}}i(C^{-2}_2 - C^2_2), \tag{105}$$

and subsequently perform a numerical diagonalization of T^μ_ν using the EIGEN C++ library [74] to obtain the rest-frame velocity u^μ and local energy density ϵ as the timelike eigenvector and eigenvalue.

With regards to the numerical implementation of Eq. (95), we also note that the terms containing spatial derivatives can be efficiently computed in Fourier space, and we employ an $\mathcal{O}(a_S^2)$ improved five-point stencil derivative. Concerning the discretization of the time step, we employ a fourth order Runge-Kutta scheme with adaptive time step of typically $\delta\tau = 0.01\ \min(\tau, R/10)$.

2. Observables

Since the numerical setup is restricted to energy-weighted moments of the phase-space distribution, all observables that can be computed are necessarily weighted with energy as well. Evidently, to compute an observable, it has to be expressed as a linear combination of the moments C^m_l, meaning that it has to be expanded in spherical harmonics. By making use of their orthogonality relation, one can then express observables of the form,

$$\tau\langle(p^\tau)^2\mathcal{O}\rangle = \int \frac{\mathrm{d}^2 p_\perp}{(2\pi)^2}\int \frac{\mathrm{d}p_\eta}{2\pi} p^\tau \mathcal{O}(\theta_p,\phi_p) f, \tag{106}$$

as a linear combination of the coefficients,

$$\tau\langle(p^\tau)^2\mathcal{O}\rangle = \sum_{(l,m)}\alpha^{\mathcal{O}}_{m,l}C^m_l, \tag{107}$$

where the expansion coefficients $\alpha^{\mathcal{O}}_{m,l}$ are determined as

$$\alpha^{\mathcal{O}}_{m,l} = \int \mathrm{d}\Omega_p \mathcal{O}(\theta_p,\phi_p) Y^{m*}_l(\theta_p,\phi_p). \tag{108}$$

Specifically, for calculating the observables $dE_\perp/dy$ and v^E_n that are of interest to us, we need to consider integrals of expressions of the form,

$$\mathcal{O}_n(\theta_p,\phi_p) = e^{in\phi_p}\sin(\theta_p). \tag{109}$$

Since the ϕ_p-dependence of Y^{m*}_l is simply given by $e^{-im\phi_p}$, it is already obvious that $\alpha^{\mathcal{O}_n}_{m,l}$ vanishes for all $m \neq n$. Additionally, for increasing l, the spherical harmonics Y^{n*}_l alternate between being symmetric and antisymmetric with respect to θ_p, such that $\alpha^{\mathcal{O}_n}_{n,l} = 0$ for $l-n$ odd, while for $l-n$ even, the coefficients can be computed as

$$\alpha_{n,l}^{\mathcal{O}_n} = 2\pi 2^{-l} y_l^n \sum_{k=0}^{\frac{l-n}{2}} (-1)^{k+n} \binom{l}{n} \binom{2l-2k}{l} \times \frac{(l-2k)!}{(l-2k-n)!} \frac{\Gamma(\frac{n+3}{2})\Gamma(\frac{l-2k-n+1}{2})}{\Gamma(\frac{l-2k+4}{2})}. \quad (110)$$

In the special case $n = 1$, only one coefficient is nonvanishing, but otherwise, there are infinitely many. However, their values are decreasing with l quickly enough so that cutting off the expansion at $l_{\max}$ yields a reasonable approximation.

B. Relativistic lattice Boltzmann solver

Within our second approach, we employ a RLB solver inspired by the finite difference RLB algorithm discussed in Refs. [75–79]. The strategy for devising the numerical method is split into three main parts, which are described in this subsection. The structure of the kinetic equation is presented in Sec. IV B 1 in two forms. The first form is based on the standard Bjorken coordinates $(\tau, \mathbf{x}_\perp, \eta)$, while the second relies on a set of hybrid free-streaming coordinates, inspired by the approach in Ref. [52]. The momentum space discretization is discussed in Sec. IV B 2. The spatial and temporal discretization, as well as the numerical schemes employed for the advection and time stepping, are briefly summarized in Sec. IV B 3.

1. Boltzmann equation for the RLB approach

In the RLB method, we employ the factorization of the momentum space with respect to the coordinates (p, v_z, ϕ_p) introduced in Eq. (19). Starting from Eq. (20), we apply the LB algorithm at the level of the function $\mathcal{F}_{\rm RLB} = \frac{\tau_0}{\tau}\mathcal{F}$, where $\mathcal{F}$ is introduced in Eq. (21). Specifically,

$$\mathcal{F}_{\rm RLB} = \frac{\pi \nu_{\rm eff} R^2 \tau_0}{(2\pi)^3} \left(\frac{{\rm d}E_\perp^{(0)}}{{\rm d}\eta}\right)^{-1} \int_0^\infty {\rm d}p^\tau (p^\tau)^3 f. \quad (111)$$

The nondimensionalization of the coordinates τ and $\mathbf{x}_\perp$ is performed with respect to $R^{3/4}\tau_0^{1/4}$ [80]; i.e.,

$$\bar{\tau} = \frac{\tau}{\tau_0^{1/4} R^{3/4}} = \left(\frac{R}{\tau_0}\right)^{1/4} \tilde{\tau},$$
$$\bar{\mathbf{x}}_\perp = \frac{\mathbf{x}_\perp}{\tau_0^{1/4} R^{3/4}} = \left(\frac{R}{\tau_0}\right)^{1/4} \tilde{\mathbf{x}_\perp}, \quad (112)$$

while the energy density and temperature are nondimensionalized with respect to constant quantities,

$$\bar{\epsilon} = \frac{\tau_0 \pi R^2 \epsilon}{dE_\perp^{(0)}/d\eta} = \frac{\tau_0}{\tau}\tilde{\epsilon},$$
$$\bar{T} = \left(\frac{\tau_0 \pi R^2 \frac{\pi^2}{30}\nu_{\rm eff}}{dE_\perp^{(0)}/d\eta}\right)^{1/4} T = \left(\frac{\tau_0}{\tau}\right)^{1/4} \tilde{T}, \quad (113)$$

such that $\bar{\epsilon} = \bar{T}^4$. In this section, we use an overhead bar $\bar{}$ to denote dimensionless quantities obtained using the above convention, in contrast to the overhead tilde $\tilde{}$ employed in Sec. II (note that $\bar{T}$ and $\bar{\epsilon}$ are related to T and ϵ through constant factors). The Boltzmann equation (20) written for $\mathcal{F}_{\rm RLB}$ introduced above reads [80]

$$\left(\frac{\partial}{\partial\bar{\tau}} + \mathbf{v}_\perp \cdot \bar{\nabla} + \frac{1+v_z^2}{\tau}\right)\mathcal{F}_{\rm RLB} - \frac{1}{\bar{\tau}}\frac{\partial[v_z(1-v_z^2)\mathcal{F}_{\rm RLB}]}{\partial v_z} = -\hat{\gamma}(v^\mu u_\mu)\bar{T}(\mathcal{F}_{\rm RLB} - \mathcal{F}_{\rm RLB}^{\rm eq}). \quad (114)$$

The components of the stress-energy tensor can be nondimensionalized in the same way as the energy density, being related to $\mathcal{F}_{\rm RLB}$ through

$$\bar{T}^{\mu\nu} = \int d\Omega_p v^\mu v^\nu \mathcal{F}_{\rm RLB}. \quad (115)$$

The energy-weighted flow harmonics (36) can be obtained via

$$v_n^E = \frac{\int_{\mathbf{x}_\perp}\int d\Omega_p \sqrt{1-v_z^2} e^{in\phi_p}\mathcal{F}_{\rm RLB}}{\int_{\mathbf{x}_\perp}\int d\Omega_p \sqrt{1-v_z^2}\mathcal{F}_{\rm RLB}}. \quad (116)$$

The Boltzmann equation in the form given in Eq. (114) serves as the basis of the algorithm employed for large values of the opacity $\hat{\gamma}$. At small values of the opacity, we find the form in Eq. (114) unsuitable and instead employ free-streaming coordinates in momentum space. This approach is inspired from Ref. [80] but differs from the aforementioned approach because the spatial coordinates are left unchanged. Defining

$$p_{\rm fs}^\tau = p^\tau \Delta, \qquad v_z^{\rm fs} = \frac{\tau v_z}{\tau_0 \Delta},$$
$$p^\tau = p_{\rm fs}^\tau \Delta_{\rm fs}, \qquad v_z = \frac{\tau_0 v_z^{\rm fs}}{\tau \Delta_{\rm fs}}, \quad (117)$$

where

$$\Delta = \sqrt{1 + \left(\frac{\tau^2}{\tau_0^2} - 1\right) v_z^2},$$
$$\Delta_{\rm fs} = \frac{1}{\Delta} = \sqrt{1 - \left(1 - \frac{\tau_0^2}{\tau^2}\right) v_{z;{\rm fs}}^2}, \quad (118)$$

the Boltzmann equation (20) becomes

$$\frac{\partial f}{\partial \bar{\tau}}+\frac{1}{\Delta_{\rm fs}}\mathbf{v}_{\perp;\rm fs}\cdot\bar{\nabla}_\perp f=-\hat{\gamma}(v^\mu u_\mu)\bar{T}(f-f_{\rm eq}), \tag{119}$$

where $\mathbf{v}_{\perp;\rm fs}=\sqrt{1-v_{z;\rm fs}^2}(\cos\phi_p,\sin\phi_p)$, while $v_\mu u^\mu = u^\tau-\frac{1}{\Delta_{\rm fs}}\mathbf{v}_{\perp;\rm fs}\cdot\mathbf{u}_\perp$. We now introduce the function $\mathcal{F}_{\rm fs}$, defined in analogy to Eq. (111) using integration with respect to $p^\tau_{\rm fs}$:

$$\mathcal{F}_{\rm fs}=\frac{\pi\nu_{\rm eff}R^2\tau_0}{(2\pi)^3}\left(\frac{{\rm d}E_\perp^{(0)}}{{\rm d}\eta}\right)^{-1}\int_0^\infty {\rm d}p^\tau_{\rm fs}(p^\tau_{\rm fs})^3 f, \tag{120}$$

such that Eq. (119) becomes

$$\frac{\partial \mathcal{F}_{\rm fs}}{\partial \bar{\tau}}+\frac{1}{\Delta_{\rm fs}}\mathbf{v}_{\perp;\rm fs}\cdot\bar{\nabla}_\perp \mathcal{F}_{\rm fs}=-\hat{\gamma}(v^\mu u_\mu)\bar{T}(\mathcal{F}_{\rm fs}-\mathcal{F}^{\rm eq}_{\rm fs}). \tag{121}$$

Due to the changes to the momentum space degrees of freedom, the computation of the components of the stress-energy tensor becomes more involved. Taking into account the transformation of the measure $dp^\tau(p^\tau)^2d\Omega_p = (\tau_0/\tau)dp^\tau_{\rm fs}(p^\tau_{\rm fs})^2d\Omega_{p;\rm fs}$, the dimensionless components $\bar{T}^{\mu\nu}$ can be computed as

$$\begin{aligned}
\bar{T}^{\tau\tau}&=\frac{\tau_0}{\tau}\int d\Omega_{p;\rm fs}\Delta_{\rm fs}\mathcal{F}_{\rm fs},\\
\bar{T}^{\tau i}&=\frac{\tau_0}{\tau}\int d\Omega_{p;\rm fs}v^i_{\perp;\rm fs}\mathcal{F}_{\rm fs},\\
\bar{T}^{ij}&=\frac{\tau_0}{\tau}\int d\Omega_{p;\rm fs}\frac{v^i_{\perp;\rm fs}v^j_{\perp;\rm fs}}{\Delta_{\rm fs}}\mathcal{F}_{\rm fs},\\
\tau^2\bar{T}^{\eta\eta}&=\frac{\tau_0^3}{\tau^3}\int d\Omega_{p;\rm fs}\frac{v^2_{z;\rm fs}}{\Delta_{\rm fs}}\mathcal{F}_{\rm fs},
\end{aligned} \tag{122}$$

where $v^i_{\perp;\rm fs}=v_{\perp;\rm fs}(\cos\phi_p,\sin\phi_p)$ and $v_{\perp;\rm fs}=\sqrt{1-v^2_{z;\rm fs}}$. Based on the equilibrium Bose-Einstein distribution at vanishing chemical potential,

$$f_{\rm eq}=(e^{p_\mu u^\mu/T}-1)^{-1}, \tag{123}$$

the functions $\mathcal{F}^{\rm eq}_{\rm RLB}$ and $\mathcal{F}^{\rm eq}_{\rm fs}$ in Eq. (111), are readily obtained as

$$\begin{aligned}
\mathcal{F}^{\rm eq}_{\rm RLB}&=\frac{1}{4\pi}\frac{\bar{\epsilon}}{(u^0-\mathbf{v}_\perp\cdot\boldsymbol{u}_\perp)^4},\\
\mathcal{F}^{\rm eq}_{\rm fs}&=\frac{1}{4\pi}\frac{\bar{\epsilon}}{(u^0\Delta_{\rm fs}-\boldsymbol{v}_{\perp;\rm fs}\cdot\boldsymbol{u}_\perp)^4},
\end{aligned} \tag{124}$$

where $\bar{\epsilon}=\bar{T}^4$.

The system is initialized using the Romatschke-Strickland distribution [81] for Bose-Einstein statistics [82],

$$f_{\rm RS}=\left\{\exp\left[\frac{1}{\Lambda}\sqrt{(p\cdot u)^2+\xi_0(p\cdot\hat{\eta})^2}\right]-1\right\}^{-1}, \tag{125}$$

where $\hat{\eta}^\mu$ is the unit vector along the rapidity coordinate. Simplifying to the initial state considered in this paper, Eq. (125) reduces to

$$f_{\rm RS}=\left[\exp\left(\frac{p^\tau}{\Lambda}\sqrt{1+\xi_0 v_z^2}\right)-1\right]^{-1}. \tag{126}$$

The function $\Lambda\equiv\Lambda(\mathbf{x}_\perp)$ is determined from

$$\Lambda^4(\mathbf{x}_\perp)=2T^4(\tau_0,\mathbf{x}_\perp)\left(\frac{\arctan\sqrt{\xi_0}}{\sqrt{\xi_0}}+\frac{1}{1+\xi_0}\right)^{-1}, \tag{127}$$

where $T(\tau_0,\mathbf{x}_\perp)$ is obtained from the initial energy density $\epsilon(\tau_0,\mathbf{x}_\perp)$ via the equation $\epsilon=aT^4$, where $a=\frac{\pi^2\nu_{\rm eff}}{30}$ for Bose-Einstein statistics. The anisotropy parameter ξ_0 can be used to set the ratio of longitudinal and transverse pressures $\mathcal{P}_{L;0}/\mathcal{P}_{T;0}$ via

$$\frac{\mathcal{P}_{L;0}}{\mathcal{P}_{T;0}}=\frac{2}{1+\xi_0}\frac{(1+\xi_0)\frac{\arctan\sqrt{\xi_0}}{\sqrt{\xi_0}}-1}{1+(\xi_0-1)\frac{\arctan\sqrt{\xi_0}}{\sqrt{\xi_0}}}. \tag{128}$$

The case $\mathcal{P}_{L;0}/\mathcal{P}_{T;0}=0$ implied by the initial conditions in Eq. (11) can be reached only as the limit $\xi_0\to\infty$. In this paper, we consider finite (large) values of ξ_0 and, for simplicity, we employ the same value of ξ_0 throughout the whole transverse plane. Since at initial time $\tau=\tau_0$, $p^\tau_{\rm fs}=p^\tau$ and $v_{z;\rm fs}=v_z$, it can be seen that the initial conditions $\mathcal{F}^{\rm RS}_{\rm RLB}$ and $\mathcal{F}^{\rm RS}_{\rm fs}$ are equal and given by

$$\mathcal{F}^{\rm RS}_{\rm RLB}=\mathcal{F}^{\rm RS}_{\rm fs}=\frac{\bar{\epsilon}/2\pi}{(1+\xi_0v_z^2)^2}\left(\frac{\arctan\sqrt{\xi_0}}{\sqrt{\xi_0}}+\frac{1}{1+\xi_0}\right)^{-1}. \tag{129}$$

2. Momentum space discretization

In this paper, we employ the discretization of the momentum space discussed in Ref. [76]. In this scheme, we employ $Q_{\phi_p}\times Q_z$ discrete values for ϕ_p and v_z ($v_{z;\rm fs}$ in the case of the free streaming variables), such that (ϕ_p,v_z) or $(\phi_p,v_{z;\rm fs})$ are replaced by $(\phi_{p;i},v_{z;j})$ and $(\phi_{p;i},v^{\rm fs}_{z;j})$, respectively. The discrete set of distributions $\mathcal{F}^*_{ij}$ (with $*\in\{\rm RLB,fs\}$) are related to the original distribution function $\mathcal{F}_*$, via [76]

$$\begin{pmatrix}\mathcal{F}^{\rm RLB}_{ij}\\ \mathcal{F}^{\rm fs}_{ij}\end{pmatrix}=\frac{2\pi}{Q_{\phi_p}}w_j\begin{pmatrix}\mathcal{F}_{\rm RLB}(\phi_{p;i},v_{z;j})\\ \mathcal{F}_{\rm fs}(\phi_{p;i},v^{\rm fs}_{z;j}).\end{pmatrix}. \tag{130}$$

The weight $2\pi/Q_{\phi_p}$ is computed in both RLB and fs cases following the prescription of the Mysovskikh

(trigonometric) [83] quadrature, by which the trigonometric circle is discretized equidistantly, $\phi_{p;j} = \phi_0 + \frac{2\pi}{Q_{\phi_p}}(j - \frac{1}{2})$, with $1 \le j \le Q_{\phi_p}$. For definiteness, we set the arbitrary offset ϕ_0 to 0. For the discretization of v_z (RLB) and $v_{z;\mathrm{fs}}$ (FS), we employ two different strategies as discussed below.

RLB case. In the case of large values of $\hat{\gamma}$, when Eq. (114) is considered, we employ the Gauss-Legendre quadrature, such that w_j represent the Gauss-Legendre weights and $v_{z;j}$ are the roots of the Legendre polynomial of order Q_z; i.e., $P_{Q_z}(v_{z;j}) = 0$. Their values up to quadrature orders $Q_z = 1000$ can be found in the supplementary material of Ref. [76]. In this approach, the term $\partial[v_z(1-v_z^2)\mathcal{F}_{\mathrm{RLB}}]/\partial v_z$ is computed by projection onto the space of Legendre polynomials,

$$\left[\frac{\partial[v_z(1-v_z^2)\mathcal{F}_{\mathrm{RLB}}]}{\partial v_z}\right]_{ji} = \sum_{j'=1}^{Q_z} \mathcal{K}^P_{j,j'}\mathcal{F}^{\mathrm{RLB}}_{j'i}. \tag{131}$$

The matrix elements $\mathcal{K}^P_{j,j'}$, given in Eq. (3.54) of Ref. [76], are

$$\begin{aligned}\mathcal{K}^P_{j,j'} = w_j \sum_{m=1}^{Q_z-3} \frac{m(m+1)(m+2)}{2(2m+3)} P_m(v_{z;j})P_{m+2}(v_{z;j'}) \\ - w_j \sum_{m=1}^{Q_z-1} \frac{m(m+1)}{2} P_m(v_{z;j}) \left[\frac{(2m+1)P_m(v_{z;j'})}{(2m-1)(2m+3)}\right. \\ \left. + \frac{m-1}{2m-1} P_{m-2}(v_{z;j'})\right].\end{aligned} \tag{132}$$

The components of the stress-energy tensor are obtained by replacing the integration with respect to $\mathrm{d}\Omega_p$ with a double sum over i and j:

$$\bar{T}^{\mu\nu} = \sum_{i=1}^{Q_{\phi_p}} \sum_{j=1}^{Q_z} \mathcal{F}^{\mathrm{RLB}}_{ij} v^\mu_{ij} v^\nu_{ij}, \tag{133}$$

where $v^\tau_{ij} = 1$, $(v^1_{ij}, v^2_{ij}) = \sqrt{1-v^2_{z;j}}(\cos\phi_{p;i}, \sin\phi_{p;i})$, and $v^\eta_{ij} = \tau^{-1} v_{z;j}$. A similar prescription is employed for the computation of the $\mathrm{d}\Omega_p$ integral in the energy-weighted flow harmonics v^E_n (116).

FS case. For small values of $\hat{\gamma}$, the free-streaming coordinate $v_{z;\mathrm{fs}}$ is discretized in a logarithmic scale. Inspired from Eq. (A61) of Ref. [52], we first perform the change of coordinate to

$$v_{z;\mathrm{fs}} = \frac{1}{A}\tanh\chi, \tag{134}$$

where $0 < A < 1$ and χ takes values between $\pm\mathrm{artanh}A$. In order to increase the accuracy of the momentum space integration, we consider the rectangle method and take the discrete values χ_j at the center of the Q_z equidistant intervals, such that

$$\chi_j = \left(\frac{2j-1}{Q_z} - 1\right)\mathrm{artanh}A, \qquad v^{\mathrm{fs}}_{z;j} = \frac{1}{A}\tanh\chi_j. \tag{135}$$

The quadrature weights w_j are then computed based on the Jacobian due to the change of integration variable from $v_{z;\mathrm{fs}}$ to χ,

$$w_j = \frac{2\mathrm{artanh}A}{AQ_z\cosh^2\chi_j}. \tag{136}$$

Since the discretization of $v_{z;\mathrm{fs}}$ presented above is no longer given by a Gauss quadrature prescription, we note that the FS approach gives rise to a numerical scheme, which is more similar to the discrete velocity method (DVM) approach [84,85]. As before, the components of the stress-energy tensor can be obtained by replacing the integral with respect to $\mathrm{d}\Omega_p$ in Eq. (122) with quadrature sums:

$$\begin{aligned}\bar{T}^{\tau\tau} &= \frac{\tau_0}{\tau}\sum_{i,j}\Delta^{\mathrm{fs}}_j\mathcal{F}^{\mathrm{fs}}_{ij}, \\ \begin{pmatrix}\bar{T}^{\tau 1}\\ \bar{T}^{\tau 2}\end{pmatrix} &= \frac{\tau_0}{\tau}\sum_{i,j} v^{\mathrm{fs}}_{\perp;j}\begin{pmatrix}\cos\phi_{p;i}\\ \sin\phi_{p;i}\end{pmatrix}\mathcal{F}^{\mathrm{fs}}_{ij}, \\ \begin{pmatrix}\bar{T}^{11}\\ \bar{T}^{12}\\ \bar{T}^{22}\end{pmatrix} &= \frac{\tau_0}{\tau}\sum_{i,j}\frac{(v^{\mathrm{fs}}_{\perp;j})^2}{\Delta^{\mathrm{fs}}_j}\begin{pmatrix}\cos^2\phi_{p,i}\\ \sin\phi_{p,i}\cos\phi_{p,i}\\ \sin^2\phi_{p,i}\end{pmatrix}\mathcal{F}^{\mathrm{fs}}_{ij}, \\ \tau^2\bar{T}^{\eta\eta} &= \frac{\tau_0^3}{\tau^3}\sum_{i,j}\frac{(v^{\mathrm{fs}}_{z;j})^2}{\Delta^{\mathrm{fs}}_j}\mathcal{F}^{\mathrm{fs}}_{ij},\end{aligned} \tag{137}$$

where $\Delta^{\mathrm{fs}}_j = [1-(1-\tau_0^2/\tau^2)(v^{\mathrm{fs}}_{z;j})^2]^{1/2}$ and $v^{\mathrm{fs}}_{\perp;j} = \sqrt{1-(v^{\mathrm{fs}}_{z;j})^2}$. A similar procedure is employed for the computation of v^E_n (116).

3. Finite difference schemes

In order to obtain the numerical solution of Eqs. (114) and (121), we consider a discretization of the temporal variable using an adaptive time step $\delta\tau_n = \min(\tau_n/10, \tau_R/2u^\tau, \delta\tau)$, where $\delta\tau = 0.005R$, such that $\tau_{n+1} = \tau_n + \delta\tau_n$. Writing the Boltzmann equation as

$$\frac{\partial\mathcal{F}}{\partial\tau} = L[\mathcal{F}], \tag{138}$$

where $L[\mathcal{F}]$ can be found from Eqs. (114) or (121), we employ the third order total variation diminishing (TVD) Runge-Kutta method proposed in Ref. [86,87]. This algorithm allows the values $\mathcal{F}_{n+1}$ of the distribution functions at

the new time step to be obtained from the old ones using two intermediate stages.

The advection along the transverse directions is performed using the flux-based upwind-biased fifth order weighted essentially nonoscillatory (WENO-5) scheme [63,88]. Considering that the spatial domain of extent $L_1 \times L_2$ is discretized using $N_1 \times N_2$ equidistant nodes, the coordinates of the discrete points are

$$x_{1,s} = x_{1,\mathrm{left}} + \frac{L_1}{N_1}\left(s - \frac{1}{2}\right),$$
$$x_{2,r} = x_{2,\mathrm{bot}} + \frac{L_2}{N_2}\left(r - \frac{1}{2}\right), \tag{139}$$

with $1 \le s \le N_1$ and $1 \le r \le N_2$. Focusing without loss of generality on the derivative with respect to x_1, the algorithm entails

$$c_1\left(\frac{\partial \mathcal{F}}{\partial x_1}\right)_{s,r} = \frac{\mathbb{F}_{s+\frac{1}{2},r} - \mathbb{F}_{s-\frac{1}{2},r}}{\delta x_1}, \tag{140}$$

where $\delta x_1 = L_1/N_1$. The velocity c_1 is given in the case when $\hat{\gamma}$ is large, when Eq. (114) is solved, by $c_1 = \sqrt{1 - v_z^2}\cos\phi_p$ being independent of position and space. In the case of small values of $\hat{\gamma}$, Eq. (121) shows that the advection velocity $c_1 = \frac{1}{\Delta}\sqrt{1 - \tilde{v}_z^2}\cos\phi_p$ depends on the Bjorken time τ; however, it remains constant throughout the entire transverse plane. The stencils required to compute the fluxes $\mathbb{F}_{s\pm\frac{1}{2},r}$ are chosen in an upwind-biased manner based on the sign of c_1. Since the algorithm to compute these stencils is rather lengthy, we do not repeat it here and instead refer the interested reader to Refs. [63,76,88,89] for details.

V. RESULTS

We will now analyze the space-time evolution of the system and the development of transverse flow as a function of the opacity parameter $\hat{\gamma}$ [cf. Eq. (31)]. We focus on the range of opacities $0.01 \le \hat{\gamma} \le 400$ and consider different initial eccentricities $\epsilon_n \in \{0.01, 0.05, 0.1, 0.2, 0.32, 0.36\}$ [cf. Eqs. (14), (15)].

If not stated otherwise, open symbols and dashed lines correspond to results obtained using the expansion in spherical harmonic moments in Sec. IV A, where we typically use $l_{\max} = 32, N_S = 256$, $a_S = 0.0625R$.[8] Conversely, results obtained with the RLB method are represented by solid symbols and solid lines. The RLB simulations are divided in two batches. The first batch includes systems with $\hat{\gamma} \ge 2$. For these simulations, we used the RLB algorithm for large $\hat{\gamma}$ described in Sec. IV B with $Q_z = 40$ and $Q_{\phi_p} = 80$, while the number of nodes on each semiaxis is taken to be $X = 100$ for $\epsilon_n \ge 0.05$ and $X = 200$ for $\epsilon_n < 0.05$. The anisotropy parameter in the initial state is set to $\xi_0 = 20$, corresponding to an initial ratio $\mathcal{P}_L/\mathcal{P}_T \simeq 0.08$. The second batch comprises the systems with $\hat{\gamma} \le 2$ for which we employ the hybrid free-streaming algorithm described in Sec. IV B with $Q_z = 500$ and $Q_{\phi_p} = 80$. In this case, the anisotropy parameter is set to $\xi_0 = 100$, corresponding to $\mathcal{P}_L/\mathcal{P}_T \simeq 0.02$, and the spatial resolution is $X = 100$ nodes per semiaxis.

A. Cooling due to longitudinal expansion ($dE_\perp/d\eta$)

Before we discuss the development of transverse flow, we first investigate the cooling of the system due to work performed against the longitudinal expansion, which is quantified by the decrease of the transverse energy per rapidity $\mathrm{d}E_\perp/\mathrm{d}\eta$. We first note that for a free-streaming system, $\mathrm{d}E_\perp/\mathrm{d}\eta$ is constant. Increasing the opacity will initially only have a small effect, which can be quantified in terms of the linear decrease in $\hat{\gamma}$ calculated in Sec. III E. However, for large opacities $\hat{\gamma} \gg 1$, the system has sufficient time to undergo pressure isotropization at early times, leading to an extended phase of longitudinal cooling, which results in a significant decrease of $\mathrm{d}E_\perp/\mathrm{d}\eta$. Hence, when presenting our results for $\mathrm{d}E_\perp/\mathrm{d}y(\tau)$ in Fig. 1, we have grouped them into two plots for large opacities in the upper panel and small opacities in the lower panel. While for large opacities, the curves are normalized by the initial value $\mathrm{d}E_\perp^{(0)}/\mathrm{d}\eta$ and plotted on a doubly logarithmic scale to visualize the power law decay of $\mathrm{d}E_\perp/\mathrm{d}\eta$ at intermediate times, for small opacities, we show the difference of $\mathrm{d}E_\perp/\mathrm{d}\eta - \mathrm{d}E_\perp^{(0)}/\mathrm{d}\eta$, normalized by the initial value and $\hat{\gamma}$ to account for the linear behaviour in opacity. We also show a comparison with the analytical result from Sec. III E, which provides a good description of the curves for $\hat{\gamma} \lesssim 1$.

Qualitatively, all curves exhibit a similar behavior starting out from the early time fixed point of kinetic theory, where longitudinal pressure vanishes, and energy per rapidity stays almost constant. Subsequently, as longitudinal pressure develops due to interactions, work is being performed, which starts to happen earlier and earlier the larger the opacity. Eventually, at late times $\tau/R \gtrsim 1$, the transverse expansion becomes dominant, and the system rapidly dilutes towards free streaming behaviour, resulting in a late time plateau of the $\mathrm{d}E_\perp/\mathrm{d}\eta(\tau)$-curves.

We find that for large opacities $\hat{\gamma} \gtrsim 10$, the pressure isotropization at early times and the onset of the transverse expansion at later times are sufficiently well separated to observe an intermediate $\tau^{1/3}$-scaling of $dE_\perp/d\eta$, which—as we will see shortly—can be related to the usual $\epsilon \sim \tau^{-4/3}$ decrease of the energy density in Bjorken flow. It stands to reason that, at early times, the transverse gradients in the system are negligible compared to the longitudinal expansion, and the system will locally behave like a

[8] We note that results for $\hat{\gamma} \le 1$ require a larger accuracy, and we use $l_{\max} = 48, N_S = 320$, $a_S = 0.05R$. Similarly, for accurate calculations of $\mathrm{d}E_\perp/\mathrm{d}y$, we need a larger value of $l_{\max}$, and we employ $l_{\max} = 96, N_S = 160$, $a_S = 0.06R$ in this case.

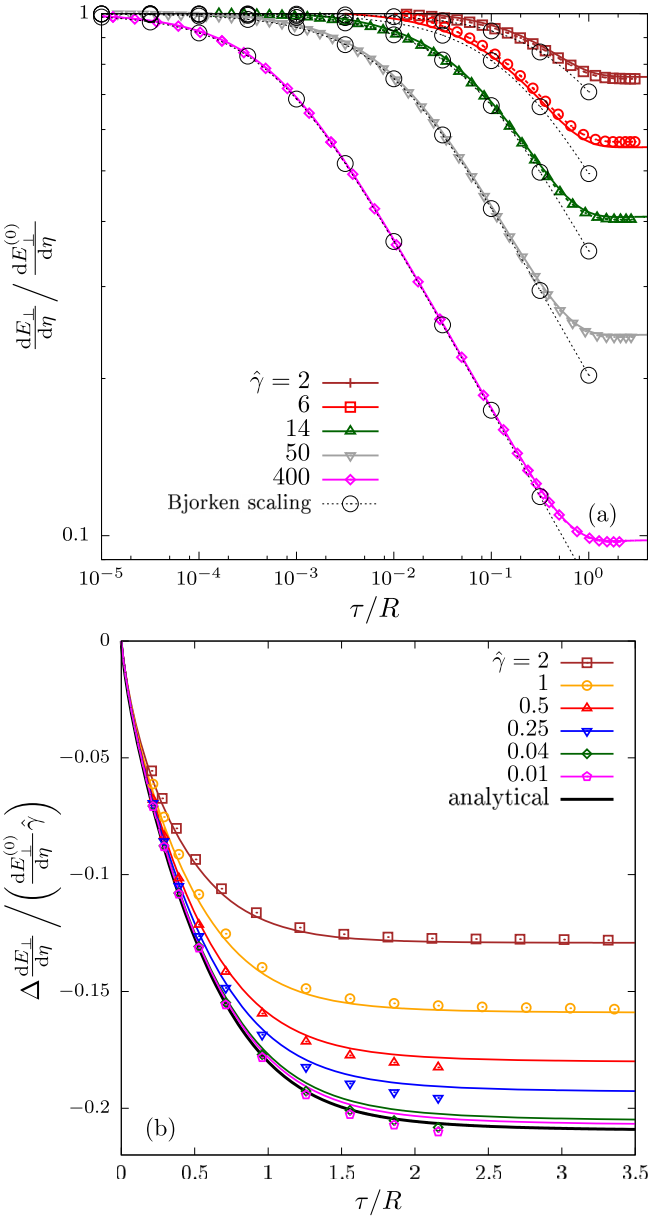

FIG. 1. Evolution of $dE_\perp/d\eta$ (top) and $\Delta dE_\perp/d\eta = dE_\perp/d\eta - dE_\perp^{(0)}/d\eta$ (bottom) normalized with respect to the initial value $dE_\perp^{(0)}/d\eta$ for various large (top) and small opacities (bottom). In the bottom panel, we also normalize with respect to $\hat{\gamma}$. Colored solid lines were obtained with the RLB method, while open symbols denote results from the moment method. The solid black line shows the first order result in opacity expansion. Dashed black lines with black circles correspond to the Bjorken flow prediction derived in Eq. (151), and the curves in the top panel are presented on double logarithmic scale. All results are obtained for initial eccentricity $\epsilon_2 = 0.05$.

one-dimensional Bjorken system. Based on the following considerations, this behavior can be quantified further and cast into a parameter-free prediction for the evolution of $dE_\perp/d\eta$ in Eq. (151), which is indicated by black circles in the upper panel of Fig. 1 and agrees remarkably well with numerical results for the large opacities up to times $\tau/R \lesssim 0.1$.

Defining the conformal scaling variable $\tilde{w}(\tau, \mathbf{x}_\perp) = \frac{T(\tau,\mathbf{x}_\perp)\tau}{4\pi\eta/s}$, the Bjorken flow exhibits a universal attractor curve [90] for

$$\epsilon(\tau)\tau^{4/3} = (4\pi\eta/s)^{4/9} a^{1/9} (\epsilon\tau)_0^{8/9} C_\infty \mathcal{E}(\tilde{w}),$$
$$\tau^{1/3}\frac{dE_\perp}{d^2\mathbf{x}_\perp d\eta} = (4\pi\eta/s)^{4/9} a^{1/9} (\epsilon\tau)_0^{8/9} C_\infty f_{E_\perp}(\tilde{w}), \quad (141)$$

where the asymptotic limits of $\mathcal{E}(\tilde{w})$ are known [90] and given by

$$\mathcal{E}(\tilde{w} \gg 1) = 1 - \frac{2}{3\pi\tilde{w}},$$
$$\mathcal{E}(\tilde{w} \ll 1) = C_\infty^{-1}\tilde{w}^{4/9}. \quad (142)$$

Similarly, one finds for $f_{E_\perp}(\tilde{w})$ that

$$f_{E_\perp}(\tilde{w} \gg 1) = \frac{\pi}{4},$$
$$f_{E_\perp}(\tilde{w} \ll 1) = C_\infty^{-1}\tilde{w}^{4/9}, \quad (143)$$

where for the RTA Boltzmann equation, $C_\infty \approx 0.9$ [73,90], and the leading constant $\pi/4$ can be deduced from an integral of the thermal equilibrium distribution. By use of the equation of state $\epsilon = aT^4$, Eq. (141) can be recast as a self-consistency condition for $\tilde{w}$, which takes the form,

$$\tilde{w}(\tau, \mathbf{x}_\perp) = (4\pi\eta/s)^{-8/9} a^{-2/9} (\epsilon\tau)_0^{2/9}(\mathbf{x}_\perp) \times \tau^{2/3}[C_\infty \mathcal{E}(\tilde{w}(\tau, \mathbf{x}_\perp))]^{1/4}, \quad (144)$$

and can be used to relate the differential with respect to $\tilde{w}$ at fixed τ to the differential with respect to the transverse plane coordinates $\mathbf{x}_\perp$ as

$$\frac{d\tilde{w}}{\tilde{w}}\left[1 - \frac{1}{4}\frac{\tilde{w}\mathcal{E}'(\tilde{w})}{\mathcal{E}(\tilde{w})}\right] = \frac{2}{9}\frac{\frac{\partial(\epsilon\tau)_0(\mathbf{x}_\perp)}{\partial|\mathbf{x}_\perp|}}{(\epsilon\tau)_0(\mathbf{x}_\perp)} d|\mathbf{x}_\perp|. \quad (145)$$

Specifically, for the initial Gaussian profile in Eq. (14), one finds

$$|\mathbf{x}_\perp| d|\mathbf{x}_\perp| = -\frac{9R^2}{4}\frac{d\tilde{w}}{\tilde{w}}\left[1 - \frac{1}{4}\frac{\tilde{w}\mathcal{E}'(\tilde{w})}{\mathcal{E}(\tilde{w})}\right], \quad (146)$$

which can be used to calculate the resulting change of the energy per unit rapidity as follows. Starting from the definition in Eq. (141), one can express the energy per unit rapidity in terms of the scaling function,

$$\frac{dE_\perp}{d\eta} = \tau^{-1/3}(4\pi\eta/s)^{4/9} a^{1/9} C_\infty \times (2\pi)\int d|\mathbf{x}_\perp||\mathbf{x}_\perp| f_{E_\perp}(\tilde{w}(\tau, \mathbf{x}_\perp))(\epsilon\tau)_0^{8/9}(\mathbf{x}_\perp). \quad (147)$$

Expressing the remaining factor of the energy density $(\epsilon\tau)_0^{8/9}$ in terms of the conformal scaling variable $\tilde{w}$, according to

$$(\epsilon\tau)_0^{8/9}(\mathbf{x}_\perp) = (4\pi\eta/s)^{32/9} a^{8/9} \tau^{-8/3} \frac{\tilde{w}^4}{C_\infty \mathcal{E}(\tilde{w})}, \quad (148)$$

which follows from Eq. (144), one can then express

$$\frac{dE_\perp}{d\eta} = \frac{9\pi a}{2R}\left(\frac{R}{\tau}\right)^3 (4\pi\eta/s)^4 \times \int_0^{\tilde{w}(\tau,\mathbf{x}_\perp=0)} \frac{\tilde{w}^3 d\tilde{w}}{\mathcal{E}(\tilde{w})}\left[1 - \frac{1}{4}\frac{\tilde{w}\mathcal{E}'(\tilde{w})}{\mathcal{E}(\tilde{w})}\right] f_{E_\perp}(\tilde{w}). \quad (149)$$

By considering the ratio $\frac{dE_\perp}{d\eta} / \frac{dE_\perp^0}{d\eta}$ and identifying

$$\frac{(4\pi\eta/s)^4 a}{dE_\perp^0/d\eta R} = \frac{1}{\pi}\left(\frac{4\pi}{5\hat{\gamma}}\right)^4, \quad (150)$$

one then obtains the final result

$$\frac{dE_\perp/d\eta}{dE_\perp^0/d\eta} = \frac{9}{2}\left(\frac{4\pi}{5\hat{\gamma}}\right)^4 \left(\frac{R}{\tau}\right)^3 \times \int_0^{\tilde{w}(\tau,\mathbf{x}_\perp=0)} \frac{\tilde{w}^3 d\tilde{w}}{\mathcal{E}(\tilde{w})}\left[1 - \frac{\tilde{w}}{4}\frac{\mathcal{E}'(\tilde{w})}{\mathcal{E}(\tilde{w})}\right] f_{E_\perp}(\tilde{w}), \quad (151)$$

where $\tilde{w}(\tau, \mathbf{x}_\perp = 0)$ in the center of the collision can be expressed in terms of $\hat{\gamma}$ via

$$\tilde{w}(\tau, \mathbf{x}_\perp = 0) = \left(\frac{5\hat{\gamma}}{4\pi}\right)^{8/9}\left(\frac{\tau}{R}\right)^{2/3} [C_\infty \mathcal{E}(\tilde{w})]^{1/4}. \quad (152)$$

The asymptotic behavior of Eq. (151) can be understood as follows. In the limit $\hat{\gamma}(\frac{\tau}{R})^{3/4} \ll 1$, we have $\tilde{w} \approx \frac{5}{4\pi}\hat{\gamma}(\frac{\tau}{R})^{3/4} \ll 1$, and we can approximate $\mathcal{E}(\tilde{w}) = f_{E_\perp}(\tilde{w}) = C_\infty^{-1}\tilde{w}^{4/9}$ to obtain

$$\frac{dE_\perp/d\eta}{dE_\perp^0/d\eta} = 1, \quad (153)$$

as expected. Conversely, in the limit $\hat{\gamma}^{3/4}(\frac{\tau}{R}) \gg 1$, we have $\tilde{w} \approx (\frac{5}{4\pi})^{8/9}\hat{\gamma}^{8/9} C_\infty^{1/4}(\frac{\tau}{R})^{2/3} \gg 1$, such that we can approximate $\mathcal{E}(\tilde{w}) \approx 1$ and evaluate Eq. (151) as

$$\frac{dE_\perp/d\eta}{dE_\perp^0/d\eta} = \frac{9}{8}\left(\frac{4\pi}{5\hat{\gamma}}\right)^{4/9}\left(\frac{R}{\tau}\right)^{1/3} C_\infty f_{E_\perp}(\infty), \quad (154)$$

which predicts that $dE_\perp/d\eta$ decreases as $\tau^{-1/3}$ at intermediate times before the transverse expansion becomes dominant. By comparing the results in Fig. 1, one finds that for sufficiently large opacities, the power-law behavior in Eq. (154) is indeed realized at intermediate times and discontinues once $\tau/R \simeq 1$ when the transverse expansion becomes dominant, such that the estimate (154) is no longer applicable, and $\frac{dE_\perp/d\eta}{dE_\perp^0/d\eta}$ attains a constant asymptotic value. The details regarding the computation of the integral in Eq. (151) are presented in Appendix E.

We note that our estimate in Eq. (154) also shows that for sufficiently large opacities, where longitudinal cooling occurs predominantly before the transverse expansion sets in, the final value of $\frac{dE_\perp/d\eta}{dE_\perp^0/d\eta}$ is proportional to $\hat{\gamma}^{-4/9}$, as previously argued in [52]. Numerical results for the asymptotic values of $\frac{\mathrm{d}E_\perp/d\eta}{\mathrm{d}E_\perp^0/d\eta}$, extracted by performing extrapolations of the curves of the form $a + b\tilde{\tau}^{-c}$, where a, b, and c are fitting parameters, are shown in Fig. 2 as a function of the opacity parameter $\hat{\gamma}$. We find that at low $\hat{\gamma}$, the analytical result to leading order in opacity [cf. Eq. (82)], represented with a solid black line, provide an accurate description up to $\hat{\gamma} \lesssim 1$. Conversely, for large opacities $\hat{\gamma}$, the decrease of the energy per unit rapidity $\frac{\mathrm{d}E_\perp/d\eta}{\mathrm{d}E_\perp^0/d\eta}$ exhibits the expected scaling behavior, with $\frac{\mathrm{d}E_\perp/d\eta}{\mathrm{d}E_\perp^0/d\eta} \approx 1.4\hat{\gamma}^{-4/9}$ for $\hat{\gamma} \gtrsim 10$, as indicated by the purple line. By comparing the numerical coefficient with Eq. (154), this result seems to indicate that cooling stops at a time $\tau_{\mathrm{stop}} \simeq 0.6R$, which is consistent with the trend seen for the high $\hat{\gamma}$ curves in Fig. 1(a).

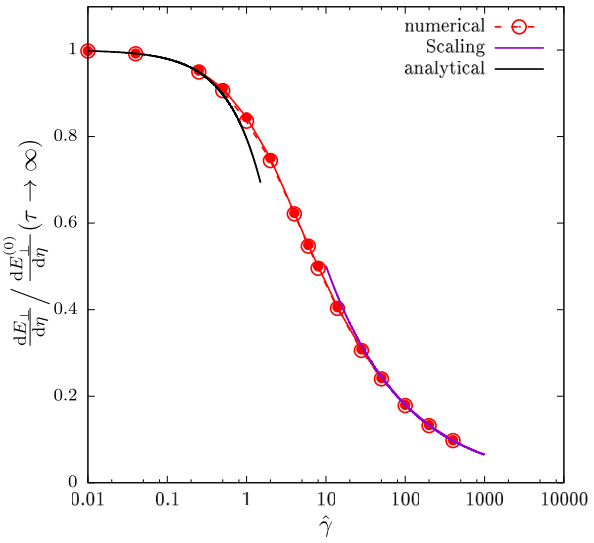

FIG. 2. Opacity ($\hat{\gamma}$) dependence of the ratio of final to initial (transverse) energy per-unit rapidity $\frac{\mathrm{d}E_\perp}{\mathrm{d}\eta} / \frac{\mathrm{d}E_\perp^{(0)}}{\mathrm{d}\eta}$. The red solid line with filled circles denotes results from the RLB method, while the red dotted line with open circles was obtained in the moment method. Numerical results are compared to analytical results obtained in leading order opacity expansion (black solid curve), and a power-law scaling fit $\frac{\mathrm{d}E_\perp}{\mathrm{d}\eta} / \frac{\mathrm{d}E_\perp^{(0)}}{\mathrm{d}\eta} \approx 1.4\hat{\gamma}^{-4/9}$ at large opacities (purple solid line).

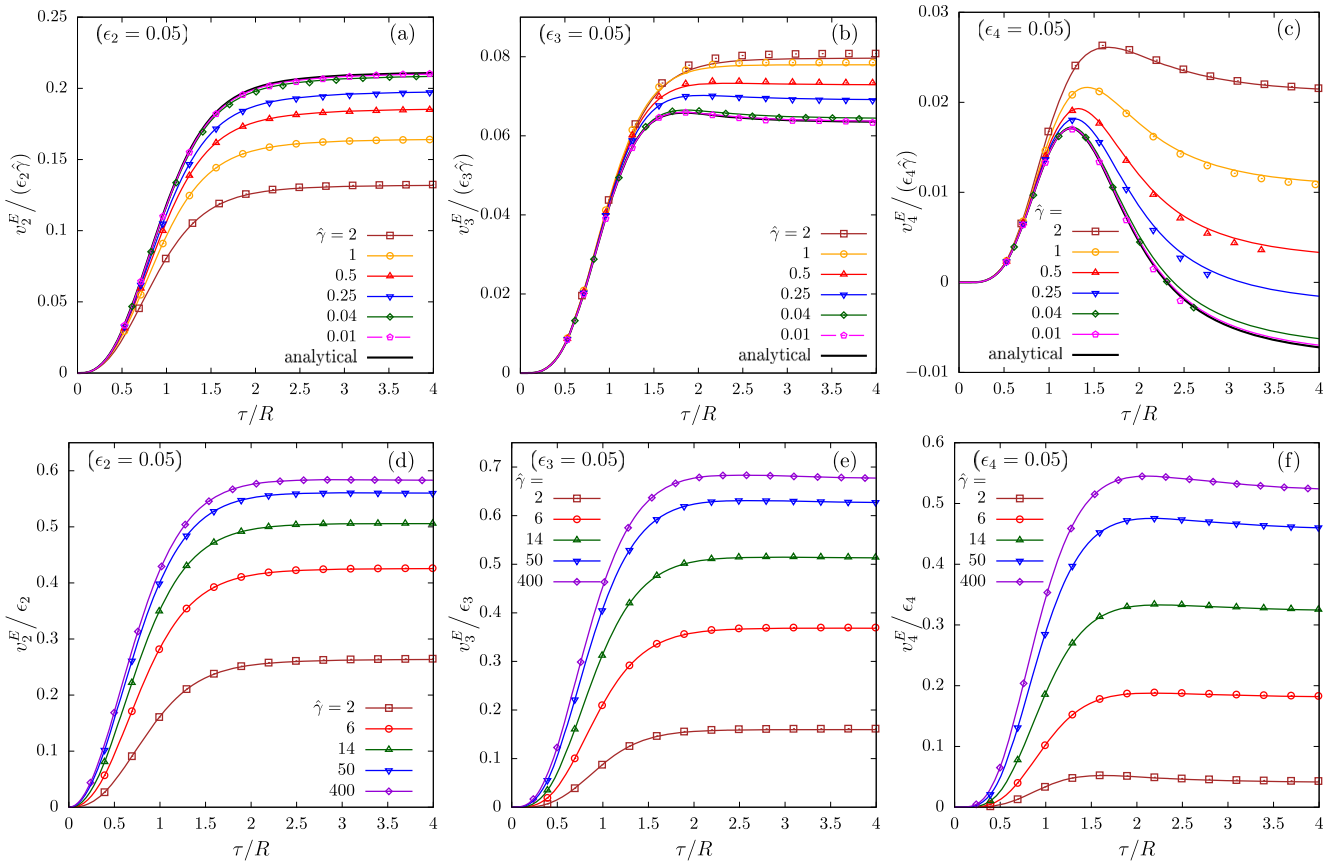

FIG. 3. Evolution of the linear flow response $v_n^E/\epsilon_n\hat{\gamma}$ at small opacities $\hat{\gamma}$ (top) and v_n^E/ϵ_n at large opacities $\hat{\gamma}$ (bottom). Different columns correspond to elliptic flow $n = 2$ (left), triangular flow $n = 3$ (middle), and quadrangular flow $n = 4$ (right). Colored solid lines were obtained in the RLB method, while open symbols denote results from the moments method. Analytical results are plotted as solid black lines. All results were obtained for an initial eccentricity $\epsilon_n = 0.05$.

B. Development and opacity dependence of transverse flow harmonics (v_n)

Next, we will analyze the development of anisotropic flow in terms of the time dependence of the harmonic transverse flow coefficients v_n^E for different opacities. We recall that the initial anisotropies are modeled using a single harmonic (n) perturbation and first look at the time dependence of v_2^E, v_3^E, and v_4^E for different opacities, where in each case, the eccentricities are fixed to $\epsilon_n = 0.05$, which serves as a good approximation to the small eccentricity limit. We measure the magnitude of the linear response ratio v_n/ϵ_n for each harmonic; in addition, we also extract the nonlinear response of the fourth and sixth order harmonics via the ratios v_4/ϵ_2^2, v_6/ϵ_3^2, and v_6/ϵ_2^3. For notational brevity, we omit the superscript E when referring to the energy-weighted flow harmonics, i.e. $v_n \equiv v_n^E$.

Since the qualitative behaviour of v_n is somewhat different in the regimes of small and large opacities $\hat{\gamma}$, we again divide our results into two categories corresponding to $\hat{\gamma} \geq 2$ and $\hat{\gamma} \leq 2$, as in Fig. 1. Since the analytical calculation in Sec. III indicates that at small $\hat{\gamma}$, all response coefficients increase linearly with $\hat{\gamma}$, we will further normalize our low opacity results ($\hat{\gamma} \leq 2$) by division with respect to $\hat{\gamma}$.

Our results are compactly summarized in Figs. 3 and 4, where we present numerical results for the linear $(v_2/\epsilon_2, v_3/\epsilon_3, v_4/\epsilon_4)$ and nonlinear $(v_4/\epsilon_2^2, v_6/\epsilon_3^2, v_6/\epsilon_2^3)$ response coefficients obtained for small (top panels) and large (bottom panels) values of $\hat{\gamma}$. We find that for small values of $\hat{\gamma} \lesssim 0.04$, the leading order linear dependence of v_n/ϵ_n on $\hat{\gamma}$ computed in Eq. (83)–(85) is nicely confirmed by the asymptotic approach of our numerical results to the analytical results, represented by a solid black line. Similarly, a linear dependence with respect to $\hat{\gamma}$ is also found for the nonlinear response coefficients $v_4/\epsilon_2^2, v_6/\epsilon_3^2, v_6/\epsilon_2^3$, which, for v_4/ϵ_2^2, is in line with the result obtained in Ref. [53] for a slightly different initial setup. While for $\hat{\gamma} \gtrsim 0.25$, all linear flow coefficients exhibit a positive response with respect to the initial eccentricities, the quadrangular flow $v_4/\epsilon_4\hat{\gamma}$ in Fig. 3 shows a negative response for $\hat{\gamma} \lesssim 0.25$.

Based on a closer inspection, one finds that the curves of $v_4/(\epsilon_4\hat{\gamma})$ exhibit an early time increase similar to the

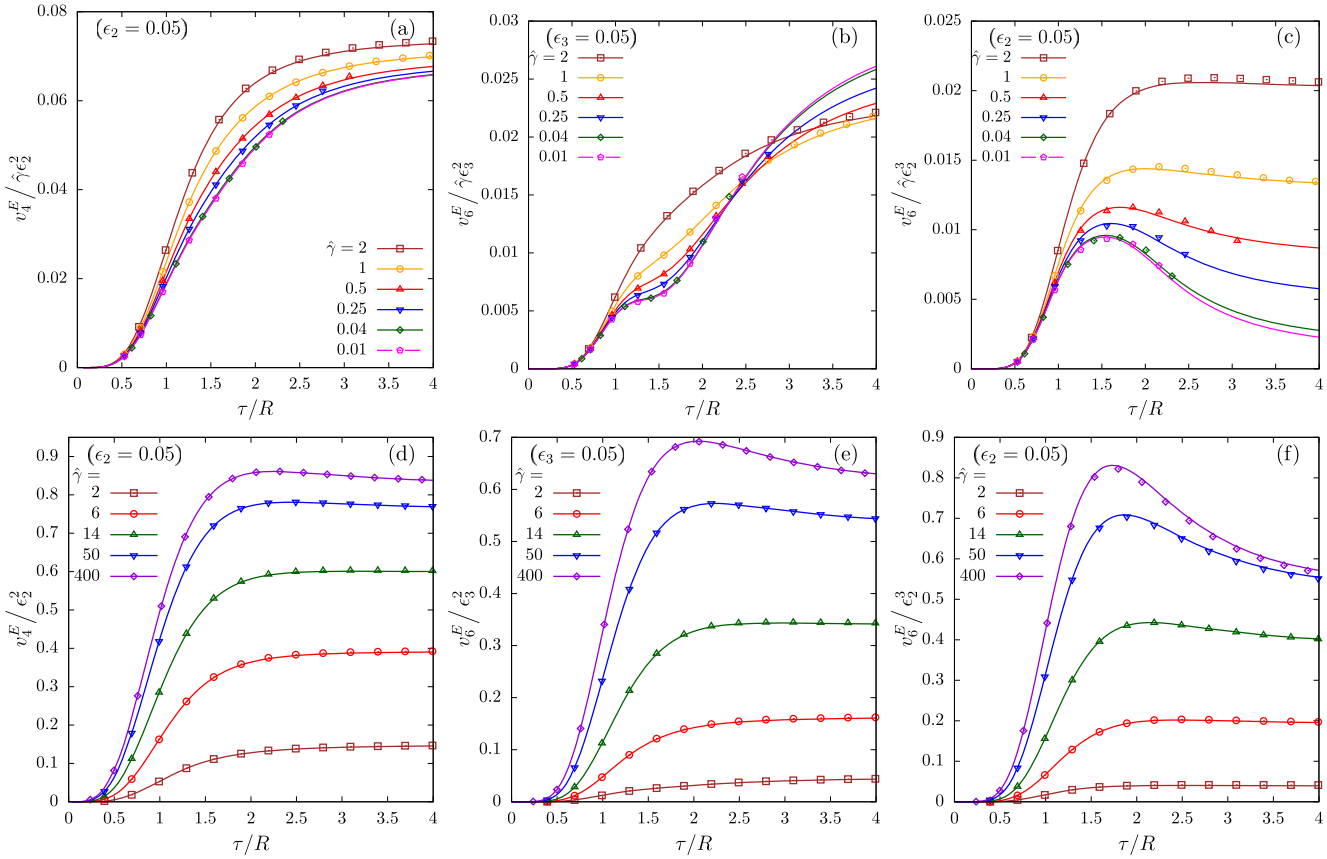

FIG. 4. (Top line) Evolution at low opacities of the nonlinear flow response coefficients $v_4^E/\epsilon_2^2\hat{\gamma}$ (left), $v_6^E/\epsilon_3^2\hat{\gamma}$ (middle), and $v_6^E/\epsilon_2^3\hat{\gamma}$ (right). (Bottom line) Evolution at large opacities of v_4^E/ϵ_2^2, v_6^E/ϵ_3^2 (middle) and v_6^E/ϵ_2^3 (right). Colored solid lines were obtained in the RLB method, while open symbols denote results from the moments method. All results were obtained for an initial eccentricity $\epsilon_n = 0.05$.

behavior seen for the other harmonic flow coefficients; however, in contrast to v_2, v_3, the initial rise of v_4 peaks around $\tau \simeq 1.5R$, followed by a decrease due to negative contributions received at large times. When increasing the opacity, nonlinear effects cause the elliptic flow response $v_2/(\epsilon_2\hat{\gamma})$ to decrease, while $v_3/(\epsilon_3\hat{\gamma})$, $v_4/(\epsilon_4\hat{\gamma})$ as well as the nonlinear $v_4/(\epsilon_2^2\hat{\gamma})$ and $v_2/(\epsilon_2^3\hat{\gamma})$ exhibit an increasing trend; due to the rather complicated time dependence, the behavior of $v_6/(\epsilon_3^2\hat{\gamma})$ appears nonmonotonic. Clearly, the largest effect is seen in the case of the v_4/ϵ_4-response, which changes sign as the late time contributions become less and less prominent.

When considering large opacities $\hat{\gamma} \gtrsim 2$ shown in the bottom panels of Figs. 3 and 4, the curves for linear $(v_2/\epsilon_2, v_3/\epsilon_3, v_4/\epsilon_4)$ and nonlinear $(v_4/\epsilon_2^2, v_6/\epsilon_3^2, v_6/\epsilon_2^3)$ response coefficients retain the same qualitative time dependence and monotonically increase as a function of $\hat{\gamma}$, seemingly approaching a finite large opacity limit, which we will further examine in the following. Generally, we find that the linear anisotropic flow response develops predominantly in the regime $0.5 \lesssim \tau/R \lesssim 2$ and then stays almost constant, with the exception of the aforementioned late time decrease of linear v_4. In the case of the nonlinear coefficients v_4/ϵ_2^2, v_6/ϵ_3^2, and v_6/ϵ_2^3, the response takes a little longer to develop, but nevertheless, the asymptotic late time value is reached on similar timescales $0.5 \lesssim \tau/R \lesssim 4$.

Beyond the time evolution of the different flow harmonics, additional insights into the development of anisotropic flow can be gained from their production rates $p(v_n)$, which correspond to the local rate of change of these quantities. Since free streaming and longitudinal expansion do not change the (transverse) momentum distribution of particles, the buildup of anisotropic flow is solely due to interactions. We can thus determine the production rate $p(O)$ of a flow observable $O = \int d^2x_\perp \int \frac{d^3p}{(2\pi)^3} \mathcal{O} f$ as

$$p(O) = \frac{dO}{dx_\perp d\tau}\bigg|_{\text{coll}} = \int d\phi_{x_\perp} x_\perp \int \frac{d^3p}{(2\pi)^3} \mathcal{O} \frac{d}{d\tau} f\bigg|_{\text{coll}}, \quad (155)$$

where the rate of change of the phase-space distribution f due to collisions is given by

$$\frac{d}{d\tau} f\bigg|_{\text{coll}} = \frac{v^\mu u_\mu}{\tau_R}(f_{\text{eq}} - f). \quad (156)$$

Specifically, the observables v_n^E are defined according to Eq. (36) as quotients of two such terms, such that the production rate $p(O)$ receives two contributions coming from the numerator and denominator according to the quotient rule for differentiation.

Figure 5 features heat maps in the $x_\perp$-τ-plane for $p(v_2)$, $p(v_3)$, and $p(v_4)$ as well as $p(v_{4,n})$ referring to the nonlinear response, normalized by the respective late time asymptotic values of v_n for several different opacities ranging from the analytical results for small opacities $\hat{\gamma} \ll 1$ all the way to $\hat{\gamma} = 50$. Besides the production rates of different v_n, the top panel of Fig. 5, also shows a heat map of the dimensionless temperature $\tilde{T}$ and the flow components u^τ and u^r to allow for a comparison with the

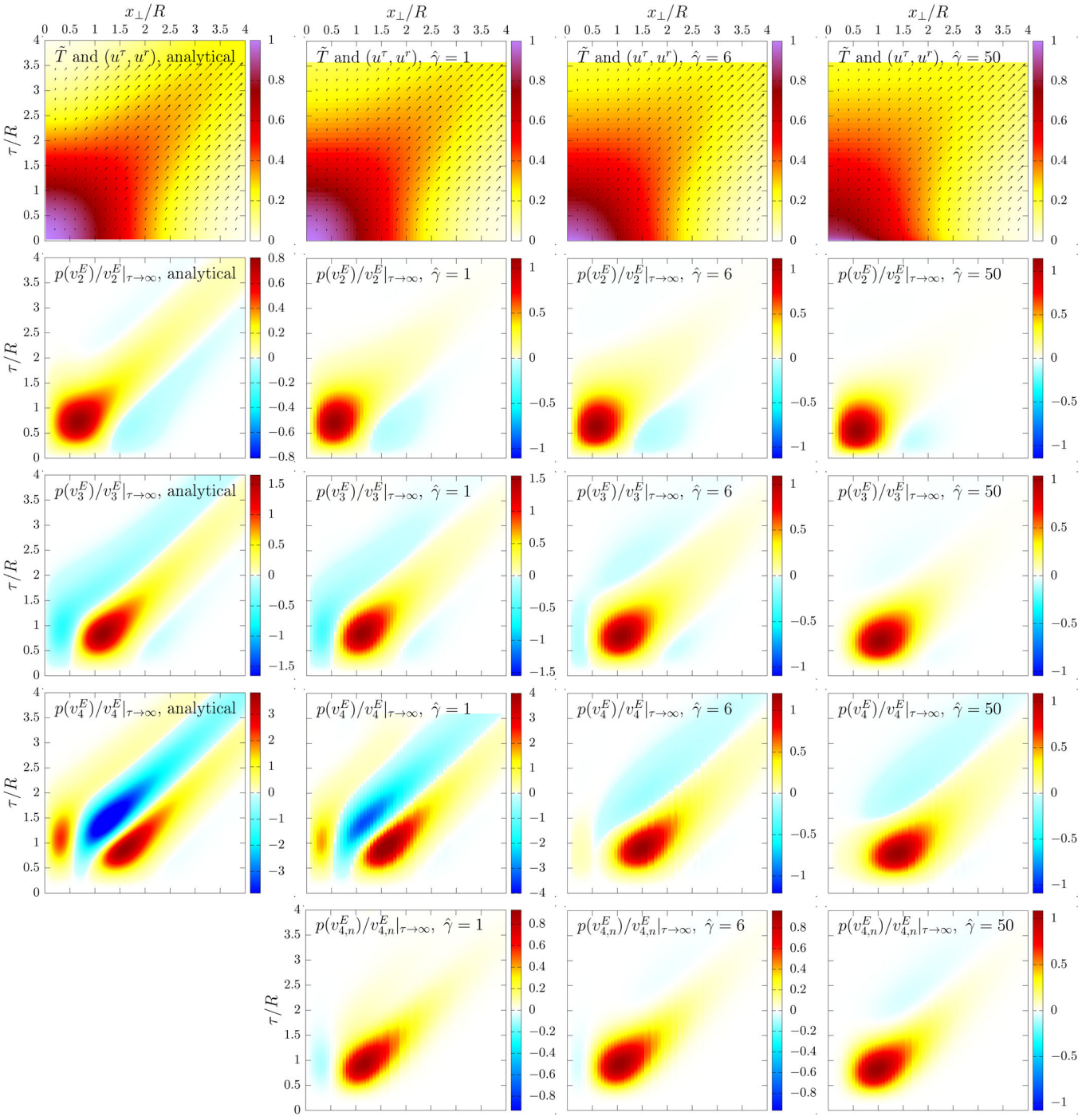

FIG. 5. (Top row) Space-time profiles of the effective temperature $\tilde{T}$ along with the temporal and radial components of the vector field u^μ, presented in the $x_\perp$-τ-plane for $\epsilon_n = 0.05$. (Bottom rows) Space-time profiles of the production rates of linear v_2^E, v_3^E, and v_4^E response (second to fourth row) as well as nonlinear v_4^E response (fifth row). Numerical results were obtained in the moment method.

spatial distribution and expansion of the system. The latter showcase how with increasing opacity, the system cools more rapidly in the center, and the transverse expansion proceeds much slower, resulting in a longer lifetime of the central fireball. Strong correlations of the temperature profile in τ and $x_\perp$ only develop at much later times when compared to the free-streaming limit, which exhibits a prominent diagonal line in the $\tilde{T}$-heat map. Inspection of the $p(v_n)$-heat maps reveals that different regions in the $x_\perp$-τ-plane contribute with different signs to the development of anisotropic flow v_n. By comparing the results for v_2, v_3, and v_4, one also observes that for larger n, the relevant regions extend more toward larger $x_\perp$, while at the same time, more of these regions appear, causing large cancellations between the different contributions. Specifically for small opacities, the structure of the heat maps of the v_n production rates can be related to the weight,

$$\begin{aligned}&|\mathbf{x}_\perp - \mathbf{v}_\perp \Delta\tau|^n \cos(n\phi_{\mathbf{x}_\perp - \mathbf{v}_\perp \Delta\tau, \mathbf{n}_\perp}) \\ &\quad = \sum_{j=0}^{n} (-1)^j \binom{n}{j} x_\perp^n \left(\frac{\Delta\tau}{x_T}\right)^j [\cos(n\phi_{\mathbf{x}_\perp \mathbf{n}_\perp}) \cos(j\phi_{\mathbf{x}_\perp \mathbf{p}_\perp}) \\ &\qquad - \sin(n\phi_{\mathbf{x}_\perp \mathbf{n}_\perp}) \sin(j\phi_{\mathbf{x}_\perp \mathbf{p}_\perp})], \end{aligned} \tag{157}$$

with which the anisotropic perturbations of the initial phase-space distribution propagate in free streaming. Since the evolution of the perturbation is expressed as a sum of $n+1$ terms containing different powers of $\Delta\tau/x_\perp$ with alternating signs, it will divide the $x_\perp$-τ-plane into $n+1$ regions of alternating signs depending on which one of these terms dominates. In addition, the production of the anisotropic flow v_ns will be weighted with the local effective temperature $\tilde{T}$ of the system, such that for small opacities, most of the contributions originate from the $\tau \sim x_\perp$ diagonal, so only $\Delta\tau/x_\perp$-terms that dominate close to that region will have a significant impact on the total $v_n(\tau)$. Specifically, for $n=2$, there is only one dominant term, which explains the monotonic increase of v_2 as a function of time seen in Fig. 3. Conversely, for $n=3$, one positive and one negative contribution are competing, with the positive one being slightly larger than the negative one, which is why for small opacities, v_3/e_3 is significantly smaller than v_2/e_2 and features a slight negative trend at late times. Finally, in the case of $n=4$, there are three relevant terms. At early times, the two positive contributions from the inner and outer border of the system win, and v_4 increases, but the one negative contribution surrounded by them in the $x_\perp$-τ-plane is closest to the diagonal and dominates at late times, resulting in a sign change for v_4 observed for the smallest opacities in Fig. 3.

With increasing opacity, one observes a clear change in the shapes of the regions, resulting in a shift of v_n production toward earlier τ and smaller $x_\perp$ in Fig. 5. However, more strikingly, the increase of opacity also leads to a change of the relative weights of different regions, developing toward a scenario with only one dominant positive contribution for all the v_ns at large opacity.

We finally note that the weighting with the effective temperature $\tilde{T}$ plays an important role in this mechanism, such that a different initial condition could result in different relative weights of the regions with different sign of the production rates, which can have notable effects on the buildup of the different flow harmonics. Clearly, one should expect that the higher order flow harmonics, where more cancellations appear, are more sensitive to changes of the initial conditions, and indeed we find that varying the parameter α that controls the radial profile (cf. Sec. II A) will have a notable influence on the $v_3(\tau)$ and $v_4(\tau)$-curves at small opacities.

Beyond the opacity dependence, one may also examine how the development of anisotropic flow $v_n(\tau)$ changes with the amplitude ϵ_n of the respective initial eccentricity. Figures 6 and 7 showcase how the curves of normalized flow spread with eccentricity for two representative fixed values of $\hat{\gamma}$. Somewhat surprisingly, we find that the curves exhibit only very small deviations from an entirely linear (quadratic) dependence on eccentricity in the linear v_2, v_3, and v_4 (quadratic v_4 and v_6) flow response, even for rather large eccentricities. The only response featuring a significant dependence on eccentricity is the cubic v_6 response to ϵ_2. While this holds true not only for the final values but also for the entire buildup and evolution as a function of τ/R, we remark, however, that these findings are probably specific to the particularly simple geometry considered in our setup, and it will therefore be important to extend such systematic studies of the opacity dependence of the flow response toward more realistic profiles of the transverse geometry.

Next, in order to further scrutinize the eccentricity dependence, we extract the extrapolated final values of v_n/ϵ_n, as well as of nonlinear v_4/ϵ_2^2, v_6/ϵ_3^2, and v_6/ϵ_2^3 at late times and plot them as a function of the square of the relevant eccentricity for several different opacities. Our results shown in Figs. 8 and 9 again confirm the surprisingly small deviations from perfect linear (quadratic) scaling of the flow response, with only very slight negative (positive) trends at large opacity and eccentricity. Our results in Fig. 8 appear to be in conflict with results previously obtained by Kurkela *et al.* [57] in the same setup. We note once again that although the absence of significant nonlinearity in the eccentricities may seem in conflict with conventional knowledge (see, e.g., [58,91,92]), we attribute this to the specific initial conditions considered within our setup, and we have explicitly checked that hydrodynamic simulations of the same initial conditions also lead to similar results for v_2/ϵ_2. Vice versa, the absence of nonlinearities within our setup also indicates that the significant nonlinearity observed for more realistic initial state models should be attributed to other features of the initial states considered in hydrodynamic simulations of

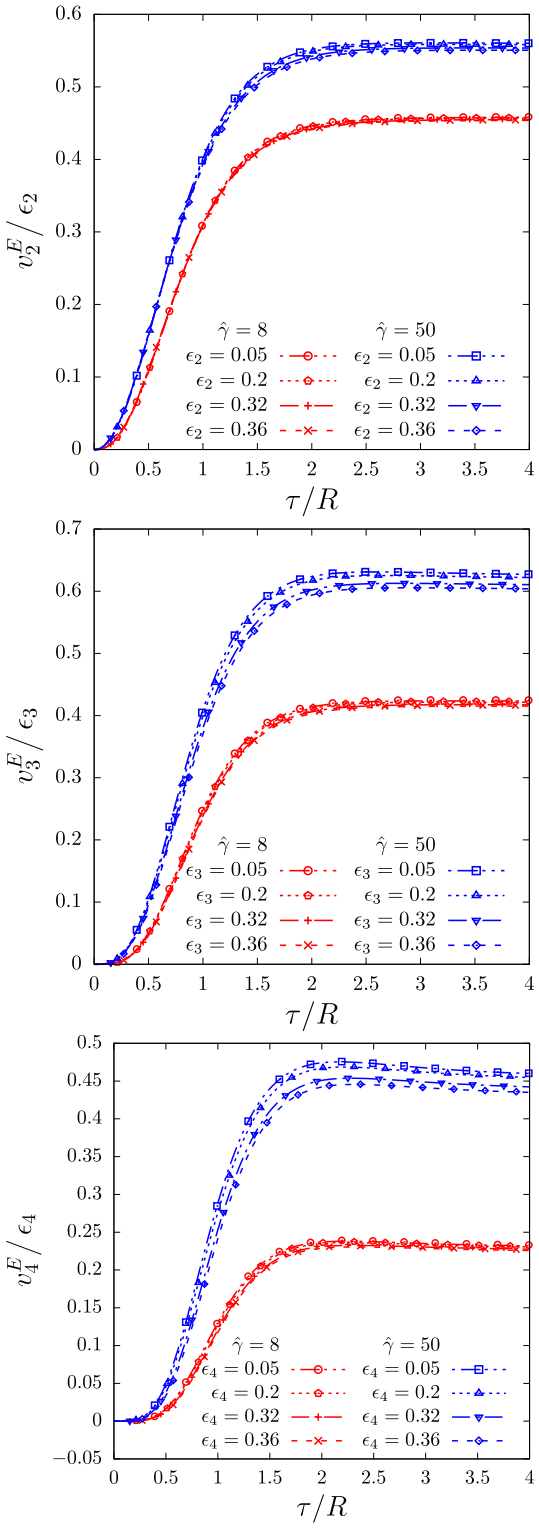

FIG. 6. Linear response coefficients v_n^E/ϵ_n as a function of τ/R for different opacities $\hat{\gamma}=8$ and $\hat{\gamma}=50$ and various different eccentricities ϵ_n. Lines denote results from the RLB method, and symbols show results from the moment method.

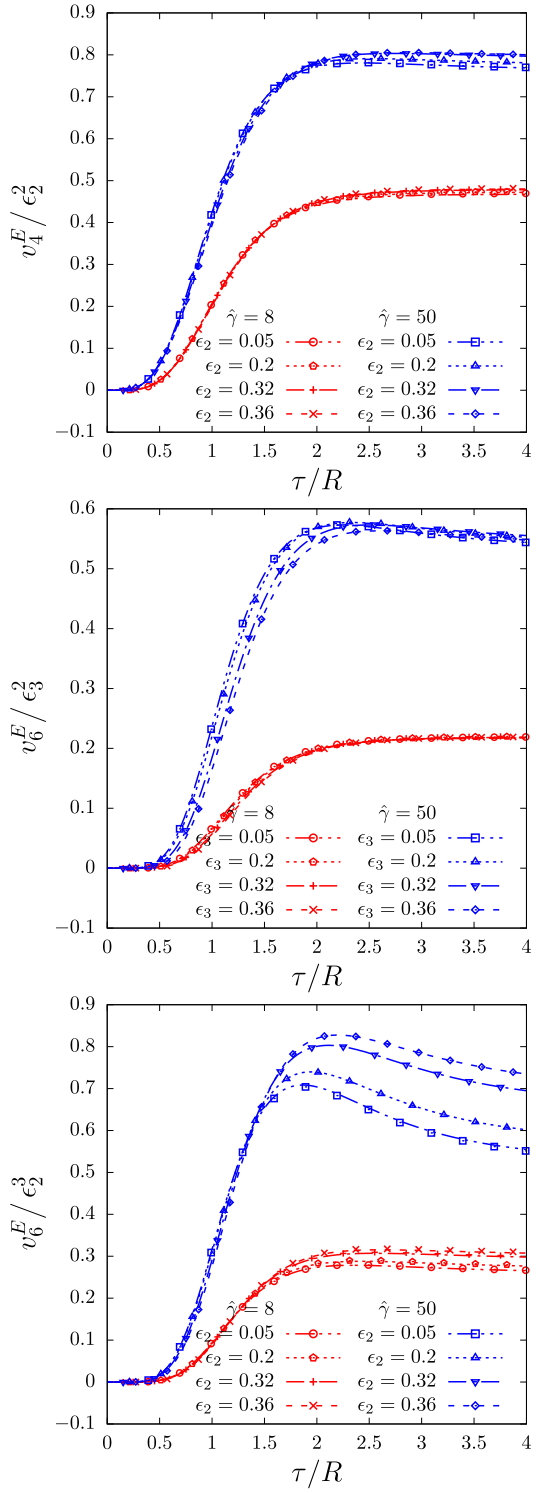

FIG. 7. Nonlinear response coefficients v_4^E/ϵ_2^2 (top), v_6^E/ϵ_3^2 (middle), and v_6^E/ϵ_2^3 (bottom) as a function of τ/R for different opacities $\hat{\gamma}=8$ and $\hat{\gamma}=50$ and various different eccentricities ϵ_n. Lines denote results from the RLB method, and symbols show results from the moment method.

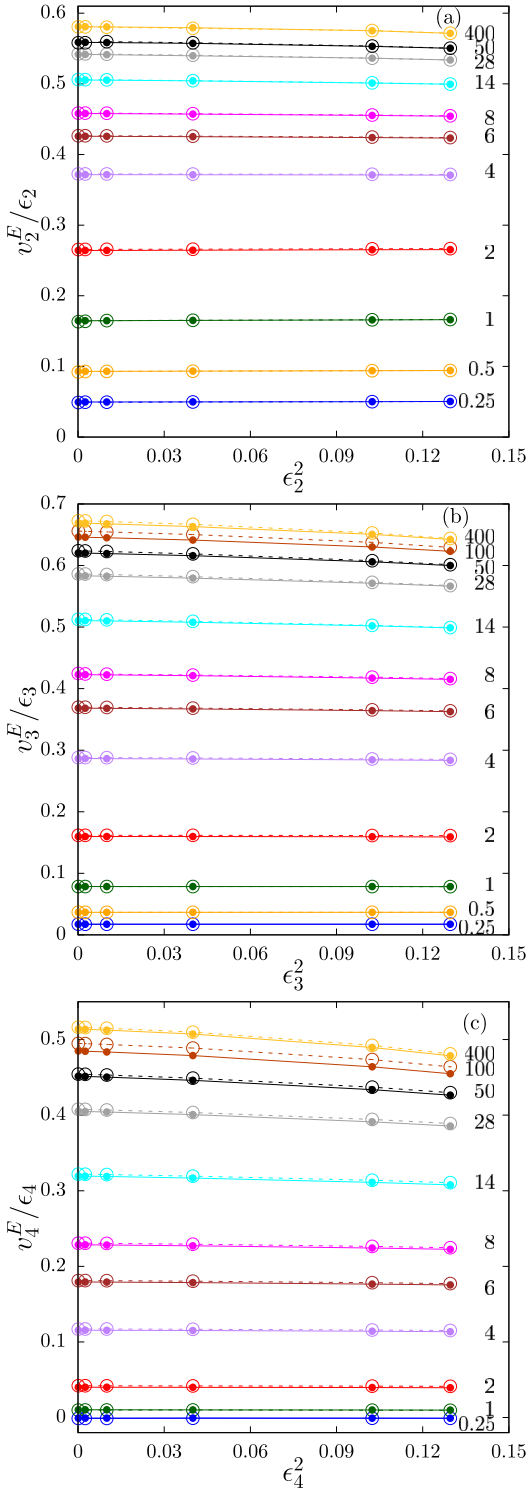

FIG. 8. Squared eccentricity (ϵ_n^2) dependence of the linear response coefficients $\kappa_{n,n} = v_n^E(\tau \to \infty)/\epsilon_n$ for elliptic flow $n = 2$ (top), triangular flow $n = 3$ (middle), and quadrangular flow $n = 4$ (bottom). Solid lines with filled circles denote results from the RLB method, while dotted lines with open circles were obtained in the moment method.

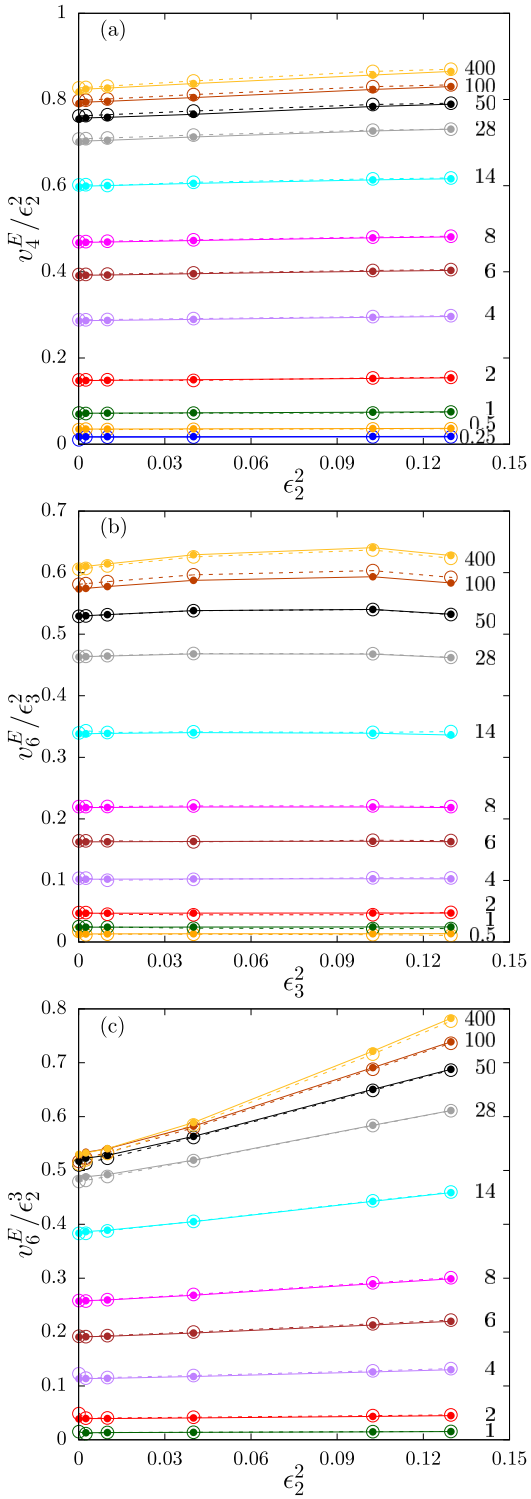

FIG. 9. Squared eccentricity (ϵ_n^2) dependence of the nonlinear response coefficients $\kappa_{4,22} = v_4^E(\tau \to \infty)/\epsilon_2^2$ (top), $\kappa_{6,33} = v_6^E(\tau \to \infty)/\epsilon_3^2$ (middle), and $\kappa_{6,222} = v_6^E(\tau \to \infty)/\epsilon_2^3$ (bottom). Solid lines with filled circles denote results from the RLB method, while dotted lines with open circles were obtained in the moment method.

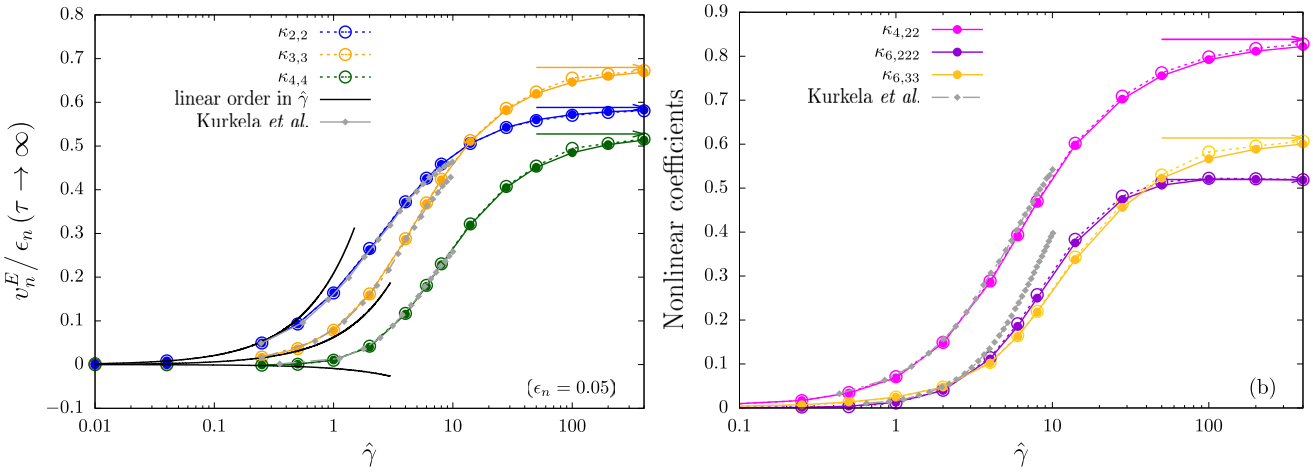

FIG. 10. Opacity ($\hat{\gamma}$) dependence of (left) the linear $\kappa_{n,n} = \lim_{\epsilon_n\to 0} v_n^E(\tau\to\infty)/\epsilon_n$ and (right) the nonlinear $\kappa_{n,mm} = \lim_{\epsilon_m\to 0} v_n^E(\tau\to\infty)/\epsilon_m^2$, $\kappa_{n,mmm} = \lim_{\epsilon_m\to 0} v_n^E(\tau\to\infty)/\epsilon_m^3$ response coefficients. Colored solid lines with filled circles denote results from the RLB method, while colored dotted lines with open circles were obtained in the moment method. The black solid lines show the results obtained to leading order in opacity expansion for the linear coefficients (left). Gray lines represent the results of Kurkela *et al.* in [57] [no such results are available for $\kappa_{6,33}$ in panel (b)]. Horizontal arrows indicate asymptotic values extracted from a fit to the numerical data at large opacities (see text).

heavy-ion collisions, which are not solely characterized in terms of the usual eccentricities.

Since the flow response to the initial eccentricity is essentially linear within our setup, our findings for the development of transverse flow can be compactly summarized in Fig. 10, where we present results for the $\hat{\gamma}$-dependence of the response coefficients $\kappa_{n,n} = \lim_{\epsilon_n\to 0} v_n/\epsilon_n$, as well as $\kappa_{4,22} = \lim_{\epsilon_2\to 0} v_4/\epsilon_2^2$, $\kappa_{6,33} = \lim_{\epsilon_3\to 0} v_6/\epsilon_3^2$, and $\kappa_{6,222} = \lim_{\epsilon_2\to 0} v_6/\epsilon_2^3$ estimated from our data at $\epsilon = 0.05$. Besides the numerical results, we also indicate the linearized analytical approximation in Eqs. (83)–(85) and the numerical results of Kurkela *et al.* [57]. Despite the discrepancy in the results for the eccentricity dependence, we generally find good agreement with Kurkela *et al.* in the linear response at low opacities ($\hat{\gamma} \lesssim 10$), which only starts to deviate slightly at larger opacities.

Concerning the opacity dependence, one finds that at low opacities up to $\hat{\gamma} \lesssim 1$, the linear response coefficients are reasonably well described by the leading order opacity expansion $\kappa_{n,n} \sim \hat{\gamma}$ in Eqs. (83)–(85). However, one should note that, due to the intricate space-time structure of v_n production, the higher harmonic coefficients are increasingly sensitive to changes in the underlying dynamics, such that, e.g., $\kappa_{4,4}$, starts to deviate from the leading order opacity expansion already at smaller values of $\hat{\gamma}$. When increasing the opacity further, one observes a sizeable change in the linear and nonlinear flow response coefficients for $1 \lesssim \hat{\gamma} \lesssim 100$, which is no longer captured by the leading order opacity expansion. Eventually, for very large opacities $\hat{\gamma} \gtrsim 100$, the opacity dependence of the linear and nonlinear response coefficients becomes weaker and weaker, indicating a saturation toward a finite large opacity limit. Empirically, we find that in this regime, the opacity dependence of the response coefficients can be well approximated by a constant asymptotic value and a power-law correction, with the asymptotic values $\kappa(\hat{\gamma}\to\infty)$ indicated by horizontal arrows in Fig. 10.

C. Energy flow and hydrodynamic limit

So far, we have employed an effective kinetic description to study longitudinal cooling and the development of transverse flow as a function of the opacity parameter $\hat{\gamma}$. While at small opacities $\hat{\gamma} \ll 1$, the results from numerical simulations are well described by the first interaction correction to free streaming, one generally expects that in the opposite limit of large opacities $\hat{\gamma} \gg 1$, the effective kinetic description approaches the limit of dissipative and eventually ideal hydrodynamics. Hence, in order to investigate to what extent this expectation holds true, we will now compare our results from kinetic theory with numerical simulations in Müller-Israel-Stewart type second order relativistic viscous hydrodynamics.

We employ the publicly available vHLLE code originally introduced in Ref. [72] and extend the latest GitHub branch[9] to include the initial conditions considered in this paper. Apart from the conservation equation for the stress-energy tensor, $\nabla_\nu T^{\mu\nu} = 0$, the code implements the Müller-Israel-Stewart equations for the evolution of the pressure

[9]Commit number `efa9e28d24d5115a8d8134852-32fb342b38380f0`.

deviator $\pi^{\mu\nu}$, which, for the case of a conformal fluid, reduce to [93]

$$\dot{\pi}^{\langle\mu\nu\rangle} = \frac{2\eta\sigma^{\mu\nu} - \pi^{\mu\nu}}{\tau_\pi} - \frac{\delta_{\pi\pi}}{\tau_\pi}\pi^{\mu\nu}\theta + \frac{\phi_7}{\tau_\pi}\pi_\alpha^{\langle\mu}\pi^{\nu\rangle\alpha} - \frac{\tau_{\pi\pi}}{\tau_\pi}\pi_\alpha^{\langle\mu}\sigma^{\nu\rangle\alpha}, \tag{158}$$

where $\sigma_{\mu\nu} = 2\nabla_{\langle\mu}u_{\nu\rangle}$ is the shear tensor, $\theta = \nabla_\mu u^\mu$ is the expansion scalar, while the transport coefficients appearing above satisfy [94]

$$\tau_\pi = \frac{5\eta}{sT}, \quad \frac{\delta_{\pi\pi}}{\tau_\pi} = \frac{4}{3}, \quad \phi_7 = \frac{9}{70p}, \quad \frac{\tau_{\pi\pi}}{\tau_\pi} = \frac{10}{7}. \tag{159}$$

We note already at this stage that the early time behavior in ideal and viscous hydrodynamics does not agree with the early time free-streaming limit of kinetic theory, which, as pointed in [57,95], leads to an unphysical behavior of $dE_\perp/d\eta$ at early times, which makes the scaling variable $\hat{\gamma}$ ill defined in the limit $\tau_0 \to 0$. While in [57], this problem was addressed by modifying the initial conditions and matching the energy per unit rapidity at a later time $\tau/R = 1$ of the evolution, we follow the more common procedure and choose a finite initial time τ_0, where we initialize the energy density as in Eqs. (14) and (15) and set the components of the shear stress tensor, $\pi^{\mu\nu}$, to[10]

$$\tau_0^{-2}\pi^{\eta\eta} = -2\pi^{xx} = -2\pi^{yy} = -p, \tag{160}$$

which ensures vanishing longitudinal pressure, to comply with the initial conditions for kinetic theory in Eq. (11).[11] Similarly, we fix the value of the shear viscosity to entropy density ratio η/s for a given value of $\hat{\gamma}$ in the same way as for RTA, via Eq. (31), evaluated at initial time τ_0. By comparing kinetic theory and hydrodynamic simulations with the same finite τ_0, we can then achieve a direct comparison and, in addition, investigate the dependence on the initialization time τ_0 in the two different theories.

Evaluating the energy-weighted flow harmonics v_n^E considered in this paper, a Cooper-Frye-like mechanism should be considered to reconstruct the phase-space distribution function from the hydrodynamic fields e, u^μ, and $\pi^{\mu\nu}$. We circumvent this ambiguity by instead referring to the stress-energy anisotropy ϵ_p, which, according to Eq. (37), can be defined directly in terms of the components of the energy-momentum tensor. Since $T^{\mu\nu}$ is fundamentally accessible in both kinetic theory and hydrodynamics, a comparison between the two theories can be made unambiguously at the level of ϵ_p. The quantity ϵ_p measures the second harmonic modulation of the energy flow and our kinetic theory simulations exhibits almost identical behavior of ϵ_p and the energy-weighted harmonic coefficient v_2^E. Since we are not aware of generalizations of ϵ_p higher order flow harmonics, we will therefore restrict our attention to $n = 2$ perturbations, with initial eccentricity $\epsilon_2 = 0.05$.[12]

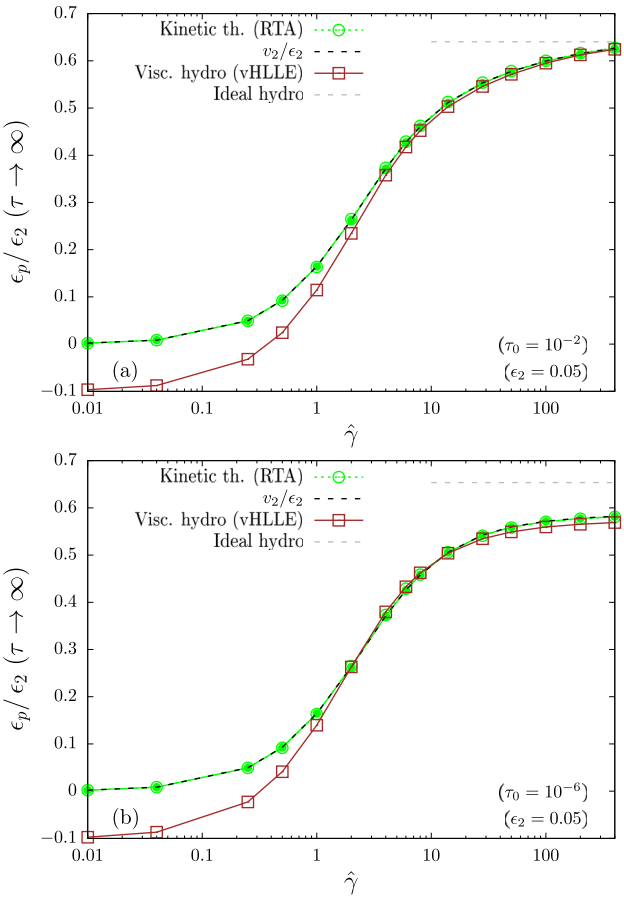

FIG. 11. Opacity ($\hat{\gamma}$) dependence of the energy-flow response ϵ_p/ϵ_2 for two different initialization times $\tau_0/R = 10^{-2}$ (top) and $\tau_0/R = 10^{-6}$ (bottom). Two results are plotted for kinetic theory: Those from the RLB method are plotted as a green solid line with filled circles and those from the moments method are plotted as a green dashed line with open circles. All results are for $\epsilon_2 = 0.05$.

Our results for the elliptic energy-flow response are compactly summarized in Fig. 11, where we compare the opacity dependence of ϵ_p/ϵ_2 in kinetic theory (RTA) and hydrodynamics (vHLLE) for two different initialization times $\tau_0/R = 10^{-2}, 10^{-6}$ in the top and bottom panels. When

[10]We employ a conformal equation of state $e = 3p$.

[11]Since at very early times, the evolution in viscous hydrodynamics and kinetic theory does not agree, another conceivable option is to initialize the hydrodynamic simulation on the hydrodynamic attractor for Bjorken flow [57,95]. We have also performed such simulations and find no significant differences regarding the development of transverse flow.

[12]We have checked that, similar to the kinetic theory results in Fig. 8, nonlinear contributions $\epsilon_p \sim \epsilon_2^3$ are sufficiently small to be neglected for the linear response analysis of ϵ_p/ϵ_2.

considering the larger initialization time $\tau_0/R = 10^{-2}$, one finds that viscous hydrodynamics provides a reasonable description of kinetic theory for $\hat{\gamma} \gtrsim 5$, with both curves smoothly approaching the ideal hydrodynamic limit for large opacities, as indicated by the gray dashed line. When considering a much smaller initialization time, $\tau_0/R = 10^{-6}$, we find small deviations between kinetic theory and hydrodynamics in the same opacity range. While these deviations might not be very sizeable, they notably do not steadily decrease with increasing opacity, as one would naively expect. Moreover, a perhaps more evident observation is that neither of the two curves appears to approach the ideal hydrodynamics result, such that even when extrapolated to infinite opacity, the RTA value ($\simeq$0.59) slightly differs from the vHLLE value ($\simeq$0.57), and both fall about 10% short of the ideal hydrodynamic limit ($\simeq$0.64).

Even though this behavior may appear counterintuitive at first sight, it can ultimately be traced back to the noncommutativity of the limits $\tau_0 \to 0$, where the system is subject to a rapid longitudinal expansion, and $\hat{\gamma} \to \infty$, where hydrodynamics emerges from kinetic theory as the system undergoes rapid equilibration. Starting from kinetic theory, it is clear that for any finite opacity $\hat{\gamma}$, the system is initially far from equilibrium and behaves as approximately free streaming, until on time scales $\tau_{\mathrm{eq}}/R \sim \hat{\gamma}^{-4/3}$, the system undergoes equilibration, and the subsequent evolution can be approximately described by viscous or even ideal fluid dynamics. While in the limit $\hat{\gamma} \to \infty$, the equilibration time $\tau_{\mathrm{eq}}/R \to 0$ and fluid dynamics becomes applicable at earlier and earlier times, the early time free streaming and initial approach toward equilibrium is never correctly described by fluid dynamics. The results in Fig. 11 thus provide a clear illustration of the fact that at very early times, the system is necessarily out of equilibrium, and the two limits $\hat{\gamma} \to \infty$ and $\tau_0 \to 0$ are in general not commutative.

Even though at large opacities, the mismatch between kinetic theory and hydrodynamics occurs only at very early times, this affects, e.g., the longitudinal cooling and can still have a notable effect on the development of anisotropic flow at later times, which is seen in Fig. 11. We are thus led to conclude that a nonequilibrium description of the early time dynamics is inevitable to accurately describe the development of anisotropic flow, even at relatively large opacities.

As a final remark to the comparison of opacity dependencies in the different descriptions, we note that for any finite τ_0, kinetic theory and viscous hydrodynamics will approach ideal hydrodynamics for sufficiently large opacities where the equilibration time τ_{eq} becomes smaller than the initialization time τ_0. While the results shown in Fig. 12 provide an explicit illustration of this behavior, the convergence toward ideal hydrodynamics at large opacities corresponds to the incorrect order of limits, as physically, one needs to account for the entire space-time evolution of the system; i.e., the limit $\tau_0 \to 0$ has to be taken before $\hat{\gamma} \to \infty$.

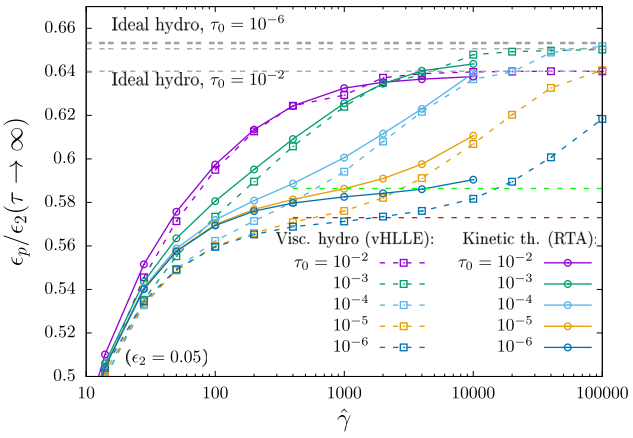

FIG. 12. Opacity ($\hat{\gamma}$) dependence of the response coefficient ϵ_p/ϵ_2 in kinetic theory (RTA, obtained using the RLB method), viscous (vHLLE), and ideal hydrodynamics for different initialization times $\tau_0/R = 10^{-2} - 10^{-6}$. Convergence toward ideal hydrodynamics is only observed when the initialization time becomes smaller than the equilibration time of the system.

One may wonder how the increasingly short period of nonequilibrium evolution at early times can have such a significant impact on the transverse flow, which only develops on much later times scales $\tau/R \gtrsim 0.1$. While it is true that at very early times, the system does not develop a significant amount of transverse expansion and can locally be described by Bjorken flow as discussed in Sec. V A, it is equally important to realize that the early-time dynamics is nevertheless inhomogeneous in the transverse plane. Due to the fact that the initial energy density locally sets the scale for the Bjorken evolution, some regions will experience a faster cooling relative to others, thereby changing the shape of the energy density distribution in transverse space. Due to this phenomenon of inhomogenous longitudinal cooling, the geometric eccentricities will be modified even before the transverse expansion sets in. Since the anisotropic flow is built up solely due to transverse expansion, its magnitude is determined by the value of the eccentricity at the onset of transverse expansion. We therefore conclude that differences in the longitudinal cooling at early times are ultimately responsible for the observed differences in the transverse flow.

We illustrate this behavior in Fig. 13, where we present the evolution of the coordinate space eccentricity ϵ_2 as a function of time τ/R. Different colored curves in the top panel show the evolution of ϵ_2 in kinetic theory for different opacities. Similarly, the bottom panel shows the corresponding results obtained in viscous hydrodynamics (vHLLE). The ideal hydrodynamics result is shown for comparison as a solid black line in both panels. Starting around $\tau \sim 0.1R$, all curves exhibit a significant drop due to the onset of transverse expansion. However, in kinetic theory and viscous hydrodynamics, the eccentricity decreases even before that

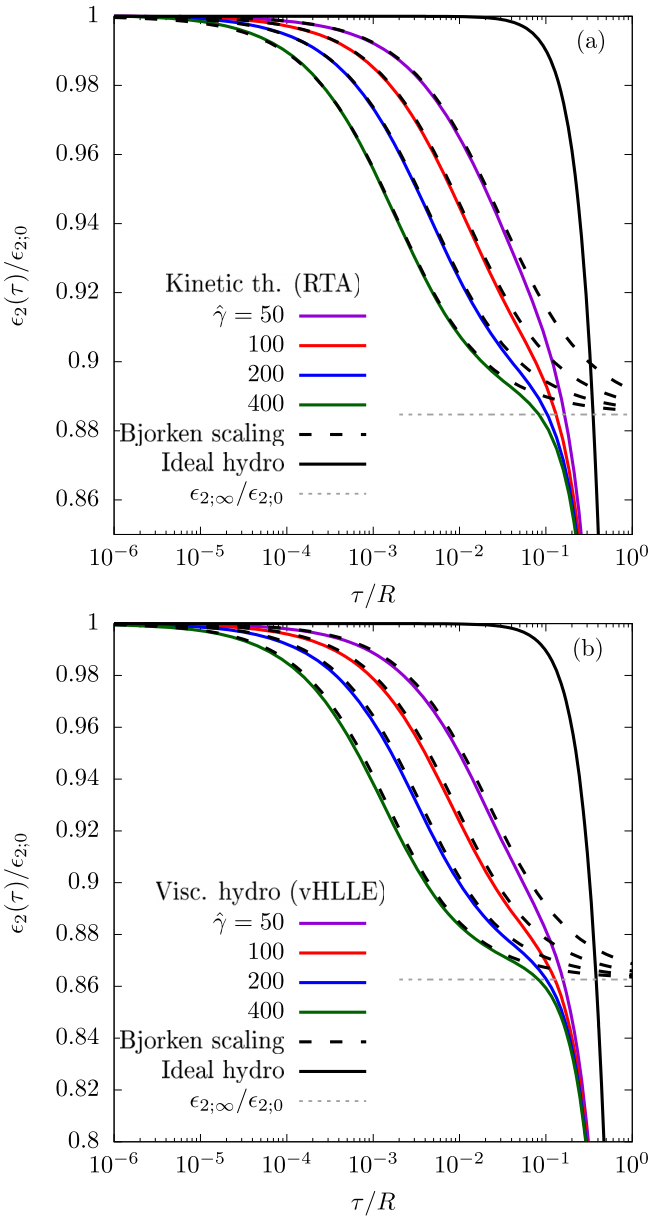

FIG. 13. Comparison of the evolution of ϵ_2 normalized to its initial value $\epsilon_{2;0}$ on a logarithmic timescale for kinetic theory obtained using the moments method (top) and viscous hydrodynamics (bottom). Also shown are the corresponding results in Bjorken flow scaling approximation (dashed black lines) and ideal hydrodynamics (solid black lines). Gray dashed lines show the limit in Eq. (161) in the absence of transverse expansion.

due to the previously discussed phenomenon of inhomogeneous longitudinal cooling. Strikingly, this effect can also be described (semi)analytically by approximating the dynamics as a collection of local Bjorken flows in a similar way to what was discussed in Sec. V A, which yields results for the decrease of ϵ_2 that we plotted as dashed black lines. We note that the limiting behavior for this decrease can be obtained as

$$\lim_{\tau\to\infty} \frac{\epsilon_2(\tau)}{\epsilon_{2;0}} = \frac{(1-q/4)^3}{(1-q/6)^3}, \tag{161}$$

where q is related to the behavior of the universal function $\mathcal{E}(\tilde{w}) \sim \tilde{w}^q$ at small $\tilde{w}$, such that in kinetic theory, $q = 4/9$ as indicated in Eq. (142), whereas for the hydrodynamic theory in Eq. (158), one has $q = (\sqrt{505} - 13)/18 \simeq 0.526$. Evaluating Eq. (161) for the above values of q, one obtains a $\sim$11.5% (RTA) and 13.7% (vHLLE) decrease of ϵ_2 solely due to the longitudinal expansion, as indicated by the gray dashed lines in Fig. 13. Hence, this effect indeed takes on the correct magnitude to be able to describe the difference of $\sim$10% in the large opacity limits of kinetic theory and viscous hydro compared to ideal hydrodynamics.

VI. CONCLUSIONS AND OUTLOOK

We employed the Boltzmann equation in the (conformal) RTA as a simple model to study the space-time dynamics of small and large systems created in high-energy hadronic collisions. Within the simple effective kinetic description described in Sec. II, the evolution of the system depends on a single dimensionless opacity parameter $\hat{\gamma}$ that combines the system size and energy dependencies, and we estimate $\hat{\gamma}$ to range from values $\lesssim 1$ in p + Pb collisions to ≈ 10 in Pb + Pb collisions at LHC energies [cf. Eqs. (32) and (33)].

We performed (semi)analytic calculations at leading order in opacity $\hat{\gamma}$ (cf. Sec. III) and developed first principles numerical simulations (cf. Sec. IV) to investigate the longitudinal cooling of the transverse energy per unit rapidity, $\frac{dE_\perp/d\eta}{dE_\perp^{(0)}/d\eta}$, and the development of transverse flow quantified by the (energy-weighted) flow harmonics v_n^E for a large range of opacities.

We find that with increasing opacities, pressure isotropization takes place at earlier and earlier times, such that for large opacities $\hat{\gamma} \gtrsim 1$, the onset of longitudinal cooling of the system is well described by one-dimensional Bjorken dynamics, until at later times $\tau/R \gtrsim 0.1$, when the effects of the transverse expansion can no longer be ignored.

By studying the response to anisotropic perturbations of the initial energy density, we investigated the development of transverse flow from low to high opacities. While for small opacities, $\hat{\gamma} \lesssim 1$, the development of transverse flow is reasonably well described by the leading order opacity corrections to free streaming, we find that for $1 \lesssim \hat{\gamma} \lesssim 100$, the linear and nonlinear flow response exhibits a strong opacity dependence and eventually saturates for large opacities $\hat{\gamma} \gtrsim 100$.

Even though one naively expects the results for large opacities $\hat{\gamma} \gg 1$ to approach the hydrodynamic limit, it turns out that subtleties of the limits $\hat{\gamma} \to \infty$ and $\tau_0 \to 0$ provide a restriction on the accuracy of hydrodynamic descriptions. Since the early time preequilibrium dynamics of the system cannot be accurately described by ordinary viscous or ideal hydrodynamics, deviations between all

approaches persist even at very large opacities. With respect to RTA results, we found discrepancies of the viscous and ideal hydro results of the order of ∼2.5% and ∼12%, respectively. However, as these discrepancies can be mostly attributed to the phenomenon of inhomogeneous longitudinal cooling, we believe that the inclusion of a more appropriate preequilibrium description as in KØMPØST [96,97] may significantly improve the agreement between microscopic and macroscopic descriptions (see also [80]). Similarly, it is also conceivable that resummed hydrodynamic approaches such as anisotropic hydroynamics (aHydro) [98–102] can accurately describe the inhomogeneous longitudinal cooling, and it will be interesting to further investigate this in the future.

While our current study provides a detailed assessment of the development of transverse flow from very small to very large opacities, some of the shortcomings should be addressed prior to inferring phenomenological conclusions for proton-proton, proton-nucleus, and nucleus-nucleus collisions. Evidently, it would be important to perform event-by-event studies with a more realistic transverse collision geometry, which is conceptually straightforward but will require significantly larger computation time. Beyond such straightforward extensions, it would also be interesting to consider more realistic collision kernels [55] and investigate the effects of a nonconformal equation of state, which however will require additional theoretical developments.

ACKNOWLEDGMENTS

We thank N. Borghini, H. Elfner, N. Kersting, A. Mazeliauskas, B. Schenke, U. A. Wiedemann, H. Roch, M. Borrell Martinez, A. Shark, and P. Aasha for valuable discussions. This work is supported by the Deutsche Forschungsgemeinschaft (DFG, German Research Foundation) through the CRC-TR 211 "Strong-interaction matter under extreme conditions" Project No. 315477589—TRR 211. V. E. A. gratefully acknowledges the support of the Alexander von Humboldt Foundation through a Research Fellowship for postdoctoral researchers. Numerical calculations presented in this work were performed at Paderborn Center for Parallel Computing (PC2) and the Center for Scientific Computing (CSC) at the Goethe-University of Frankfurt, and we gratefully acknowledge their support.

APPENDIX A: FREE STREAMING THE ANISOTROPIES

In linear order of the opacity expansion, the dynamics of the anisotropies is naturally dominated by the free-streaming limit, as will also be more evident from the calculations in the following sections. It is therefore pivotal to examine how the anisotropic factors of $x_\perp^n \cos(n\phi_{\mathbf{x}_\perp\mathbf{n}_\perp})$ that are part of the initial condition in Eqs. (14) and (15) behave under free streaming according to the propagation as given in Eq. (48). The notation $\phi_{\mathbf{x}_\perp\mathbf{n}_\perp} = \phi_x - \Psi_n$ was introduced in Eq. (16). For this purpose, it is convenient to rewrite the $\cos(n\phi)$ and $\sin(n\phi)$ in terms of the Chebyshev polynomials of the first and second kind [[103], Ch. 18]:

$$\cos(n\phi) = T_n(\cos(\phi)), \quad \sin(n\phi) = \sin(\phi)U_{n-1}(\cos(\phi)). \tag{A1}$$

The explicit form of the Chebyshev polynomials,

$$T_n(z) = \frac{n}{2}\sum_{k=0}^{\lfloor\frac{n}{2}\rfloor}(-1)^k\frac{(n-k-1)!}{(n-2k)!k!}(2z)^{n-2k},$$
$$U_n(z) = \sum_{k=0}^{\lfloor\frac{n}{2}\rfloor}(-1)^k\binom{n-k}{k}(2z)^{n-2k}, \tag{A2}$$

can be used to express $\cos(n\phi)$ and $\sin(n\phi)$ in terms of powers of $\cos\phi$. Under free streaming (44), the factor $x_\perp^n\cos(n\phi_{\mathbf{x}_\perp\mathbf{n}_\perp})$ evolves to

$$|\mathbf{x}_\perp - \mathbf{v}_\perp\Delta\tau|^n\cos(n\phi_{\mathbf{x}_\perp-\mathbf{v}_\perp\Delta\tau,\mathbf{n}_\perp}) = |\mathbf{x}_\perp - \mathbf{v}_\perp\Delta\tau|^n T_n\left(\frac{(\mathbf{x}_\perp - \mathbf{v}_\perp\Delta\tau)\cdot\mathbf{n}_\perp}{|\mathbf{x}_\perp - \mathbf{v}_\perp\Delta\tau|}\right), \tag{A3}$$

where Eq. (A1) was employed on the right-hand side. In the above, the time lapse $t(\tau,\tau_0,y-\eta)$ was replaced by $\Delta\tau = \tau - \tau_0$ by virtue of Eq. (47).

The Chebyshev polynomials obey the identity,

$$z^n = |z|^n T_n\left(\frac{a}{|z|}\right) + ib|z|^{n-1}U_{n-1}\left(\frac{a}{|z|}\right), \tag{A4}$$

where a and b are real numbers, and $z = a + ib$ is a complex number. Denoting $\phi_{\mathbf{p}_\perp\mathbf{n}_\perp} = \phi_p - \Psi_n$, we set

$$a \to x_\perp\cos(\phi_{\mathbf{x}_\perp\mathbf{n}_\perp}) - \Delta\tau\cos(\phi_{\mathbf{p}_\perp\mathbf{n}_\perp}),$$
$$b \to x_\perp\sin(\phi_{\mathbf{x}_\perp\mathbf{n}_\perp}) - \Delta\tau\sin(\phi_{\mathbf{p}_\perp\mathbf{n}_\perp}),$$
$$z \to x_\perp e^{i\phi_{\mathbf{x}_\perp\mathbf{n}_\perp}} - \Delta\tau e^{i\phi_{\mathbf{p}_\perp\mathbf{n}_\perp}}, \tag{A5}$$

such that $\mathrm{Re}(z^n)$ is just the expression on the left-hand side of Eq. (A3), and an expression with a very simple dependence on $\phi_{\mathbf{x}_\perp\mathbf{p}_\perp} = \phi_x - \phi_p$ can be derived:

$$|\mathbf{x}_\perp - \mathbf{v}_\perp\Delta\tau|^n\cos(n\phi_{\mathbf{x}_\perp-\mathbf{v}_\perp\Delta\tau,\mathbf{n}_\perp}) = \sum_{j=0}^{n}\binom{n}{j}x_\perp^{n-j}(-\Delta\tau)^j[\cos(n\phi_{\mathbf{x}_\perp\mathbf{n}_\perp}) \times\cos(j\phi_{\mathbf{x}_\perp\mathbf{p}_\perp}) - \sin(n\phi_{\mathbf{x}_\perp\mathbf{n}_\perp})\sin(j\phi_{\mathbf{x}_\perp\mathbf{p}_\perp})]. \tag{A6}$$

APPENDIX B: SOLVING INTEGRALS IN LANDAU MATCHING

In order to be able to perform the necessary integrals of the kernel according to Eq. (76), we will need specific expressions for ϵ and u^μ, meaning that we need to compute the exact form of $T^{(0)\mu\nu}$ and $\delta T^{(0)\mu\nu}$ by solving the integrals given in Sec. III D.

As we will discuss below, we can break the integration down to solving integrals of an exponential of $\cos(\phi)$ multiplied with powers of trigonometric functions. These can be expressed in terms of modified Bessel functions of the first kind:

$$\int \mathrm{d}\phi e^{a\cos(\phi)}\cos(n\phi) = 2\pi I_n(a), \tag{B1}$$

$$\int \mathrm{d}\phi e^{a\cos(\phi)}\cos(n\phi)\cos^m(\phi) = 2\pi I_n^{(m)}(a), \tag{B2}$$

$$\int \mathrm{d}\phi e^{a\cos(\phi)}\sin(n\phi) = 0, \tag{B3}$$

$$\int \mathrm{d}\phi e^{a\cos(\phi)}\sin(n\phi)\sin(\phi) = 2\pi I_n'(a) - 2\pi I_{n+1}(a), \tag{B4}$$

$$\int \mathrm{d}\phi e^{a\cos(\phi)}\sin(n\phi)\cos(\phi)\sin(\phi) = 2\pi I_n''(a) - 2\pi I_{n+1}'(a). \tag{B5}$$

It is straightforward to see that $T^{(0)\mu\nu}$ is indeed of this form as

$$T^{(0)\mu\nu} = \frac{\tau_0}{\tau}\int \frac{\mathrm{d}\phi_p}{2\pi} v_\perp^\mu v_\perp^\nu \bar{\epsilon}(\tau_0, \mathbf{x}_\perp - \Delta\tau \mathbf{v}_\perp), \tag{B6}$$

where $v_\perp^\mu = (1, \cos\phi_p, \sin\phi_p, 0)$ has no longitudinal component under free streaming due to the $\delta(y-\eta)$ function in Eq. (48). The integral with respect to $p_\perp$ was performed according to Eq. (12). At zeroth order, we took into account only the isotropic part of the initial energy density profile $\bar{\epsilon}$, introduced in Eq. (14), which is evaluated at shifted coordinates, according to

$$\bar{\epsilon}(\tau_0, \mathbf{x}_\perp - \Delta\tau\mathbf{v}_\perp) = \frac{1}{\pi R^2 \tau_0}\frac{\mathrm{d}E_\perp^{(0)}}{\mathrm{d}\eta}\exp\left(-\frac{x_\perp^2 + \Delta\tau^2 - 2x_\perp\Delta\tau\cos(\phi_x - \phi_p)}{R^2}\right). \tag{B7}$$

Using the integral formulae given in Eqs. (B1)–(B5), the components of the stress-energy tensor introduced in Eq. (53) can be computed to be

$$T^{(0)\tau\tau} = \frac{1}{\tau}\frac{1}{\pi R^2}\frac{\mathrm{d}E_\perp^{(0)}}{\mathrm{d}\eta}\exp\left(-\frac{x_\perp^2 + \Delta\tau^2}{R^2}\right)I_0(2b), \tag{B8}$$

$$T^{(0)\tau\perp} = \frac{1}{\tau}\frac{1}{\pi R^2}\frac{\mathrm{d}E_\perp^{(0)}}{\mathrm{d}\eta}\exp\left(-\frac{x_\perp^2 + \Delta\tau^2}{R^2}\right)I_1(2b), \tag{B9}$$

$$T^{(0)\perp\perp} = \frac{1}{\tau}\frac{1}{\pi R^2}\frac{\mathrm{d}E_\perp^{(0)}}{\mathrm{d}\eta}\exp\left(-\frac{x_\perp^2 + \Delta\tau^2}{R^2}\right)I_2(2b), \tag{B10}$$

$$T^{(0)\mathbb{1}} = \frac{1}{\tau}\frac{1}{\pi R^2}\frac{\mathrm{d}E_\perp^{(0)}}{\mathrm{d}\eta}\exp\left(-\frac{x_\perp^2 + \Delta\tau^2}{R^2}\right)[I_0(2b) - I_0''(2b)], \tag{B11}$$

where we defined $b = \frac{x_\perp\Delta\tau}{R^2}$.

The anisotropic part $\delta T^{(0)\mu\nu}$,

$$\delta T^{(0)\mu\nu} = \frac{\tau_0}{\tau}\int \frac{\mathrm{d}\phi_{\mathbf{x}_\perp\mathbf{p}_\perp}}{2\pi} v_\perp^\mu v_\perp^\nu \delta\epsilon(\tau_0, \mathbf{x}_\perp - \Delta\tau\mathbf{v}_\perp), \tag{B12}$$

exhibits a dependence on the angle $\phi_{\mathbf{x}_\perp\mathbf{n}_\perp}$ due to the form (15) of the anisotropic part of the initial energy profile, which is evaluated at shifted coordinates according to

$$\delta\epsilon(\tau_0, \mathbf{x}_\perp - \Delta\tau\mathbf{v}_\perp) = \frac{1}{\pi R^2\tau_0}\frac{\mathrm{d}E_\perp^{(0)}}{\mathrm{d}\eta}\exp\left[-\bar{\alpha}\frac{|\mathbf{x}_\perp - \Delta\tau\mathbf{v}_\perp|^2}{R^2}\right]\delta_n\left(\frac{|\mathbf{x}_\perp - \Delta\tau\mathbf{v}_\perp|}{R}\right)^n\cos(n\phi_{\mathbf{x}_\perp\mathbf{n}_\perp}). \tag{B13}$$

Solving the integrals in Eq. (B12) is a bit more difficult, requiring the computation of an angular integral of the free-streamed anisotropies. We have already seen in Appendix A how we can rewrite them into a term with a straightforward $\phi_{\mathbf{x}_\perp\mathbf{p}_\perp}$-dependence. An additional $\phi_{\mathbf{x}_\perp\mathbf{p}_\perp}$-dependence comes from the velocity vectors v^μ. In the computation of $\delta\epsilon$, δu_t, and δu_s, they will be contracted with the eigenvectors u^μ, t^μ, and s^μ in the following ways:

$$\begin{aligned}
u_\mu v^\mu v^\nu u_\nu &= \gamma^2[1 - 2\beta\cos(\phi_{\mathbf{x}_\perp\mathbf{p}_\perp}) + \beta^2\cos^2(\phi_{\mathbf{x}_\perp\mathbf{p}_\perp})],\\
u_\mu v^\mu v^\nu t_\nu &= \gamma^2[\beta - \cos(\phi_{\mathbf{x}_\perp\mathbf{p}_\perp}) - \beta^2\cos(\phi_{\mathbf{x}_\perp\mathbf{p}_\perp}) + \beta\cos^2(\phi_{\mathbf{x}_\perp\mathbf{p}_\perp})],\\
u_\mu v^\mu v^\nu s_\nu &= -\gamma[\sin(\phi_{\mathbf{x}_\perp\mathbf{p}_\perp}) - \beta\cos(\phi_{\mathbf{x}_\perp\mathbf{p}_\perp})\sin(\phi_{\mathbf{x}_\perp\mathbf{p}_\perp})].
\end{aligned} \tag{B14}$$

Taking into account all of the ingredients presented above, we indeed find that we can decompose all terms into integrals of the form in Eqs. (B1)–(B5). We can plug the results into Eqs. (68)–(70) to obtain explicit expressions for the anisotropic corrections $\delta\epsilon$, δu_t, and δu_s:

$$\begin{aligned}\delta\epsilon &= u_\mu \delta T^{(0)\mu\nu} u_\nu \\ &= \delta_n \frac{1}{\tau}\frac{\mathrm{d}E_\perp^{(0)}}{\mathrm{d}\eta}\frac{1}{2\pi R^{n+2}} e^{-\bar{\alpha}\frac{x_\perp^2+\Delta\tau^2}{R^2}} \int \frac{d\phi_{\mathbf{x}_\perp\mathbf{p}_\perp}}{2\pi} e^{2\bar{\alpha}b\cos(\phi_{\mathbf{x}_\perp\mathbf{p}_\perp})}\gamma^2[1-2\beta\cos(\phi_{\mathbf{x}_\perp\mathbf{p}_\perp})+\beta^2\cos^2(\phi_{\mathbf{x}_\perp\mathbf{p}_\perp})] \\ &\quad\times\sum_{j=0}^{n}\binom{n}{j}x_\perp^{n-j}(-\Delta\tau)^j\cos(n\phi_{\mathbf{x}_\perp\mathbf{n}_\perp}+j\phi_{\mathbf{x}_\perp\mathbf{p}_\perp}) \qquad \text{(B15)}\end{aligned}$$

$$= \cos(n\phi_{\mathbf{x}_\perp\mathbf{n}_\perp})\delta_n \frac{1}{\tau}\frac{\mathrm{d}E_\perp^{(0)}}{\mathrm{d}\eta}\frac{1}{\pi R^{n+2}} e^{-\bar{\alpha}\frac{x_\perp^2+\Delta\tau^2}{R^2}}\gamma^2\sum_{j=0}^{n}\binom{n}{j}x_\perp^{n-j}(-\Delta\tau)^j[I_j(2\bar{\alpha}b)-2\beta I_j'(2\bar{\alpha}b)+\beta^2 I_j''(2\bar{\alpha}b)] \qquad \text{(B16)}$$

$$\delta u_t = \frac{u_\mu\delta T^{(0)\mu\nu}t_\nu}{p_t-\epsilon} = \delta_n\frac{1}{\tau}\frac{\mathrm{d}E_\perp^{(0)}}{\mathrm{d}\eta}\frac{1}{\pi R^{n+2}} e^{-\bar{\alpha}\frac{x_\perp^2+\Delta\tau^2}{R^2}}\int\frac{d\phi_{\mathbf{x}_\perp\mathbf{p}_\perp}}{2\pi}e^{2\bar{\alpha}b\cos(\phi_{\mathbf{x}_\perp\mathbf{p}_\perp})}\gamma^2[\beta-\cos(\phi_{\mathbf{x}_\perp\mathbf{p}_\perp}) \qquad \text{(B17)}$$

$$-\beta^2\cos(\phi_{\mathbf{x}_\perp\mathbf{p}_\perp})+\beta\cos^2(\phi_{\mathbf{x}_\perp\mathbf{p}_\perp})]\sum_{j=0}^{n}\binom{n}{j}x_\perp^{n-j}(-\Delta\tau)^j\cos(n\phi_{\mathbf{x}_\perp\mathbf{n}_\perp}+j\phi_{\mathbf{x}_\perp\mathbf{p}_\perp})$$

$$= \cos(n\phi_{\mathbf{x}_\perp\mathbf{n}_\perp})\delta_n\frac{1}{p_t-\epsilon}\frac{1}{\tau}\frac{\mathrm{d}E_\perp^{(0)}}{\mathrm{d}\eta}\frac{1}{\pi R^{n+2}}e^{-\bar{\alpha}\frac{x_\perp^2+\Delta\tau^2}{R^2}}\gamma^2\sum_{j=0}^{n}\binom{n}{j}x_\perp^{n-j}(-\Delta\tau)^j[\beta I_j(2\bar{\alpha}b)-(1+\beta^2)I_j'(2\bar{\alpha}b)+\beta I_j''(2\bar{\alpha}b)] \qquad \text{(B18)}$$

$$\begin{aligned}\delta u_s &= \frac{u_\mu\delta T^{(0)\mu\nu}s_\nu}{p_s-\epsilon} \\ &= \delta_n\frac{1}{\tau}\frac{\mathrm{d}E_\perp^{(0)}}{\mathrm{d}\eta}\frac{1}{\pi R^{n+2}}e^{-\bar{\alpha}\frac{x_\perp^2+\Delta\tau^2}{R^2}}\int\frac{d\phi_{\mathbf{x}_\perp\mathbf{p}_\perp}}{2\pi}e^{2\bar{\alpha}b\cos(\phi_{\mathbf{x}_\perp\mathbf{p}_\perp})}\gamma[\sin(\phi_{\mathbf{x}_\perp\mathbf{p}_\perp})-\beta\cos(\phi_{\mathbf{x}_\perp\mathbf{p}_\perp})\sin\phi_{\mathbf{x}_\perp\mathbf{p}_\perp}] \\ &\quad\times\sum_{j=0}^{n}\binom{n}{j}x_\perp^{n-j}(-\Delta\tau)^j\cos(n\phi_{\mathbf{x}_\perp\mathbf{n}_\perp}+j\phi_{\mathbf{x}_\perp\mathbf{p}_\perp}) \qquad \text{(B19)}\end{aligned}$$

$$\begin{aligned}&= -\sin(n\phi_{\mathbf{x}_\perp\mathbf{n}_\perp})\delta_n\frac{1}{p_s-\epsilon}\frac{1}{\tau}\frac{\mathrm{d}E_\perp^{(0)}}{\mathrm{d}\eta}\frac{1}{\pi R^{n+2}}e^{-\bar{\alpha}\frac{x_\perp^2+\Delta\tau^2}{R^2}}\gamma\sum_{j=0}^{n}\binom{n}{j}x_\perp^{n-j}(-\Delta\tau)^j[I_j'(2\bar{\alpha}b)-I_{j+1}(2\bar{\alpha}b) \\ &\quad-\beta I_j''(2\bar{\alpha}b)+\beta I_{j+1}'(2\bar{\alpha}b)]. \qquad \text{(B20)}\end{aligned}$$

APPENDIX C: DETAILS OF LINEARIZED CALCULATION

As stated in Sec. III E, the linear order corrections to the observables V_{mn} can be computed as a six-dimensional integral of the kernel:

$$V_{mn}^{(1)}(\tau) = \int \mathrm{d}^2p_\perp e^{in\phi_p}p_\perp^m\int_{\tau_0}^{\tau}\mathrm{d}\tau'\int\mathrm{d}^2x_\perp\int\mathrm{d}\eta\tau'\frac{\nu_{\mathrm{eff}}}{(2\pi)^3}C[f^{(0)}](\tau',\mathbf{x}_\perp,\mathbf{p}_\perp,y-\eta), \qquad \text{(C1)}$$

$$C[f^{(0)}] = -p^\mu u_\mu\left(5\frac{\eta}{s}\right)^{-1}T(f^{(0)}-f_{\mathrm{eq}}). \qquad \text{(C2)}$$

We already outlined in that section how this problem can be split into different terms. The moments V_{m0} depend only on the isotropic part, while the moments V_{mn} with $n\neq 0$ vanish in the isotropic case and have to be computed to linear order in the anisotropic perturbations. Additionally, the linear order corrections to the moments split into buildup of equilibrium $V_{mn}^{(1,\mathrm{eq})}$

and decay of the initial condition $V_{mn}^{(1,0)}$ as computed from the corresponding parts of the kernel:

$$C_{\mathrm{eq}}[f^{(0)}] = p^\mu u_\mu \left(5\frac{\eta}{s}\right)^{-1} T f_{\mathrm{eq}}, \tag{C3}$$

$$C_0[f^{(0)}] = -p^\mu u_\mu \left(5\frac{\eta}{s}\right)^{-1} T f^{(0)}. \tag{C4}$$

This section discusses how four of the integrals can be computed analytically for each of these terms. Many of the angular integrations will again take the forms of the integral formulae given in the beginning of Appendix B. We will start with the moments V_{m0} as they are independent of the anisotropic perturbation.

Exact expressions for the local theormodynamic quantities T, u^μ can be computed from the components of $T^{\mu\nu}$ that are discussed in Appendix B according to the formulae derived in Section III D. In terms of $b = \frac{x_\perp \Delta\tau}{R^2}$, they read

$$T = R^{-1}\left(\frac{1}{\pi}\left(\frac{\pi^2}{30}\nu_{\mathrm{eff}}\right)^{-1}\frac{\mathrm{d}E_\perp^{(0)}}{\mathrm{d}\eta}R\right)^{1/4}\left(\frac{R}{\tau}\right)^{1/4} \times \exp\left(-\frac{x_\perp^2+\Delta\tau^2}{4R^2}\right)[I_0(b)-\beta I_0'(b)]^{1/4}, \tag{C5}$$

$$u^\mu = \gamma(1,\beta\hat{\mathbf{x}}_\perp,0), \qquad \gamma = (1-\beta^2)^{-1/2}, \tag{C6}$$

$$\beta = \frac{I_0(b)}{I_1(b)} - \frac{1}{2b} - \sqrt{\left[\frac{I_0(b)}{I_1(b)} - \frac{1}{2b}\right]^2 - 1}. \tag{C7}$$

Looking at the expression for T, it is immediately apparent that its dimensionless constant prefactor together with $(5\frac{\eta}{s})^{-1}$ constitutes a factor of $\hat{\gamma}$ in $C[f^{(0)}]$, as we have predicted in Sec. II B. We can immediately also compute

$$p^\mu u_\mu = \gamma p_\perp[\cosh(y-\eta) - \beta\cos(\phi_{\mathbf{x}_\perp\mathbf{p}_\perp})]. \tag{C8}$$

Reminding also of the form of $f^{(0)}$,

$$f^{(0)}(\tau,\mathbf{x}_\perp,\mathbf{p}_\perp,y-\eta) = \frac{(2\pi)^3}{\nu_{\mathrm{eff}}}\frac{\delta(y-\eta)}{\tau p_\perp}F\left(\frac{Q_s(\mathbf{x}_\perp-\mathbf{v}_\perp\Delta\tau)}{p_\perp}\right), \tag{C9}$$

where Q_s is fixed by the isotropic energy density according to (12), (14), and (38) to be of the form,

$$Q_s(\mathbf{x}_\perp) = Q_{s,0}\exp\left(-\frac{x_\perp^2}{3R^2}\right), \tag{C10}$$

we can compute $V_{mn}^{(1,0)}$ by plugging the above expressions into the integral formula (C1) for the part of the kernel given in (C4). Due to the fact that in both cases we integrate $f^{(0)}$, the integral over $p_\perp$ is analogous to the computation of the zeroth-order moments $V_{m0}^{(0)}$, where

$$V_{m0}^{(0)} = \int \mathrm{d}^2p_\perp p_\perp^m \frac{\mathrm{d}N^{(0)}}{\mathrm{d}^2p_\perp\mathrm{d}y} \tag{C11}$$

$$= 2\pi\int \mathrm{d}^2x_\perp \int \mathrm{d}\eta \int_0^\infty \mathrm{d}p_\perp p_\perp^{m+1}\delta(y-\eta)F\left(\frac{Q_s(\mathbf{x}_\perp-\mathbf{v}_\perp\Delta\tau)}{p_\perp}\right) \tag{C12}$$

$$= 2\pi\int \mathrm{d}^2x_\perp Q_s^{m+2}(\mathbf{x}_\perp)\int_0^\infty \mathrm{d}k k^{m+1}F\left(\frac{1}{k}\right) \tag{C13}$$

$$= 4\pi^2\frac{3R^2}{m+2}Q_{s,0}^{m+2}\int_0^\infty \mathrm{d}k k^{m+1}F\left(\frac{1}{k}\right). \tag{C14}$$

We can therefore express our result for $V_{m0}^{(1,0)}$ in terms of these zeroth-order moments and find

$$V_{m0}^{(1,0)}(\tau) = -V_{m0}^{(0)}\left(5\frac{\eta}{s}\right)^{-1}\frac{m+2}{3R^2}\int_{\tau_0}^\tau \mathrm{d}\tau'\int_0^\infty \mathrm{d}x_\perp x_\perp T\gamma\exp\left[-\frac{(m+2)(\Delta\tau'^2+x_\perp^2)}{3R^2}\right] \times \int_0^{2\pi}\frac{\mathrm{d}\phi_{\mathbf{x}_\perp\mathbf{p}_\perp}}{2\pi}[1-\beta\cos(\phi_{\mathbf{x}_\perp\mathbf{p}_\perp})]\exp\left(\frac{2(m+2)b\cos(\phi_{\mathbf{x}_\perp\mathbf{p}_\perp})}{3}\right) \tag{C15}$$

$$= -V_{m0}^{(0)}\hat{\gamma}\mathcal{P}_m(\tilde{\tau}), \tag{C16}$$

$$\mathcal{P}_m(\tilde{\tau}) = \frac{(m+2)}{3}\int_{\tilde{\tau}_0}^{\tilde{\tau}}\mathrm{d}\tilde{\tau}'\int_0^\infty \mathrm{d}\tilde{x}_\perp\tilde{x}_\perp\tilde{T}\gamma\exp\left[-\frac{(m+2)}{3}(\Delta\tilde{\tau}'^2+\tilde{x}_\perp^2)\right]\left[I_0\left(\frac{2m+4}{3}b\right)-\beta I_0'\left(\frac{2m+4}{3}b\right)\right], \tag{C17}$$

where one has to keep in mind that in the integrand b, β, γ, and T are to be understood as functions of τ' instead of τ. In the last step, the result was rewritten into the tilded coordinates introduced in Sec. II B to make the parametric dependencies more apparent.

For $V_{mn}^{(1,\mathrm{eq})}$ given by Eq. (C1) with the partial kernel (C3), computing the moments of f_{eq} via the $p_\perp$-integration yields

$$V_{m0}^{(1,\mathrm{eq})}(\tau) = \left(5\frac{\eta}{s}\right)^{-1} \frac{\nu_{\mathrm{eff}}}{(2\pi)^2}\Gamma(m+3)\zeta(m+3)\int_{\tau_0}^{\tau}\mathrm{d}\tau'\int_0^\infty \mathrm{d}x_\perp x_\perp \tau' T^{m+4} \tag{C18}$$

$$\times \int_0^{2\pi}\mathrm{d}\phi_{\mathbf{x}_\perp\mathbf{p}_\perp}\int \mathrm{d}\eta\{\gamma[\cosh(y-\eta)-\beta\cos(\phi_{\mathbf{x}_\perp\mathbf{p}_\perp})]\}^{-m-2}$$

$$= \left(5\frac{\eta}{s}\right)^{-1} \frac{\nu_{\mathrm{eff}}}{2\pi^{1/2}}\Gamma(m+3)\zeta(m+3)\frac{\Gamma(\frac{m+2}{2})}{\Gamma(\frac{m+3}{2})}\int_{\tau_0}^{\tau}\mathrm{d}\tau'\int_0^\infty \mathrm{d}x_\perp x_\perp \tau' T^{m+4}\gamma^{-m-2} \tag{C19}$$

$$\times {}_2F_1\left(\frac{m+2}{2},\frac{m+2}{2};1;\beta^2\right)$$

$$= \hat{\gamma}\nu_{\mathrm{eff}}R^{-m}\left(\frac{1}{\pi}\nu_{\mathrm{eff}}^{-1}\frac{\mathrm{d}E_\perp^{(0)}}{\mathrm{d}\eta}R\right)^{(m+3)/4}\mathcal{Q}_m(\tilde{\tau}), \tag{C20}$$

$$\mathcal{Q}_m(\tilde{\tau}) = \left(\frac{\pi^2}{30}\right)^{-(m+3)/4}\frac{1}{2\pi^{1/2}}\Gamma(m+3)\zeta(m+3)\frac{\Gamma(\frac{m+2}{2})}{\Gamma(\frac{m+3}{2})}\int_{\tilde{\tau}_0}^{\tilde{\tau}}\mathrm{d}\tilde{\tau}'\int_0^\infty \mathrm{d}\tilde{x}_\perp\tilde{x}_\perp\tilde{\tau}'\tilde{T}^{m+4}\gamma^{-m-2}$$

$$\times {}_2F_1\left(\frac{m+2}{2},\frac{m+2}{2};1;\beta^2\right). \tag{C21}$$

After absorbing one of the T prefactors into $\hat{\gamma}$, the parametric dependence of $V_{m0}^{(1,\mathrm{eq})}$ is given by (C20). As the basic structure of the integrands is the same, moments with $n \neq 0$ will have the same parametric dependencies except for the additional anisotropy parameter δ_n.

Now to compute the anisotropic corrections $\delta V_{mn}^{(1)}$ for $n \neq 0$, we first need to derive the change $\delta C[f^{(0)}]$ in the kernel,

$$C[f^{(0)}] = -p^\mu u_\mu\left(5\frac{\eta}{s}\right)^{-1}T(f_{\mathrm{eq}}-f^{(0)}), \tag{C22}$$

due to the anisotropies, so we can plug it into (C1). $C[f^{(0)}]$ depends on three quantities that receive anisotropic corrections: $f^{(0)}$, T, and u^μ. Linearization in the corrections will yield three different contributions. Separating the terms proportional to $f^{(0)}$ from those proportional to f_{eq}, we can split the kernel into the following two parts:

$$\delta C_0[f^{(0)}] = -\left(5\frac{\eta}{s}\right)^{-1}p_\mu(u^\mu T\delta f^{(0)} + u^\mu\delta T f^{(0)} + \delta u^\mu T f^{(0)}) \tag{C23}$$

$$\delta C_{\mathrm{eq}}[f^{(0)}] = \left(5\frac{\eta}{s}\right)^{-1}p_\mu\left[(u^\mu\delta T+\delta u^\mu T)f_{\mathrm{eq}}\left(\frac{p_\nu u^\nu}{T}\right)+(-u^\mu\delta T+\delta u^\mu T)\frac{p_\rho u^\rho}{T}f'_{\mathrm{eq}}\left(\frac{p_\nu u^\nu}{T}\right)\right]. \tag{C24}$$

We can compute the anisotropic contributions to thermodynamic quantities that show up in the kernel from the results for $\delta\epsilon$, δu_t, and δu_s given in Eqs. (B17)–(B19). The change in temperature δT can be computed by linearizing the equation of state $T = (\frac{\pi^2}{30}\nu_{\mathrm{eff}})^{-1/4}\epsilon^{-1/4}$ in $\delta\epsilon$, and the contraction $\delta u_\mu p^\mu$ can be expressed in terms of δu_t and δu_s.

$$\delta T = \frac{1}{4}\left(\frac{\pi^2}{30}\nu_{\mathrm{eff}}\right)^{-1/4}\epsilon^{-3/4}\delta\epsilon = \frac{1}{4}\left(\frac{\pi^2}{30}\nu_{\mathrm{eff}}\right)^{-1}T^{-3}\delta\epsilon, \tag{C25}$$

$$p^\mu\delta u_\mu = p^\mu(\delta u_t t_\mu + \delta u_s s_\mu) = \delta u_t p_\perp\gamma[\beta\cosh(y-\eta)-\cos(\phi_{\mathbf{x}_\perp\mathbf{p}_\perp})] - \delta u_s p_\perp\sin(\phi_{\mathbf{x}_\perp\mathbf{p}_\perp}). \tag{C26}$$

The only anisotropic quantity that we still need to derive is the form of the perturbation $\delta f^{(0)}$ due to the energy density perturbation $\delta\epsilon$. Given that

$$f^{(0)}(\tau, \mathbf{x}_\perp, \mathbf{p}_\perp, y-\eta) = \frac{(2\pi)^3}{\nu_{\text{eff}}} \frac{\delta(y-\eta)}{\tau p_\perp} F\left(\frac{Q_s(\mathbf{x}_\perp - \Delta\tau)}{p_\perp}\right), \tag{C27}$$

the change in f is due to the change in Q_s, which is directly related to ϵ. More specifically,

$$\delta f(\tau, \mathbf{x}_\perp, \mathbf{p}_\perp, y-\eta) = \frac{(2\pi)^3}{\nu_{\text{eff}}} \frac{\delta(y-\eta)}{\tau p_\perp} \frac{\delta Q_s(\mathbf{x}_\perp - \Delta\tau\mathbf{v}_\perp)}{p_\perp} F'\left(\frac{Q_s(\mathbf{x}_\perp - \Delta\tau\mathbf{v}_\perp)}{p_\perp}\right), \tag{C28}$$

where

$$\delta Q_s(\mathbf{x}_\perp) = \frac{1}{3} Q_s(\mathbf{x}_\perp) \frac{\delta\epsilon(\tau_0, \mathbf{x}_\perp)}{\epsilon(\tau_0, x_\perp)} = \frac{1}{3} Q_s(\mathbf{x}_\perp) \delta_n \exp\left(-\alpha \frac{x_\perp^2}{R^2}\right) \left(\frac{x_\perp}{R}\right)^n \cos(n\phi_{\mathbf{x}_\perp \mathbf{n}_\perp}). \tag{C29}$$

Evaluating δQ_s at $\mathbf{x}_\perp - \Delta\tau\mathbf{v}_\perp$ will thus yield as a factor the free-streamed version of $x_\perp^n \cos(n\phi_{\mathbf{x}_\perp \mathbf{n}_\perp})$ that was computed in Appendix A.

We now want to compute the moments $V_{mn}^{(1,0)}$ for $n \neq 0$ by computing the integrals in Eq. (C1) for the part of the kernel perturbation given in Eq. (C23). As in the isotropic case, we can simplify the integral expression by identifying $V_{m0}^{(0)}$. This holds true also for the term containing $\delta f^{(0)}$ instead of $f^{(0)}$, since

$$\int \mathrm{d}p_\perp p_\perp^m Q_s(\mathbf{x}_\perp - \mathbf{v}_\perp \Delta\tau) F'\left(\frac{Q_s(\mathbf{x}_\perp - \mathbf{v}_\perp \Delta\tau)}{p_\perp}\right) = (m+2) \int \mathrm{d}p_\perp p_\perp^{m+1} F\left(\frac{Q_s(\mathbf{x}_\perp - \mathbf{v}_\perp \Delta\tau)}{p_\perp}\right). \tag{C30}$$

The angular integrals are of the same type as the ones in Appendix B; however, each of the three perturbations has a slightly different angular dependence, so we will discuss them one by one. The δf-term is proportional to

$$\int \mathrm{d}\phi_{\mathbf{p}_\perp \mathbf{n}_\perp} \int \mathrm{d}\phi_{\mathbf{x}_\perp \mathbf{p}_\perp} e^{in\phi_{\mathbf{p}_\perp \mathbf{n}_\perp}} e^{2(\frac{m+2}{3}+\alpha) b \cos(\phi_{\mathbf{x}_\perp \mathbf{p}_\perp})} (1 - \beta\cos(\phi_{\mathbf{x}_\perp \mathbf{p}_\perp})) \sum_{j=0}^{n} \binom{n}{j} x_\perp^{n-j} (-\Delta\tau)^j \cos(n\phi_{\mathbf{x}_\perp \mathbf{n}_\perp} + j\phi_{\mathbf{x}_\perp \mathbf{p}_\perp}) \tag{C31}$$

$$= 2\pi \int \mathrm{d}\phi_{\mathbf{p}_\perp \mathbf{n}_\perp} e^{in\phi_{\mathbf{x}_\perp \mathbf{p}_\perp}} \cos(n\phi_{\mathbf{p}_\perp \mathbf{n}_\perp}) \sum_{j=0}^{n} \binom{n}{j} x_\perp^{n-j} (-\Delta\tau)^j \left[I_j\left(\left(\frac{m+2}{3}+\alpha\right) b\right) - \beta I_j'\left(\left(\frac{m+2}{3}+\alpha\right) b\right)\right] \tag{C32}$$

$$= 2\pi^2 \sum_{j=0}^{n} \binom{n}{j} x_\perp^{n-j} (-\Delta\tau)^j \left[I_j\left(\left(\frac{m+2}{3}+\alpha\right) b\right) - \beta I_j'\left(\left(\frac{m+2}{3}+\alpha\right) b\right)\right]. \tag{C33}$$

The δT-perturbation contains via $\delta\epsilon$ a factor of $\cos(n\phi_{\mathbf{x}_\perp \mathbf{n}_\perp}) = \cos(n\phi_{\mathbf{p}_\perp \mathbf{n}_\perp}) \cos(n\phi_{\mathbf{x}_\perp \mathbf{p}_\perp}) - \sin(n\phi_{\mathbf{p}_\perp \mathbf{n}_\perp}) \sin(n\phi_{\mathbf{x}_\perp \mathbf{p}_\perp})$. The term that is odd in $\phi_{\mathbf{x}_\perp \mathbf{p}_\perp}$ will vanish, while the other integrates to

$$\int \mathrm{d}\phi_{\mathbf{p}_\perp \mathbf{n}_\perp} \int \mathrm{d}\phi_{\mathbf{x}_\perp \mathbf{p}_\perp} e^{in\phi_{\mathbf{p}_\perp \mathbf{n}_\perp}} e^{2\frac{m+2}{3} b \cos(\phi_{\mathbf{x}_\perp \mathbf{p}_\perp})} [1 - \beta\cos(\phi_{\mathbf{x}_\perp \mathbf{p}_\perp})] \cos(n\phi_{\mathbf{x}_\perp \mathbf{n}_\perp}) \tag{C34}$$

$$= 2\pi \int \mathrm{d}\phi_{\mathbf{p}_\perp \mathbf{n}_\perp} e^{in\phi_{\mathbf{x}_\perp \mathbf{p}_\perp}} \cos(n\phi_{\mathbf{p}_\perp \mathbf{n}_\perp}) \left[I_n\left(\frac{m+2}{3} b\right) - \beta I_n'\left(\frac{m+2}{3} b\right)\right] \tag{C35}$$

$$= 2\pi^2 \left[I_n\left(\frac{m+2}{3} b\right) - \beta I_n'\left(\frac{m+2}{3} b\right)\right]. \tag{C36}$$

Lastly, the δu^μ-perturbation is of the form $\delta u_t \gamma[\beta - \cos(\phi_{\mathbf{x}_\perp \mathbf{p}_\perp})] - \delta u_s \sin(\phi_{\mathbf{x}_\perp \mathbf{p}_\perp})$. The term containing $\delta u_t \propto \cos(n\phi_{\mathbf{x}_\perp \mathbf{n}_\perp})$ behaves exactly like before:

$$\int \mathrm{d}\phi_{\mathbf{p}_\perp\mathbf{n}_\perp} e^{in\phi_{\mathbf{p}_\perp\mathbf{n}_\perp}} \int \mathrm{d}\phi_{\mathbf{x}_\perp\mathbf{p}_\perp} e^{2\frac{m+2}{3}b\cos(\phi_{\mathbf{x}_\perp\mathbf{p}_\perp})}[\beta - \cos(\phi_{\mathbf{x}_\perp\mathbf{p}_\perp})]\cos(n\phi_{\mathbf{x}_\perp\mathbf{n}_\perp}) \tag{C37}$$

$$= 2\pi^2\left[\beta I_n\left(\frac{m+2}{3}b\right) - I_n'\left(\frac{m+2}{3}b\right)\right], \tag{C38}$$

while the other term contains a factor of $-\sin(\phi_{\mathbf{x}_\perp\mathbf{p}_\perp})\delta u_s$, which has the total angular dependence $-\sin(\phi_{\mathbf{x}_\perp\mathbf{p}_\perp})\sin(n\phi_{\mathbf{x}_\perp\mathbf{n}_\perp}) = -\sin(\phi_{\mathbf{x}_\perp\mathbf{p}_\perp})[\cos(n\phi_{\mathbf{p}_\perp\mathbf{n}_\perp})\sin(n\phi_{\mathbf{x}_\perp\mathbf{p}_\perp}) + \sin(n\phi_{\mathbf{p}_\perp\mathbf{n}_\perp})\cos(n\phi_{\mathbf{x}_\perp\mathbf{p}_\perp})]$, so in angular integration, the $\phi_{\mathbf{x}_\perp\mathbf{p}_\perp}$-even part becomes

$$\int \mathrm{d}\phi_{\mathbf{p}_\perp\mathbf{n}_\perp} e^{in\phi_{\mathbf{p}_\perp\mathbf{n}_\perp}} \int \mathrm{d}\phi_{\mathbf{x}_\perp\mathbf{p}_\perp} e^{2\frac{m+2}{3}b\cos(\phi_{\mathbf{x}_\perp\mathbf{p}_\perp})}(-\sin(\phi_{\mathbf{x}_\perp\mathbf{p}_\perp}))\sin(n\phi_{\mathbf{x}_\perp\mathbf{n}_\perp}) \tag{C39}$$

$$= -2\pi^2\left[\beta I_n'\left(\frac{m+2}{3}b\right) - I_{n+1}\left(\frac{m+2}{3}b\right)\right]. \tag{C40}$$

Putting all of this together, we can find the 2D integral expression for $\delta V_{mn}^{(1,0)}$:

$$\delta V_{mn}^{(1,0)} = -V_{m0}^{(0)}\delta_n\hat{\gamma}\mathcal{P}_{mn}(\tilde{\tau}), \tag{C41}$$

$$\begin{aligned}
\mathcal{P}_{mn}(\tilde{\tau}) = {} & \frac{m+3}{6}\int_{\tilde{\tau}_0}^{\tilde{\tau}}\mathrm{d}\tilde{\tau}'\int_0^\infty \mathrm{d}\tilde{x}_\perp\tilde{x}_\perp\gamma\tilde{T}\exp\left[-\left(\frac{m+2}{3}+\alpha\right)(\tilde{x}_\perp^2+\Delta\tilde{\tau}'^2)\right] \\
& \times\sum_{j=0}^{n}\binom{n}{j}\tilde{x}_\perp^{n-j}(-\Delta\tilde{\tau}')^j\left\{\frac{m+2}{3}\left[I_j\left(\left(\frac{m+2}{3}+\alpha\right)b\right) - \beta I_j'\left(\left(\frac{m+2}{3}+\alpha\right)b\right)\right]\right. \\
& + \frac{1}{4}\frac{1}{\tilde{\tau}'}\gamma^2\tilde{T}^{-4}\left[I_n\left(\frac{m+2}{3}b\right) - \beta I_n'\left(\frac{m+2}{3}b\right)\right][I_j(2\bar{\alpha}b) - 2\beta I_j'(2\bar{\alpha}b) + \beta^2 I_j''(2\bar{\alpha}b)] \\
& + \left\{\gamma^2\left[\left(2\beta+\frac{1}{2b}\right)I_1(2b) - 2I_0(2b)\right]^{-1}[\beta I_j(2\bar{\alpha}b) - (1+\beta^2)I_j'(2\bar{\alpha}b) + \beta I_j''(2\bar{\alpha}b)]\right. \\
& \times\left[\beta I_n\left(\frac{m+2}{3}b\right) - I_n'\left(\frac{m+2}{3}b\right)\right] - \left[\left(\beta-\frac{1}{2b}\right)I_1(2b) - I_0(2b)\right]^{-1} \\
& \left.\left.\times[I_j'(2\bar{\alpha}b) - I_{j+1}(2\bar{\alpha}b) - \beta I_j''(2\bar{\alpha}b) + \beta I_{j+1}'(2\bar{\alpha}b)]\left[\beta I_n'\left(\frac{m+2}{3}b\right) - I_{n+1}\left(\frac{m+2}{3}b\right)\right]\right\}\right\}.
\end{aligned} \tag{C42}$$

Next, we will compute $\delta V_{mn}^{(1,\mathrm{eq})}$ by plugging (C24) into (C1). Again, the most straightforward integration is the one over $p_\perp$, which equates to taking moments of f_{eq}. Terms containing f_{eq}' can be cast into the same form as the others by partial integration, which yields

$$\int \mathrm{d}p_\perp p_\perp^{m+2}\frac{p_\mu u^\mu}{T}f_{\mathrm{eq}}'\left(\frac{p_\nu u^\nu}{T}\right) = -(m+3)\int \mathrm{d}p_\perp p_\perp^{m+2}f_{\mathrm{eq}}\left(\frac{p_\nu u^\nu}{T}\right). \tag{C43}$$

To compute the angular integrals, as in the computation of $\delta V_{mn}^{(1,0)}$, we can rewrite the $\phi_{\mathbf{x}_\perp\mathbf{n}_\perp}$-dependence of $\delta\epsilon$, δu_t, and δu_s into a dependence on $\phi_{\mathbf{p}_\perp\mathbf{n}_\perp}$ and $\phi_{\mathbf{x}_\perp\mathbf{p}_\perp}$, which makes the $\phi_{\mathbf{p}_\perp\mathbf{n}_\perp}$-integration trivial. However, the next step will be the trickiest one of this entire section, as the integrals over $\phi_{\mathbf{x}_\perp\mathbf{p}_\perp}$ and η are highly nontrivial. The integrals that need to be computed for the different anisotropic correction terms include:

$$\int \mathrm{d}\eta\int \mathrm{d}\phi_{\mathbf{x}_\perp\mathbf{p}_\perp}\left(\frac{p_\mu u^\mu}{p_\perp}\right)^{-m-2}\delta\epsilon, \tag{C44}$$

$$\int \mathrm{d}\eta\int \mathrm{d}\phi_{\mathbf{x}_\perp\mathbf{p}_\perp}\left(\frac{p_\mu u^\mu}{p_\perp}\right)^{-m-3}\delta u_t[\beta\cosh(y-\eta) - \cos(\phi_{\mathbf{x}_\perp\mathbf{p}_\perp})], \tag{C45}$$

$$\int \mathrm{d}\eta \int \mathrm{d}\phi_{\mathbf{x}_\perp \mathbf{p}_\perp} \left(\frac{p_\mu u^\mu}{p_\perp}\right)^{-m-3} \delta u_s \sin(\phi_{\mathbf{x}_\perp \mathbf{p}_\perp}). \tag{C46}$$

Getting rid of all prefactors that do not depend on the integration variables, this amounts to computing the following integrals:

$$G_\epsilon(n,m,\beta) = \int \mathrm{d}\eta \int \mathrm{d}\phi_{\mathbf{x}_\perp \mathbf{p}_\perp} [\cosh(y-\eta) - \beta\cos(\phi_{\mathbf{x}_\perp \mathbf{p}_\perp})]^{-m-2} \cos(n\phi_{\mathbf{x}_\perp \mathbf{p}_\perp}), \tag{C47}$$

$$G_{u_t}(n,m,\beta) = \int \mathrm{d}\eta \int \mathrm{d}\phi_{\mathbf{x}_\perp \mathbf{p}_\perp} [\cosh(y-\eta) - \beta\cos(\phi_{\mathbf{x}_\perp \mathbf{p}_\perp})]^{-m-3} [\beta\cosh(y-\eta) - \cos(\phi_{\mathbf{x}_\perp \mathbf{p}_\perp})] \cos(n\phi_{\mathbf{x}_\perp \mathbf{p}_\perp}), \tag{C48}$$

$$G_{u_s}(n,m,\beta) = \int \mathrm{d}\eta \int \mathrm{d}\phi_{\mathbf{x}_\perp \mathbf{p}_\perp}, [\cosh(y-\eta) - \beta\cos(\phi_{\mathbf{x}_\perp \mathbf{p}_\perp})]^{-m-3} \sin(\phi_{\mathbf{x}_\perp \mathbf{p}_\perp}) \sin(n\phi_{\mathbf{x}_\perp \mathbf{p}_\perp}). \tag{C49}$$

We have defined these integrals as the functions $G_X(n,m,\beta)$ to abbreviate the notation of our results. To compute them, we rewrite again $\sin(n\phi_{\mathbf{x}_\perp \mathbf{p}_\perp})$ and $\cos(n\phi_{\mathbf{x}_\perp \mathbf{p}_\perp})$ into Chebyshev polynomials as we did in Appendix A. The polynomial expression for $\sin(n\phi_{\mathbf{x}_\perp \mathbf{p}_\perp})$ contains another factor of $\sin(\phi_{\mathbf{x}_\perp \mathbf{p}_\perp})$, which combines with the sine already present in (C49) to give $1-\cos^2(\phi_{\mathbf{x}_\perp \mathbf{p}_\perp})$. Thus, only different powers of $\cos(\phi_{\mathbf{x}_\perp \mathbf{p}_\perp})$ without any sines occur in the integrand, which can be integrated analytically as follows:

$$\int \mathrm{d}\eta \int \mathrm{d}\phi_{\mathbf{x}_\perp \mathbf{p}_\perp} [\cosh(y-\eta) - \beta\cos(\phi_{\mathbf{x}_\perp \mathbf{p}_\perp})]^{-m-2} \cos^l(\phi_{\mathbf{x}_\perp \mathbf{p}_\perp}) \tag{C50}$$

$$= 4\int_1^\infty \mathrm{d}x \int_{-1}^1 \mathrm{d}y \frac{[x-\beta y)]^{-m-2} y^l}{\sqrt{1+x^2}\sqrt{1-y^2}} \tag{C51}$$

$$= \begin{cases} \frac{2\pi\Gamma(\frac{m+2}{2})\Gamma(\frac{l+1}{2})}{\Gamma(\frac{m+3}{2})\Gamma(\frac{l+2}{2})} {}_3F_2(\frac{m+2}{2}, \frac{m+2}{2}, \frac{l+1}{2}; \frac{1}{2}, \frac{l+2}{2}; \beta^2) & ,l \text{ even} \\ \frac{4\pi\beta\Gamma(\frac{m+3}{2})\Gamma(\frac{l+2}{2})}{\Gamma(\frac{m+2}{2})\Gamma(\frac{l+3}{2})} {}_3F_2(\frac{m+3}{2}, \frac{m+3}{2}, \frac{l+2}{2}; \frac{3}{2}, \frac{l+3}{2}; \beta^2) & ,l \text{ odd} \end{cases}, \tag{C52}$$

$$\int \mathrm{d}\eta \int \mathrm{d}\phi_{\mathbf{x}_\perp \mathbf{p}_\perp} [\cosh(y-\eta) - \beta\cos(\phi_{\mathbf{x}_\perp \mathbf{p}_\perp})]^{-m-3} \cos^l(\phi_{\mathbf{x}_\perp \mathbf{p}_\perp}) \cosh(y-\eta) \tag{C53}$$

$$= 4\int_1^\infty \mathrm{d}x \int_{-1}^1 \mathrm{d}y \frac{[x-\beta y)]^{-m-3} y^l x}{\sqrt{1+x^2}\sqrt{1-y^2}} \tag{C54}$$

$$= \begin{cases} \frac{2\pi\Gamma(\frac{m+2}{2})\Gamma(\frac{l+1}{2})}{\Gamma(\frac{m+3}{2})\Gamma(\frac{l+2}{2})} {}_3F_2(\frac{m+2}{2}, \frac{m+4}{2}, \frac{l+1}{2}; \frac{1}{2}, \frac{l+2}{2}; \beta^2) & ,l \text{ even} \\ \frac{4\pi\beta\Gamma(\frac{m+5}{2})\Gamma(\frac{l+2}{2})}{\Gamma(\frac{m+4}{2})\Gamma(\frac{l+3}{2})} {}_3F_2(\frac{m+3}{2}, \frac{m+5}{2}, \frac{l+2}{2}; \frac{3}{2}, \frac{l+3}{2}; \beta^2) & ,l \text{ odd} \end{cases}. \tag{C55}$$

To simplify these expressions, we can make use of the following property of the Γ-function:

$$\frac{\Gamma(n+\frac{1}{2})}{\Gamma(n+1)} = \frac{(2n)!}{4^n (n!)^2}\sqrt{\pi}. \tag{C56}$$

Then one finds for the integrals (C47)–(C49):

$$G_\epsilon(n,m,\beta) = \int \mathrm{d}\eta \int \mathrm{d}\phi [\cosh(y-\eta) - \beta\cos(\phi)]^{-m-2} \frac{n}{2} \sum_{k=0}^{\lfloor \frac{n}{2} \rfloor} (-1)^k \frac{(n-k-1)!}{(n-2k)!k!} 2^{n-2k} \cos^{n-2k}(\phi)$$
$$= \pi^{3/2} n \begin{cases} \frac{\Gamma(\frac{m+2}{2})}{\Gamma(\frac{m+3}{2})} \sum_{k=0}^{\lfloor \frac{n}{2} \rfloor} (-1)^k \frac{(n-k-1)!}{(\frac{n-2k}{2}!)^2 k!} {}_3F_2(\frac{m+2}{2}, \frac{m+2}{2}, \frac{n-2k+1}{2}; \frac{1}{2}, \frac{n-2k+2}{2}; \beta^2) & , n \text{ even} \\ \beta \frac{\Gamma(\frac{m+2}{2})}{\Gamma(\frac{m+3}{2})} \sum_{k=0}^{\lfloor \frac{n}{2} \rfloor} (-1)^k \frac{(n-k-1)!}{(\frac{n-2k-1}{2}!)^2 k!} {}_3F_2(\frac{m+3}{2}, \frac{m+3}{2}, \frac{n-2k+2}{2}; \frac{3}{2}, \frac{n-2k+3}{2}; \beta^2) & , n \text{ odd} \end{cases}, \tag{C57}$$

$$G_{u_t}(n,m,\beta) = \int \mathrm{d}\eta \int \mathrm{d}\phi [\cosh(y-\eta) - \beta\cos(\phi)]^{-m-3} \sum_{k=0}^{\lfloor \frac{n-1}{2} \rfloor} (-1)^k \binom{n-k-1}{k} 2^{n-2k-1} [\cos^{n-2k-1}(\phi) - \cos^{n-2k+1}(\phi)]$$
$$= 2\pi^{3/2} \begin{cases} \frac{\Gamma(\frac{m+3}{2})}{\Gamma(\frac{m+4}{2})} \sum_{k=0}^{\lfloor \frac{n-1}{2} \rfloor} (-1)^k \frac{(n-k-1)!}{(\frac{n-2k-1}{2}!)^2 k!} \big[{}_3F_2(\frac{m+3}{2}, \frac{m+3}{2}, \frac{n-2k}{2}; \frac{1}{2}, \frac{n-2k+1}{2}; \beta^2) \\ + \frac{n-2k}{n-2k+1} {}_3F_2(\frac{m+3}{2}, \frac{m+3}{2}, \frac{n-2k+2}{2}; \frac{1}{2}, \frac{n-2k+3}{2}; \beta^2) \big] & , n \text{ odd} \\ \beta \frac{\Gamma(\frac{m+4}{2})}{\Gamma(\frac{m+3}{2})} \sum_{k=0}^{\lfloor \frac{n-1}{2} \rfloor} (-1)^k \frac{(n-k-1)!}{(\frac{n-2k-2}{2}!)^2 k!} \big[{}_3F_2(\frac{m+4}{2}, \frac{m+4}{2}, \frac{n-2k+1}{2}; \frac{3}{2}, \frac{n-2k+2}{2}; \beta^2) \\ + \frac{n-2k+1}{n-2k+2} {}_3F_2(\frac{m+4}{2}, \frac{m+4}{2}, \frac{n-2k+3}{2}; \frac{3}{2}, \frac{n-2k+4}{2}; \beta^2) \big] & , n \text{ even} \end{cases}, \tag{C58}$$

$$G_{u_s}(n,m,\beta)$$
$$= \int \mathrm{d}\eta \int \mathrm{d}\phi [\cosh(y-\eta) - \beta\cos(\phi)]^{-m-3} \frac{n}{2} \sum_{k=0}^{\lfloor \frac{n}{2} \rfloor} (-1)^k \frac{(n-k-1)!}{(n-2k)!k!} 2^{n-2k} [\beta\cos^{n-2k}(\phi)\cosh(y-\eta) - \cos^{n-2k+1}(\phi)]$$
$$= \pi^{3/2} n \begin{cases} \sum_{k=0}^{\lfloor \frac{n}{2} \rfloor} (-1)^k \frac{(n-k-1)!}{(\frac{n-2k}{2}!)^2 k!} \Big[\beta \frac{\Gamma(\frac{m+2}{2})}{\Gamma(\frac{m+3}{2})} {}_3F_2(\frac{m+2}{2}, \frac{m+4}{2}, \frac{n-2k+1}{2}; \frac{1}{2}, \frac{n-2k+2}{2}; \beta^2) \\ -2\beta \frac{\Gamma(\frac{m+4}{2})}{\Gamma(\frac{m+3}{2})} \frac{n-2k+1}{n-2k+2} {}_3F_2(\frac{m+4}{2}, \frac{m+4}{2}, \frac{n-2k+3}{2}; \frac{3}{2}, \frac{n-2k+4}{2}; \beta^2) \Big] & , n \text{ even} \\ \sum_{k=0}^{\lfloor \frac{n}{2} \rfloor} (-1)^k \frac{(n-k-1)!}{(\frac{n-2k}{2}!)^2 k!} \Big[\beta^2 \frac{\Gamma(\frac{m+5}{2})}{\Gamma(\frac{m+4}{2})} {}_3F_2(\frac{m+3}{2}, \frac{m+5}{2}, \frac{n-2k+2}{2}; \frac{3}{2}, \frac{n-2k+3}{2}; \beta^2) \\ -\beta \frac{\Gamma(\frac{m+3}{2})}{2\Gamma(\frac{m+4}{2})} {}_3F_2(\frac{m+3}{2}, \frac{m+3}{2}, \frac{n-2k+2}{2}; \frac{1}{2}, \frac{n-2k+3}{2}; \beta^2) \Big] & , n \text{ odd} \end{cases}. \tag{C59}$$

The final step to computing the total expression for $\delta V_{mn}^{(1,\mathrm{eq})}$ is a bookkeeping task of combining all the above integration steps, at the end of which, one acquires

$$\delta V_{mn}^{(1,\mathrm{eq})} = \hat{\gamma}\delta_n \nu_{\mathrm{eff}} R^{-m} \left(\frac{1}{\pi} \nu_{\mathrm{eff}}^{-1} \frac{\mathrm{d}E_\perp^{(0)}}{\mathrm{d}\eta} R \right)^{(m+3)/4} \mathcal{Q}_{mn}(\tilde{\tau}), \tag{C60}$$

$$\mathcal{Q}_{mn}(\tilde{\tau}) = \left(\frac{\pi^2}{30} \right)^{-(m+3)/4} \frac{1}{8\pi^2} \zeta(m+3) \int_{\tilde{\tau}_0}^{\tilde{\tau}} \mathrm{d}\tilde{\tau}' \int_0^\infty \mathrm{d}\tilde{x}_\perp \tilde{x}_\perp \gamma^{-m-2} \tilde{T}^m \exp\left[-\bar{\alpha}(\tilde{x}_\perp^2 + \Delta\tilde{\tau}'^2) \right]$$
$$\times \sum_{j=0}^{n} \binom{n}{j} \tilde{x}_\perp^{n-j} (-\Delta\tilde{\tau}')^j \Big\{ \frac{1}{4} [\Gamma(m+3) + \Gamma(m+4)] \gamma^2 [I_j(2\bar{\alpha}b) - 2\beta I_j'(2\bar{\alpha}b) + \beta^2 I_j''(2\bar{\alpha}b)] G_\epsilon(n,m,\beta)$$
$$+ [\Gamma(m+3) - \Gamma(m+4)] \tilde{\tau}\tilde{T}^4 \Big\{ \gamma^2 \left[\left(2\beta + \frac{1}{2b} \right) I_1(2b) - 2I_0(2b) \right]^{-1}$$
$$\times [\beta I_j(2\bar{\alpha}b) - (1+\beta^2) I_j'(2\bar{\alpha}b) + \beta I_j''(2\bar{\alpha}b)] G_{u_t}(n,m,\beta)$$
$$- \left[\left(\beta - \frac{1}{2b} \right) I_1(2b) - I_0(2b) \right]^{-1} [I_j'(2\bar{\alpha}b) - I_{j+1}(2\bar{\alpha}b) - \beta I_j''(2\bar{\alpha}b) + \beta I_{j+1}'(2\bar{\alpha}b)] G_{u_s}(n,m,\beta) \Big\} \Big\}. \tag{C61}$$

APPENDIX D: EQUILIBRIUM MOMENTS OF THE NUMERICAL SETUP

In this appendix, the equilibrium moments E_l^m emerging in the time evolution equations for the moments C_l^m as derived in Sec. IV A are computed. Since taking the integral $\int \mathrm{d}p^\tau (p^\tau)^3$ of the equilibrium distribution will yield the energy density, the expression simplifies in spherical coordinates:

$$E_l^m = \nu_{\mathrm{eff}} \int \frac{\mathrm{d}^2 p_\perp}{(2\pi)^2} \int \frac{\mathrm{d}p_\eta}{2\pi} Y_l^m(\theta_p, \phi_p) p^\mu u_\mu f_{\mathrm{eq}} \tag{D1}$$

$$= \nu_{\mathrm{eff}} \int_0^\infty \mathrm{d}p^\tau (p^\tau)^3 \int_0^{2\pi} \frac{\mathrm{d}\phi_p}{2\pi} \int \frac{\mathrm{d}\cos\theta_p}{2} Y_l^m(\theta_p, \phi_p) \frac{1}{2\pi^2} v^\mu u_\mu f_{\mathrm{eq}} \left(\frac{p^\mu u_\mu}{T} \right) \tag{D2}$$

$$= \tau\epsilon \int_0^{2\pi} \frac{\mathrm{d}\phi_p}{2\pi} \int \frac{\mathrm{d}\cos\theta_p}{2} Y_l^m(\theta_p, \phi_p) (v^\mu u_\mu)^{-3}. \tag{D3}$$

In this calculation, we have defined $v^\mu = p^\mu / p^\tau$. To compute the angular integral, we write

$$v^\mu u_\mu = \gamma(1 - \vec{\beta} \cdot \vec{v}) = \gamma(1 - \beta \cos\theta_{\mathrm{up}}), \tag{D4}$$

and express the spherical harmonics in a rotated coordinate system, thus writing

$$Y_l^m(\theta_p, \phi_p) = \sum_{m'=-l}^{l} (D^l_{mm'})^* Y_l^{m'}(\theta_{\mathrm{up}}, \phi_{\mathrm{up}}), \tag{D5}$$

where the Wigner D-matrix depends on the angles involved in the rotation from $(\theta_{\mathrm{up}}, \phi_{\mathrm{up}})$ to (θ_p, ϕ_p). In these coordinates, the ϕ_{up}-integral becomes trivial; thus, only an integral of the Legendre polynomials remains to be computed:

$$\int_0^{2\pi} \frac{\mathrm{d}\phi_{\mathrm{up}}}{2\pi} \int \frac{\mathrm{d}\cos\theta_{\mathrm{up}}}{2} Y_l^{m'}(\theta_{\mathrm{up}}, \phi_{\mathrm{up}}) \gamma^{-3} (1 - \beta\cos\theta_{\mathrm{up}})^{-3} = \delta^{m'0} y_l^0 \int \mathrm{d}x \frac{P_l(x)}{2\gamma^3 (1 - \beta x)^3}. \tag{D6}$$

For the case $m' = 0$, the Wigner D matrix simplifies to

$$(D^l_{m0})^* = \sqrt{\frac{4\pi}{2l+1}} Y_l^m(\theta_{\mathrm{rot}}, \phi_{\mathrm{rot}}). \tag{D7}$$

Since $\vec{u}$ lies in the transverse plane, where its orientation is given by ϕ_u, we can identify the rotation angles to be $\theta_{\mathrm{rot}} = \frac{\pi}{2}$ and $\phi_{\mathrm{rot}} = \phi_u$, which yields

$$E_l^m = \tau\epsilon Y_l^m \left(\frac{\pi}{2}, \phi_u \right) \int_{-1}^{1} \mathrm{d}x \frac{P_l(x)}{2\gamma^3 (1 - \beta x)^3}. \tag{D8}$$

Finally, the remaining integral can be solved analytically:

$$\int_{-1}^{1} \mathrm{d}x \frac{P_l(x)}{2\gamma^3 (1 - \beta x)^3} = 2^{-l-2} \pi^{1/2} \frac{\Gamma(l+3)}{\Gamma(l + \frac{3}{2})} \gamma^{-3} \beta^l {}_2F_1 \left(\frac{l+4}{2}, \frac{l+3}{2}; l + \frac{3}{2}; \beta^2 \right). \tag{D9}$$

APPENDIX E: EARLY AND INTERMEDIATE TIME COOLING BASED ON 0+1-D BJORKEN ATTRACTOR

Below we describe the procedure employed to perform the integration in Eq. (151), which provides the *Bjorken scaling* curve in Fig. 1(a). The main ingredients that we require are the universal functions $\mathcal{E}(\tilde{w})$ and $f_{E_\perp}(\tilde{w})$. These are determined by performing a $0+1$-dimensional simulation (i.e., for a system that is homogeneous with respect to the transverse plane) using the RLB method described in Sec. IV B. The initial time and temperature were set to $\tau_0 = 10^{-4}$ fm and $T_0 = 0.315$ GeV, while $4\pi\eta/s = 1$, giving $\tilde{w}_0 \simeq 1.6 \times 10^{-4}$. The initial distribution was taken to be of Romatschke-Strickland form (126) with anisotropy parameter $\xi_0 = 1000$, corresponding to an initial pressure ratio $\mathcal{P}_L/\mathcal{P}_T \simeq 0.002$. The simulation was ran until $\tau/\tau_0 = 10^{10}$ or $\tilde{w} \simeq 1892$. During the simulation, the energy density and $dE_\perp/d^2\mathbf{x}_\perp d\eta$ are

computed, and the universal functions $\mathcal{E}$ and $f_{E_\perp}$ are obtained using

$$C_\infty \mathcal{E}(\tilde{w}) = \frac{\epsilon(\tilde{w})}{\epsilon_0}\left(\frac{\tau}{\tau_0}\right)^{4/3}\tilde{w}_0^{4/9},$$
$$C_\infty f_{E_\perp}(\tilde{w}) = \frac{\tau_0}{\tau\epsilon_0}\frac{dE}{d^2\mathbf{x}_\perp d\eta}\left(\frac{\tau}{\tau_0}\right)^{4/3}\tilde{w}_0^{4/9}, \quad \text{(E1)}$$

and the results are presented in Fig. 14. For completeness, we provide a comparison with the results for $\mathcal{E}(\tilde{w})$ reported as "Boltzmann RTA" in Fig. 1 of Ref. [90], which are shown using the red dashed line. The $C_\infty^{-1}\tilde{w}^{4/9}$ limit valid at small values of $\tilde{w}$ is shown as the black dotted line.

Next, in order to perform the integrals in Eq. (151), the top end of the integration $\tilde{w}(\tau, \mathbf{x}_\perp = 0)$ must be found by numerically inverting Eq. (152). Considering the range $10^{-5} \leq \tau/R \leq 1$ and $2 \leq \hat{\gamma} \leq 400$, the minimum and maximum values of $\tilde{w}(\tau, \mathbf{x}_\perp = 0)$ encountered are 1.4×10^{-4} and 88, corresponding to $(\tau/R, \hat{\gamma}) = (10^{-5}, 2)$ and (1,400), respectively. In order to avoid "boundary effects" due to our choice of initial conditions, we considered the numerical data only for $\tilde{w} \gtrsim 3.4 \times 10^{-4}$, while for smaller values of $\tilde{w}$, we employed the analytical limits in Eqs. (142) and (143), namely $\mathcal{E}, f_{E_\perp} \simeq C_\infty^{-1}\tilde{w}^{4/9}$.

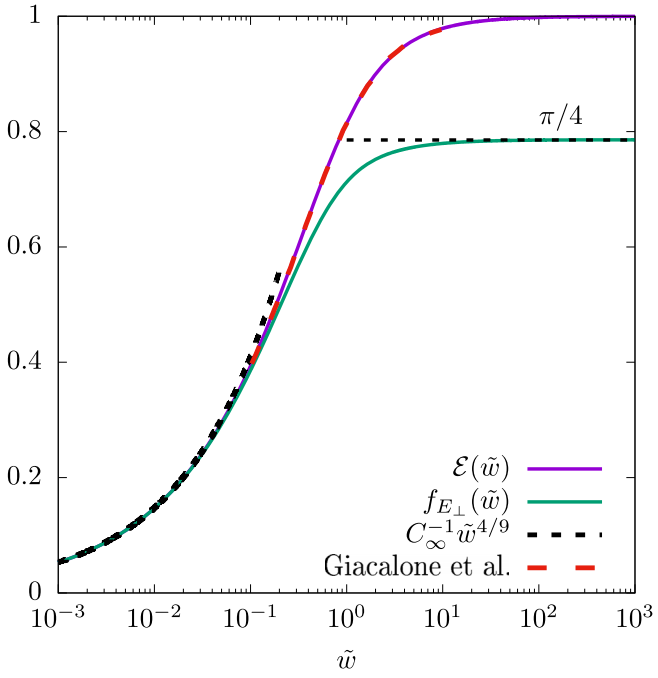

FIG. 14. Universal functions $\mathcal{E}(\tilde{w})$ and $f_{E_\perp}(\tilde{w})$ obtained using the RLB method, represented with respect to the conformal parameter $\tilde{w} = \tau T/(4\pi\eta/s)$ for the $0+1$-D Bjorken flow. The red dashed curve shows the results for the RTA attractor reported in Fig. 1 of Ref. [90].

[1] D. A. Teaney, arXiv:0905.2433.
[2] C. Gale, S. Jeon, and B. Schenke, Int. J. Mod. Phys. A **28**, 1340011 (2013).
[3] M. Luzum and H. Petersen, J. Phys. G **41**, 063102 (2014).
[4] U. Heinz and R. Snellings, Annu. Rev. Nucl. Part. Sci. **63**, 123 (2013).
[5] S. Jeon and U. Heinz, Int. J. Mod. Phys. E **24**, 1530010 (2015).
[6] D. Everett *et al.* (JETSCAPE Collaboration), Phys. Rev. C **103**, 054904 (2021).
[7] G. Nijs, W. van der Schee, U. Gürsoy, and R. Snellings, Phys. Rev. C **103**, 054909 (2021).
[8] F. G. Gardim, G. Giacalone, M. Luzum, and J.-Y. Ollitrault, Nat. Phys. **16**, 615 (2020).
[9] B. Schenke, C. Shen, and P. Tribedy, Phys. Rev. C **102**, 044905 (2020).
[10] P. Bozek, Phys. Rev. C **85**, 014911 (2012).
[11] P. Bozek and W. Broniowski, Phys. Lett. B **718**, 1557 (2013).
[12] P. Bozek and W. Broniowski, Phys. Lett. B **720**, 250 (2013).
[13] P. Bozek and W. Broniowski, Phys. Rev. C **88**, 014903 (2013).
[14] P. Bozek, W. Broniowski, and G. Torrieri, Phys. Rev. Lett. **111**, 172303 (2013).
[15] A. Bzdak, B. Schenke, P. Tribedy, and R. Venugopalan, Phys. Rev. C **87**, 064906 (2013).
[16] G.-Y. Qin and B. Müller, Phys. Rev. C **89**, 044902 (2014).
[17] K. Werner, M. Bleicher, B. Guiot, I. Karpenko, and T. Pierog, Phys. Rev. Lett. **112**, 232301 (2014).
[18] I. Kozlov, M. Luzum, G. Denicol, S. Jeon, and C. Gale, arXiv:1405.3976.
[19] B. Schenke and R. Venugopalan, Phys. Rev. Lett. **113**, 102301 (2014).
[20] P. Romatschke, Eur. Phys. J. C **75**, 305 (2015).
[21] C. Shen, J.-F. Paquet, G. S. Denicol, S. Jeon, and C. Gale, Phys. Rev. C **95**, 014906 (2017).
[22] R. D. Weller and P. Romatschke, Phys. Lett. B **774**, 351 (2017).
[23] H. Mäntysaari, B. Schenke, C. Shen, and P. Tribedy, Phys. Lett. B **772**, 681 (2017).
[24] B. Schenke, C. Shen, and P. Tribedy, Phys. Lett. B **803**, 135322 (2020).
[25] K. Dusling, W. Li, and B. Schenke, Int. J. Mod. Phys. E **25**, 1630002 (2016).
[26] C. Loizides, Nucl. Phys. **A956**, 200 (2016).
[27] J. L. Nagle and W. A. Zajc, Annu. Rev. Nucl. Part. Sci. **68**, 211 (2018).
[28] B. Schenke, Rep. Prog. Phys. **84**, 082301 (2021).

[29] S. Demirci, T. Lappi, and S. Schlichting, Phys. Rev. D **103**, 094025 (2021).
[30] S. Schlichting and D. Teaney, Annu. Rev. Nucl. Part. Sci. **69**, 447 (2019).
[31] J. Berges, M. P. Heller, A. Mazeliauskas, and R. Venugopalan, Rev. Mod. Phys. **93**, 035003 (2021).
[32] B. Schenke, S. Schlichting, and R. Venugopalan, Phys. Lett. B **747**, 76 (2015).
[33] L. McLerran and V. Skokov, Nucl. Phys. **A947**, 142 (2016).
[34] B. Schenke, S. Schlichting, P. Tribedy, and R. Venugopalan, Phys. Rev. Lett. **117**, 162301 (2016).
[35] K. Dusling, M. Mace, and R. Venugopalan, Phys. Rev. Lett. **120**, 042002 (2018).
[36] K. Dusling, M. Mace, and R. Venugopalan, Phys. Rev. D **97**, 016014 (2018).
[37] M. Greif, C. Greiner, B. Schenke, S. Schlichting, and Z. Xu, Phys. Rev. D **96**, 091504 (2017).
[38] M. Mace, V. V. Skokov, P. Tribedy, and R. Venugopalan, Phys. Rev. Lett. **121**, 052301 (2018); **123**, 039901(E) (2019).
[39] M. Mace, V. V. Skokov, P. Tribedy, and R. Venugopalan, Phys. Lett. B **788**, 161 (2019); **799**, 135006(E) (2019).
[40] A. Kovner and V. V. Skokov, Phys. Lett. B **785**, 372 (2018).
[41] M. Greif, C. Greiner, S. Plätzer, B. Schenke, and S. Schlichting, Phys. Rev. D **103**, 054011 (2021).
[42] P. Agostini, T. Altinoluk, and N. Armesto, Eur. Phys. J. C **81**, 760 (2021).
[43] V. A. Abramovsky, E. V. Gedalin, E. G. Gurvich, and O. V. Kancheli, JETP Lett. **47**, 337 (1988), http://www.jetpletters.ru/ps/1093/article_16503.shtml.
[44] A. Ortiz Velasquez, P. Christiansen, E. Cuautle Flores, I. Maldonado Cervantes, and G. Paić, Phys. Rev. Lett. **111**, 042001 (2013).
[45] C. Bierlich, G. Gustafson, and L. Lönnblad, Phys. Lett. B **779**, 58 (2018).
[46] C. Bierlich, S. Chakraborty, G. Gustafson, and L. Lönnblad, J. High Energy Phys. 03 (2021) 270.
[47] U. A. Wiedemann, Proc. Sci. ICHEP2020 (**2021**) 046 [arXiv:2101.01971].
[48] H. Heiselberg and A.-M. Levy, Phys. Rev. C **59**, 2716 (1999).
[49] N. Borghini and C. Gombeaud, Eur. Phys. J. C **71**, 1612 (2011).
[50] P. Romatschke, Eur. Phys. J. C **78**, 636 (2018).
[51] N. Kersting, N. Borghini, and S. Feld, MDPI Proc. **10**, 16 (2019).
[52] A. Kurkela, U. A. Wiedemann, and B. Wu, Eur. Phys. J. C **79**, 965 (2019).
[53] A. Kurkela, U. A. Wiedemann, and B. Wu, Phys. Lett. B **783**, 274 (2018).
[54] N. Borghini, S. Feld, and N. Kersting, Eur. Phys. J. C **78**, 832 (2018).
[55] A. Kurkela, A. Mazeliauskas, and R. Törnkvist, J. High Energy Phys. 11 (2021) 216.
[56] L. He, T. Edmonds, Z.-W. Lin, F. Liu, D. Molnar, and F. Wang, Phys. Lett. B **753**, 506 (2016).
[57] A. Kurkela, S. F. Taghavi, U. A. Wiedemann, and B. Wu, Phys. Lett. B **811**, 135901 (2020).
[58] H. Roch and N. Borghini, Eur. Phys. J. C **81**, 380 (2021).
[59] A. H. Mueller, Phys. Lett. B **475**, 220 (2000).
[60] J. Anderson and H. Witting, Physica (Amsterdam) **74**, 466 (1974).
[61] J. Anderson and H. Witting, Physica (Amsterdam) **74**, 489 (1974).
[62] C. Cercignani and G. M. Kremer, *The Relativistic Boltzmann Equation: Theory and Applications* (Birkhäuser Verlag, Basel, Switzerland, 2002).
[63] L. Rezzolla and O. Zanotti, *Relativistic Hydrodynamics* (Oxford University Press, Oxford, UK, 2013).
[64] G. S. Rocha, G. S. Denicol, and J. Noronha, Phys. Rev. Lett. **127**, 042301 (2021).
[65] F. Gelis, E. Iancu, J. Jalilian-Marian, and R. Venugopalan, Annu. Rev. Nucl. Part. Sci. **60**, 463 (2010).
[66] D. Teaney and L. Yan, Phys. Rev. C **83**, 064904 (2011).
[67] R. S. Bhalerao, M. Luzum, and J.-Y. Ollitrault, Phys. Rev. C **84**, 034910 (2011).
[68] S. Voloshin and Y. Zhang, Z. Phys. C **70**, 665 (1996).
[69] N. Borghini, P. M. Dinh, and J.-Y. Ollitrault, Phys. Rev. C **63**, 054906 (2001).
[70] J.-Y. Ollitrault, Phys. Rev. D **46**, 229 (1992).
[71] H. Song and U. W. Heinz, Phys. Rev. C **77**, 064901 (2008).
[72] I. Karpenko, P. Huovinen, and M. Bleicher, Comput. Phys. Commun. **185**, 3016 (2014).
[73] S. Kamata, M. Martinez, P. Plaschke, S. Ochsenfeld, and S. Schlichting, Phys. Rev. D **102**, 056003 (2020).
[74] G. Guennebaud, B. Jacob *et al.*, Eigen v3, 2010, http://eigen.tuxfamily.org.
[75] P. Romatschke, M. Mendoza, and S. Succi, Phys. Rev. C **84**, 034903 (2011).
[76] V. E. Ambruş and R. Blaga, Phys. Rev. C **98**, 035201 (2018).
[77] S. Succi, *The Lattice Boltzmann Equation: For Complex States of Flowing Matter* (Oxford University Press, Oxford, UK, 2018).
[78] A. Gabbana, D. Simeoni, S. Succi, and R. Tripiccione, Phys. Rep. **863**, 1 (2020).
[79] L. Bazzanini, A. Gabbana, D. Simeoni, S. Succi, and R. Tripiccione, J. Comput. Sci. **51**, 101320 (2021).
[80] A. Kurkela, U. A. Wiedemann, and B. Wu, Eur. Phys. J. C **79**, 759 (2019).
[81] P. Romatschke and M. Strickland, Phys. Rev. D **68**, 036004 (2003).
[82] E. Molnár, H. Niemi, and D. H. Rischke, Phys. Rev. D **94**, 125003 (2016).
[83] I. P. Mysovskikh, Dokl. Akad. Nauk SSSR **296**, 023006 (2003); Sov. Math. Dokl. **36**, 229 (1988).
[84] L. Mieussens, J. Comput. Phys. **162**, 429 (2000).
[85] L. R. Weih, A. Gabbana, D. Simeoni, L. Rezzolla, S. Succi, and R. Tripiccione, Mon. Not. R. Astron. Soc. **498**, 3374 (2020).
[86] C.-W. Shu and S. Osher, J. Comput. Phys. **77**, 439 (1988).
[87] S. Gottlieb and C.-W. Shu, Math. Comput. **67**, 73 (1998).
[88] G. S. Jiang and C. W. Shu, J. Comput. Phys. **126**, 202 (1996).

[89] S. Busuioc and V. E. Ambruş, Phys. Rev. E **99**, 033304 (2019).
[90] G. Giacalone, A. Mazeliauskas, and S. Schlichting, Phys. Rev. Lett. **123**, 262301 (2019).
[91] J. Noronha-Hostler, L. Yan, F. G. Gardim, and J.-Y. Ollitrault, Phys. Rev. C **93**, 014909 (2016).
[92] H. Niemi, K. J. Eskola, and R. Paatelainen, Phys. Rev. C **93**, 024907 (2016).
[93] J. E. Bernhard, J. S. Moreland, S. A. Bass, J. Liu, and U. Heinz, Phys. Rev. C **94**, 024907 (2016).
[94] G. S. Denicol, S. Jeon, and C. Gale, Phys. Rev. C **90**, 024912 (2014).
[95] A. Kurkela, W. van der Schee, U. A. Wiedemann, and B. Wu, Phys. Rev. Lett. **124**, 102301 (2020).
[96] A. Kurkela, A. Mazeliauskas, J.-F. Paquet, S. Schlichting, and D. Teaney, Phys. Rev. Lett. **122**, 122302 (2019).
[97] A. Kurkela, A. Mazeliauskas, J.-F. Paquet, S. Schlichting, and D. Teaney, Phys. Rev. C **99**, 034910 (2019).
[98] M. Martinez and M. Strickland, Nucl. Phys. **A848**, 183 (2010).
[99] W. Florkowski and R. Ryblewski, Phys. Rev. C **83**, 034907 (2011).
[100] W. Florkowski, R. Ryblewski, and M. Strickland, Phys. Rev. C **88**, 024903 (2013).
[101] M. Martinez, R. Ryblewski, and M. Strickland, Phys. Rev. C **85**, 064913 (2012).
[102] M. McNelis, D. Bazow, and U. Heinz, Comput. Phys. Commun. **267**, 108077 (2021).
[103] F. W. J. Olver, D. W. Lozier, R. F. Boisvert, and C. W. Clark *NIST Handbook Of Mathematical Functions* (Cambridge University Press, New York, 2010).